STUDIES OF PLASMA FLOWS IN SCRAPE-OFF LAYER PLASMA OF ADITYA TOKAMAK

By

DEEPAK SANGWAN

PHYS06200704013

INSTITUTE FOR PLASMA RESEARCH, GANDHINAGAR, INDIA

A thesis submitted to the
Board of Studies in Physical Sciences

In partial fulfillment of the requirements
For the Degree of

DOCTOR OF PHILOSOPHY

of

HOMI BHABHA NATIONAL INSTITUTE

August, 2013

Homi Bhabha National Institute

Recommendations of the Viva Voce Board

As members of the Viva Voce Board, we certify that we have read the dissertation prepared by **DEEPAK SANGWAN** entitled **"Studies of Plasma Flows in Scrape-off Layer Plasma of ADITYA Tokamak"** and recommend that it may be accepted as fulfilling the dissertation requirement for the Degree of Doctor of Philosophy.

---------- **Date :** 20/01/2014

Chairman : Prof. V. C. Saxena

---------- **Date :** 20/01/2014

Convener : Prof. R. Jha

---------- **Date :** 20/01/2014.

Member : Dr. C. V. S. Rao

---------- **Date :** 20/01/2014

Member : Dr. D. Raju

Final approval and acceptance of this dissertation is contingent upon the candidate's submission of the final copies of the dissertation to HBNI.

I hereby certify that I have read this dissertation prepared under my direction and recommend that it may be accepted as fulfilling the dissertation requirement.

---------- **Date :** 20/01/2014

Guide : Prof. Ratneshwar Jha

STATEMENT BY AUTHOR

This dissertation has been submitted in partial fulfillment of requirements for an advanced degree at Homi Bhabha National Institute (HBNI) and is deposited in the Library to be made available to borrowers under rules of the HBNI.

Brief quotations from this dissertation are allowable without special permission, provided that accurate acknowledgement of source is made. Requests for permission for extended quotation from or reproduction of this manuscript in whole or in part may be granted by the Competent Authority of HBNI when in his or her judgment the proposed use of the material is in the interests of scholarship. In all other instances, however, permission must be obtained from the author.

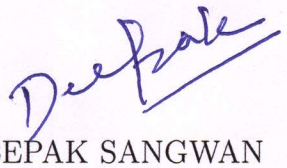

DEEPAK SANGWAN

DECLARATION

I, hereby declare that the investigation presented in the thesis has been carried out by me. The work is original and has not been submitted earlier as a whole or in part for a degree / diploma at this or any other Institution / University.

DEEPAK SANGWAN

To my family

ACKNOWLEDGEMENTS

It gives me an immense pleasure to be a part of Institute for Plasma Research, during my Ph.D. work. I would like to thank each and everyone, who have been involved directly or indirectly in the research activities carried as a part of my thesis. First of all I would like to thank my thesis supervisor, Prof. Ratneshwar Jha, with a deep sense of gratitude, for his guidance and continuous support during this thesis work. I could not have imagined the completion of such an important piece of work, without his instructions and enormous attention he has paid. I would like to thank all the Doctoral Committee members, Prof. Y. C. Saxena, Dr. C. V. S. Rao and Dr. D. Raju for following up the step by step progress made during my thesis work and for their continuous encouragement. I am pleased to acknowledge the critical support in the initial phase, from other members of ADITYA team, Dr. P. K. Chattopadhyay, Dr. J. Ghosh and R. L. Tanna. I am grateful to other faculty members, Prof. Amita Das, Prof. R. Singh, Dr. Manoj Warrier, Dr. S. Deshpande, Dr. S. Mukherjee, Dr. S. Sengupta, and others, who have taught me basic plasma physics, experimental, computational techniques or other disciplines of physics during the course work.

There were many helping hands in running the ADITYA tokamak successfully; I appreciate the support by the members of ADITYA vacuum group, ADITYA operation group, ADITYA data acquisition group and ADITYA pulse power supply group. I want to say special thanks to S.B. Bhatt, K. Jadeja, M. B. Kalal, D. S. Varia and C. Chavda. It is hard for me to forget the assistance provided, very often, by the Electronics group. Especially, I am very much thankful to Jignesh, Parmila, Parveena, Praveen and Abhijeet. I am grateful to all members of probes and bolometer diagnostics group; M. V. Goplakrishana, Kumudni Tahiliani and Samir Jha for their continuous support, and Jana Brotankova for improving my experimental skills and for her unconditional support.

I would like to thank all the staff of Workshop, Drafting, Purchase, A/C, Stores, Electrical, Computer Center, Library, and Administrative sections for their support in fabrication,procurement, maintenance and development activities during

the experimental progress related to this thesis work.

I express my sincere thanks to all of my fellow scholar's for their company and unconditional support ever.

This work would not have been possible, without the support and encouragement from my parents, brother and sister. My heartily gratitude to all of them.

Deepak Sangwan

LIST OF PUBLICATIONS

Publications in Journals:

[1] "**Plasma Flows in Scrape-off Layer of ADITYA Tokamak**", *D. Sangwan*, R. Jha, J. Brotankova and M. V. Gopalkrishna, Phys. Plasmas **19**, 092507(2012)

[2] "**Modification of Plasma Flows with Gas Puff in the Scrape-off Layer of ADITYA Tokamak** ", *D. Sangwan*, R. Jha, J. Brotankova and M. V. Gopalkrishna, Phys. Plasmas **20**, 062503(2013)

[3] "**Transport Driven Plasma Flows in the Scrape-off Layer of ADITYA Tokamak in Different Orientations of Magnetic field**", *D. Sangwan*, R. Jha, J. Brotankova and M. V. Gopalkrishna, (under review, Physics Plasmas)

Contents

SYNOPSIS

In this thesis, we have carried out experiments in ADITYA tokamak and measured plasma flows in the scrape-off layer (SOL) at different operating parameters and different spatial locations. The main motivation is to present a comprehensive studies of plasma flows, construct the possible flow pattern, and determine possible cause of the plasma flow. Plasma flows in the SOL region have been measured and studied in many tokamaks. It is now well recognized that SOL plasma flows play crucial role in the impurity control, L/H transition and global confinement of tokamak plasma. This happens because the SOL is the inter-mediating layer between main plasma and the material surface and all the plasma surface interaction takes place in this region.

The ADITYA is a medium size limiter tokamak, with major radius, R_o=0.75 m and minor radius, a=0.25 m. In ADITYA, the plasma equilibrium is not feedback controlled and hence contact of the plasma with the limiter is only in the limited poloidal region, not in the whole poloidal plane. This makes the SOL of ADITYA special. The specialty is observed in terms of simultaneous existence of long and short connection lengths in the SOL plasma. In the long connection length ($L_{\|}$) region, the outer (low) magnetic field is connected to the inner (high) magnetic field, which is not possible if the plasma touches the limiter everywhere. We have observed the effect of this special configuration in our measurements.

The thesis is divided into seven chapters, the first chapter is the introduction, the second chapter discusses different subsystems of ADITYA tokamak and the third chapter deals with the diagnostics used in our experiments. The next three chapters, namely the fourth, the fifth and the sixth ones discuss experiments carried out in ADITYA. The conclusion and future scope are presented in the last chapter. In the following, we summarize our experimental observation presented in chapters four, five and six.

The chapter four presents experimental results of plasma flow measurements in low toroidal magnetic field ($B_T \sim 0.2$ T) and at low plasma current ($I_p \sim$ 25 kA). Measurements are carried out at two locations, namely, the outboard mid-plane

($\theta = 0^o, \phi = 54^o$) and at the top port ($\theta = 90^o, \phi = 288^o$). Here limiter is the reference for toroidal angle (ϕ), which increases in the clockwise direction as seen from the top of the machine and outboard midplane is the reference for poloidal angle (θ) that increases above the midplane. The plasma flow is measured in terms of Mach number by using magnetized Mach probe, and by using the formula: $M_{\parallel} = 0.43ln(J_{UP}/J_{DN})$. The plasma density, electron temperature and floating potential are measured by using single Langmuir probes. The estimated particle diffusivity is found to be in the range of (5-10) m^2/s. The measured Mach number is found to increase with radial distance from the last closed flux surface (LCFS). Similarly, the measured Mach number decreases with increasing plasma density. Both these observations are similar to those reported from other tokamaks. The observed direction and magnitude of the plasma flow are consistent with the $E_r \times B_\theta$ drift, modified by the limiter sink action.

In the fifth chapter, we present our results of effects of a small puff of the working gas (H_2) on various plasma parameters, including plasma flows. The experiment is conducted at $B_T \sim 0.75$ T and $I_p \sim 80$ kA. The gas puff (GP) is selected in such a way that it should not affect the plasma equilibrium. The parallel flow Mach number $M_{\parallel}$, radial particle flux ($\langle \tilde{n}\tilde{v}_r \rangle$), plasma density ($n_{eb}$), Reynold stress components ($\langle \tilde{v}_r\tilde{v}_\theta \rangle, \langle \tilde{v}_r\tilde{M}_{\parallel} \rangle$) and floating potential are measured at top port ($\theta = 90^o, \phi = 288^o$) and radial outboard ($\theta = 45^o, \phi = 54^o$) above the midplane. The $M_{\parallel}$ radial profile at top port shows the shear layer near to the transition from long $L_{\parallel}$ to short $L_{\parallel}$ region. The corresponding gradient in the radial profile of $\langle \tilde{v}_r\tilde{M}_{\parallel} \rangle$ shows the coupling between mean flows and the turbulence in the shear (long $L_{\parallel}$) region and decoupling in the short $L_{\parallel}$ region. Both positive and negative values of parallel flow momentum production rate ($P_{r\phi} = -\langle \tilde{v}_r\tilde{M}_{\parallel} \rangle \frac{\partial M_{\parallel}}{\partial r}$) , shows the dual role of turbulence as a sink and source respectively for parallel flows, consistent with the previous measurements. Similarly the momentum production rate for the poloidal flows ($P_{r\theta} = -\langle \tilde{v}_r\tilde{V}_\theta \rangle \frac{\partial V_\theta}{\partial r}$) also shows the dual role of turbulence for the $E_r \times B_\theta$ flow. It is observed that the coupling between turbulence and mean flows is washed out during the gas-puff. We have also discussed the possible causes of flows, namely, $E \times B$ drift, Pfirsch-Schulter (PS) flows, poloidal pressure asymmetry caused by ballooning transport and sink action of the limiter. The increase in the $M_{\parallel}$ at both top and radial probes during GP is explained by

further rise in the pressure asymmetry and sink action of limiter. The asymmetry in $\langle \tilde{n}\tilde{v}_r \rangle$ and n_{eb} , at the top and the radial probe shows the presence of ballooning type of transport in ADITYA which is used to explain the measured flows. The observed maximum radial particle flux when the $M_{\|}$ is ~ 0, shows the importance of parallel flows in controlling the particle loss.

Mach probes at three different locations are used to determine the structure/pattern of parallel plasma flows and the effect of gas-puff on the flow pattern. It is observed that in normal ADITYA discharge (i.e., without the gas-puff), there is an indication of shell structure in the long connection length region. The shell structure is not observed during the gas-puff.

The sixth chapter deals with our experimental results on determining transport and drift driven flow components in the SOL plasma of ADITYA tokamak. The drift driven flow has contribution from $E \times B$ drift and PS flows, and the transport driven flow has contribution from ballooning transport and sink action of the limiter. They are asymmetric and symmetric respectively with respect to the change in the directions of B_T and I_p for the same helicity of the total magnetic field $B = B_T + B_\theta$. We have assumed positive/negative helicity for co/counter directions of B_T and I_p. These symmetry and asymmetry characteristics can be used to determine transport/drift driven flow components.

This experiment is carried out in four different directions of B_T and I_p, namely, (i) B_T(CW), I_p(CW), (ii) B_T(CCW), I_p(CCW), (iii) B_T(CCW), I_p(CW) and (iv) B_T(CW), I_p(CCW), where CW and CCW are clock-wise and counter-clockwise directions as seen from the top of the machine. Measurements are carried out at two locations, namely, top port ($\theta = 90^o, \phi = 288^o$) and at the outboard ($\theta = 45^o, \phi = 54^o$). The poloidal asymmetry in radial particle flux and the plasma density confirm the ballooning type of transport and its possible role in transport driven flow component. We first express, the measured Mach number as: $M_{1,2} = M_{tr} \pm M_{dr}$, where M_{tr} is the transport driven component of the Mach number and M_{dr} is the drift driven component. It is observed that although there is significant drift driven component in the measured Mach number, the transport driven component is also appreciable.

In conclusion, the present thesis describes experiments carried out to understand the plasma flows in the SOL region of the ADITYA tokamak. Firstly, we have determined that the measured Mach number contains both drift driven and transport driven components. Secondly, there is a signature of possible existence of shell structure of flows. This could be because of existence of both long and short $L_{\parallel}$ in the SOL region of ADITYA. This unique configuration also causes shear in flow Mach number in the SOL region. The additional puff of working gas can be used to eliminate the shear and reduce the edge temperature. Thirdly, we measure the Mach number by reversing the B_T and I_p, and separate out drift and transport driven components of the Mach number. It is observed that the transport driven component is significant in the measured Mach number. The future plan includes measurement of parallel plasma flows along with the poloidal plasma flows in the high field side and low field side simultaneously by using Gundestrup probe.

List of Figures

List of Tables

Chapter 1

Introduction

1.1 Fusion

The day-to-day rising demand of energy in the world forces us to think about some alternative source of energy other than conventional and nuclear fission energy source. Controlled nuclear fusion is a clean and limitless alternative energy source which can generate enormous energy without any radioactive product. In fusion reaction, two small atom (e.g, H, D, T, He) nuclei fuse and release one somewhat bigger nuclei and neutrons as the reaction product. For example the fusion between deuterium ($_1D^2$) and tritium ($_1T^3$) nuclei gives Helium ($_2He^4$) nuclei (α particle) and a neutron ($_on^1$) as reaction products. A schematic of this reaction is shown in Fig. 1.1.

$$_1D^2 \ + \ _1T^3 \ \rightarrow \ _2He^4 \ + \ _0n^1 \tag{1.1}$$

The energy is released in the form of kinetic energy of alpha particle and neutron. The energy shared by the $_2He^4$ is 3.5 Mev and by $_on^1$ is 14.1 Mev. This energy is released from the mass difference between the reactants and products (Δm) as follows:

$$D(2-0.000994)m_p+T(3-0.006284)m_p \rightarrow He(4-0.027404)m_p+n(1+0.001378)m_p, \tag{1.2}$$

where, the m_p is the mass of proton. The mass difference (Δm) between product and reactant is $0.01875 m_p$. The energy released is $E = \Delta m c^2 = 2.818 \times 10^{-12} joule = 17.59\ MeV$, where, c is the speed of light. Other possible fusion reactions in ${}_1D^2$-${}_1D^2$ plasma are:

$$ {}_1D^2 + {}_1D^2 \rightarrow {}_1T^3(1.01MeV) + {}_1p^1(3.03MeV) \tag{1.3} $$

$$ {}_1D^2 + {}_1D^2 \rightarrow {}_2He^3(0.82MeV) + {}_0n^1(2.45MeV) \tag{1.4} $$

$$ {}_1D^2 + {}_2He^3 \rightarrow {}_2He^4(3.67MeV) + {}_1p^1(14.67MeV) \tag{1.5} $$

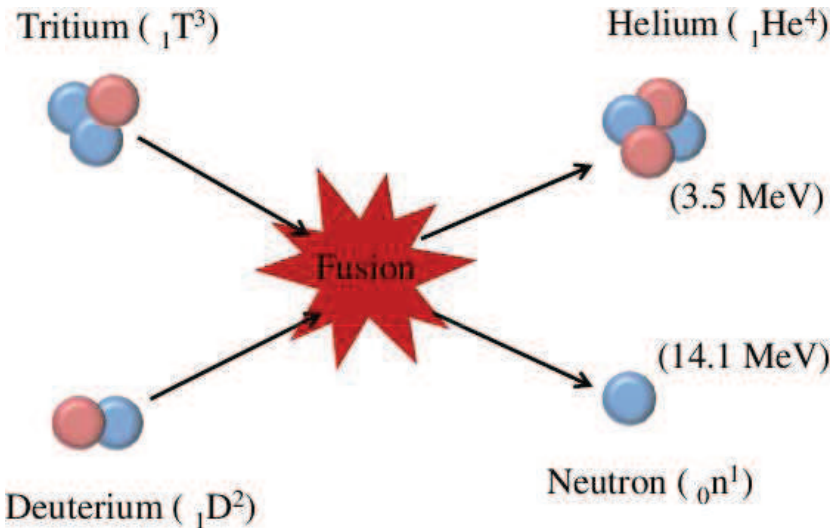

Figure 1.1: *Fusion reaction cartoon. It shows the fusion of tritium nucleus and deuterium nucleus. The reaction product are helium nucleus with 3.5 MeV energy and a neutron with 14.1 MeV energy.*

For fusion reaction to take place the two reactant nuclei should come close enough, so that they come under the influence of nuclear forces, which are short range forces. Here the fusion nuclei are of the same charge (positive), so they would not like to share the locations very near to each other. Our job is to bring these two same charged nuclei together and force them to cross their coulomb barrier [1]. We can do this by keeping these small nuclei at large temperature. This temperature can

[1]It is the repulsion barrier of the two same charge nuclei. Once the nuclei cross this, the nuclear force will start dominating and fuse two nuclei.

bring two atoms together by their random motion (high kinetic energy) and make it possible to cross the Coulomb barrier. The fusion reaction rate is maximum at certain ion temperature (T_i), shown in Fig. 1.2[1] for three different fusion reactions.

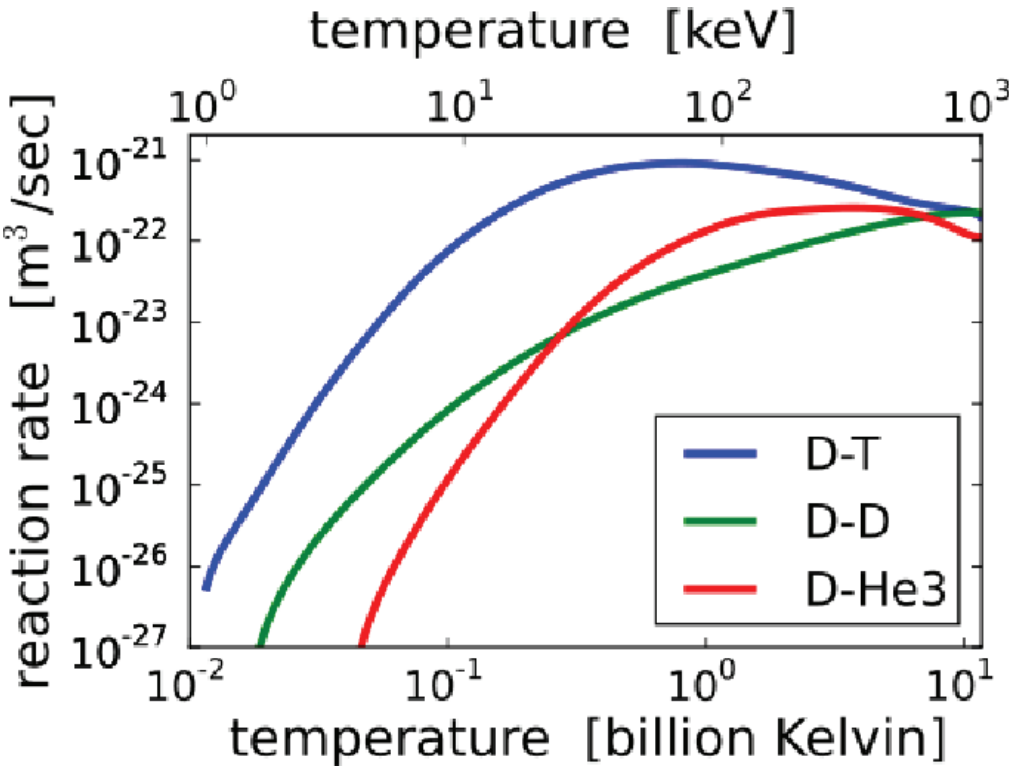

Figure 1.2: *Fusion reaction rates for the various fusion reactions. The rate of fusion reaction is maximum around a particular ion temperature, e.g. the reaction rate for the deuterium-tritium fusion reaction is maximum around 100 keV.*

The criterion for fusion reaction breakeven in terms of density (n_i), ion temperature and energy confinement time (τ_E) is defined by Lawson [1]. According to this criterion the product $n_i T_i \tau_E$ should be at least $\sim 5 \times 10^{21}\ m^{-3} keV s$. The rate of collisions between the fusion nuclei depends on the number density, so the number density is a part of the Lawson's criterion. The high speed of the nuclei are helpful in overcoming coulomb barrier. The thermal speed is equivalent to the temperature of the particles. Since at high temperatures the probability of the colliding nuclei to overcome their column barrier is high, it appears in the Lawson's criterion. At very high temperature the relative time that the two nuclei spend

[1]Figure taken from Wikipedia.

together decreases, which put an upper limit on the temperature. In addition, the brehmstrahlung radiations rate increases at high temperature ($\propto \ T^{1/2}$) [2] and at high density ($\propto \ n_i^2$), it puts an upper limit to both temperature and density. Along with these two, the third requirement, the energy confinement time is to maintain the reaction for sufficient time.

The problem with these highly energetic charge particles is that they simply cannot be put in a container. As they have high energy they can move to the vessel walls and lose their energy, and recombine at the wall. So, we need something to keep these energetic particles together and away from any material surface for long time which should be sufficient to satisfy Lawson criterion. One way is by the magnetic confinement. A cylindrical device with axial magnetic field can be used to prevent the loss of plasma particle radially, but the drawback is that the charge particles are still free along the axial direction. The particles lose at very fast rate through ends, as the charge can move freely along the magnetic field.

On the other hand in the radial direction, perpendicular to the magnetic field, the motion of the charge particles is restricted by the magnetic force ($F_\perp = q\mathbf{v} \times \mathbf{B}$), where $\mathbf{B}$ is the magnetic field, $\mathbf{v}$ is the particle velocity and q is the charge. To prevent the axial loss, magnetic mirrors came into picture in which the magnetic field strength changes in the axial direction [see Fig. 1.3].

This configuration is successful up to some temperature to confine the plasma particles but unable to hold the particles for long time because of the loss of high temperature through the end faces of magnetic mirror. To overcome this shortcoming, a new way to confine the charge particles was put forward by the Russian physicists Igor Tamm and Andrei Sakharov in 1950 in the form of tokamak. The tokamak is a Russian word, which means toroidal chamber with axial magnetic field. The problem of loss of high energy particles in the magnetic mirror is solved in tokamak by joining the two open ends of the axial magnetic field. This solves the problem of axial loss of high energy particles in tokamak. Tokamak is a toroidal device, which uses the axial or toroidal magnetic field as a main magnetic field. However, a purely toroidal magnetic field causes vertical charging of the plasma and hence it is unstable. In order to overcome this deficiency a toroidal plasma

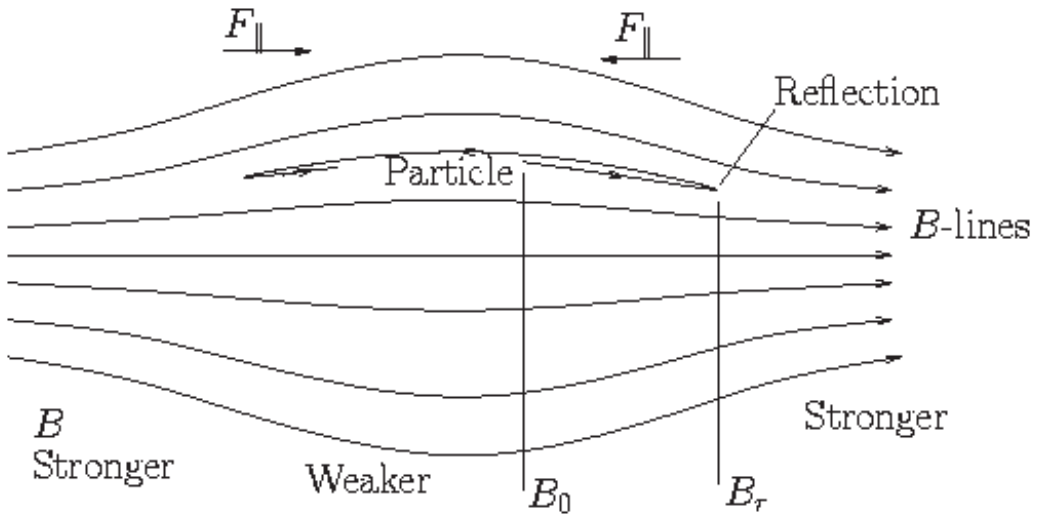

Figure 1.3: *Magnetic mirror field configuration. Here $F_\parallel$ is the axial force on the particle due to gradient in the magnetic field from B_o at the center to B_τ at the reflection point. The reflection of particles from the two ends gives it mirror name. The axial field strength is maximum at two ends and minimum at the center. It changes the particles parallel velocity, which is maximum at the middle of the mirror, and zero at the reflection points. On the other hand the reflection of high energy particles is not possible, as the field is not able to make their parallel velocity zero at the ends.*

current is used, which generates a poloidal field, so that the net magnetic field is helical and hence the vertical charging of the plasma is avoided. A tokamak model is shown in Fig. 1.4[1].

Tokamaks open a new era in fusion research. Russians are the first to enter in tokamak research area. Presently working tokamaks are DIII-D [3], JT-60 [4], JET [5], Tore Supra [6], EAST [7], MAST [8], HT-7 [9], TEXTOR [10], ASDEX Upgrade [11], Alcator-C Mod [12], TCV [13], COMPASS [14] and ADITYA [15]. Tokamak research has made a tremendous progress in last 50 years. By realizing that no single country is able to achieve the fusion on its own, different countries have come forward for a joint collaborative work in the field of fusion in the form of ITER, in France [16].

[1]Figure taken from Internet

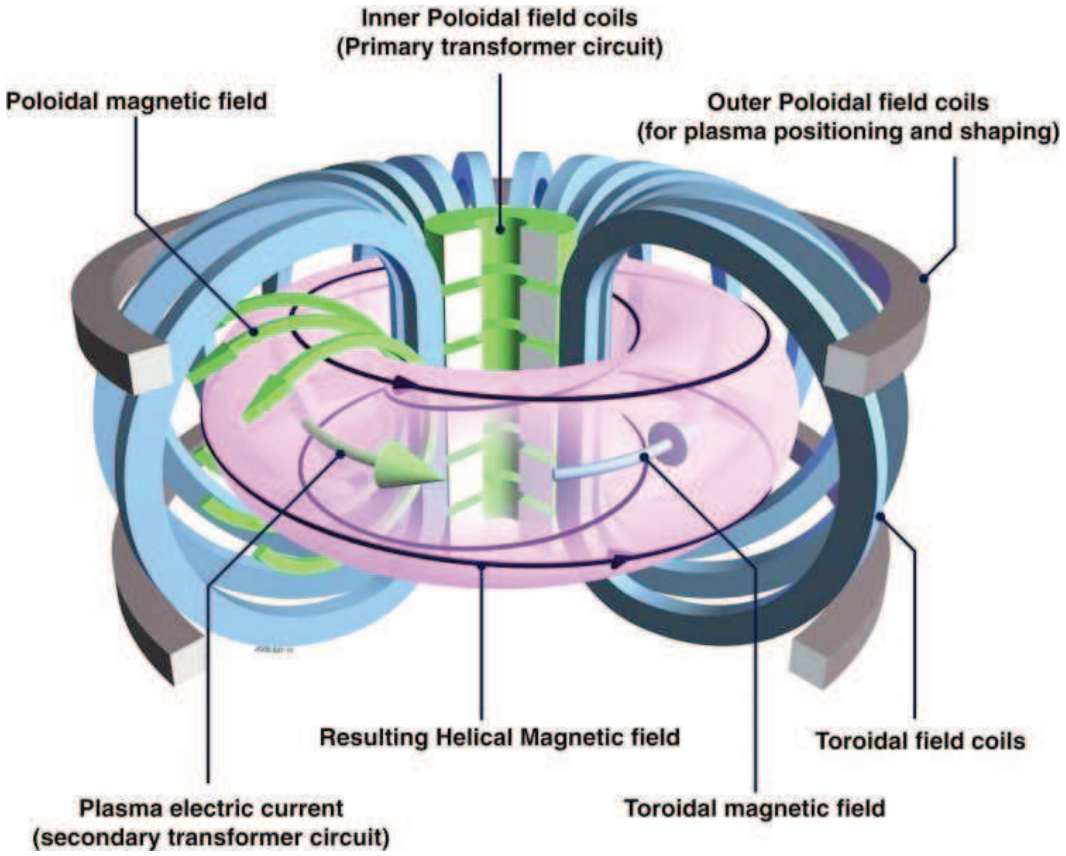

Figure 1.4: *Schematic of tokamak with different field coils. The toroidal field coils are used to generate the toroidal magnetic field and the primary transformer drives the toroidal plasma current in the gas. Here the plasma is the secondary of the transformer. The resulting helical field lines are superposition of the toroidal magnetic field and the poloidal magnetic field. The poloidal magnetic field is generated by the plasma current.*

Based on construction, tokamaks can be divided into two categories: limiter tokamak and divertor tokamak. The limiter/divertor is used to define the plasma boundary and control the plasma surface interaction. Both limiter and divertor are of three types. Limiters are: (i) toroidal rail limiter, (ii) poloidal ring limiter, and (iii) point limiter. The corresponding divertors are (i) toroidal divertor, (ii) poloidal divertor, and (iii) bundle divertor [17]. Poloidal limiter and poloidal divertor are the most used configurations in the limiter and divertor tokamaks. Today, all the big tokamaks have poloidal divertor configurations because of its

better control over the plasma surface interaction.

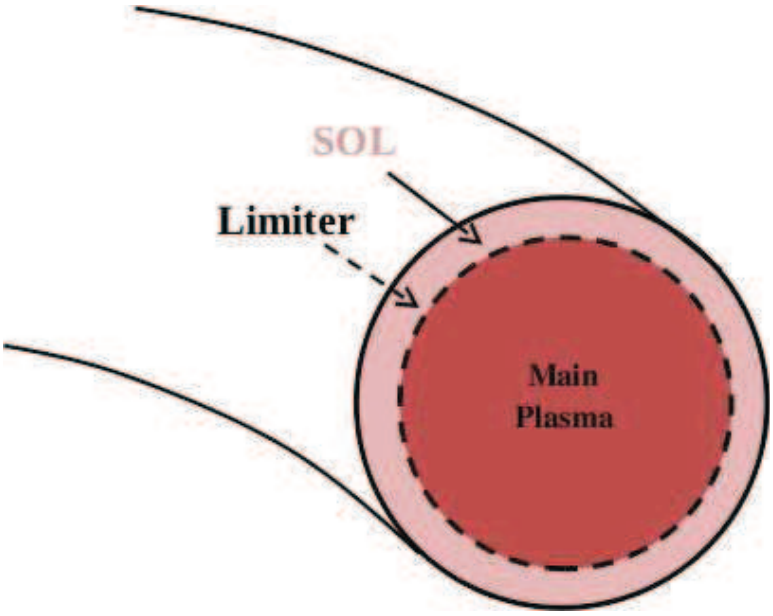

Figure 1.5: *Schematic diagram of the scrape-off layer in the limiter plasma. The dashed circle is the limiter edge. Plasma inside the limiter is the main plasma with closed field lines and the plasma in limiter shadow is the scrape off layer plasma with open field lines. Here the field lines open at the limiter.*

Tokamak plasma is divided into two regions, namely, main plasma and scrape-off layer(SOL) plasma [see Fig. 1.5 for limiter SOL and Fig. 1.6 for the divertor SOL]. The main plasma is the relatively hot plasma which is confined in the closed field lines and the SOL plasma is the plasma in the open field lines which is relatively cold. Here the open field lines are the field lines which touch some material surface. The SOL plasma works as an interface between the main confined plasma and the material surface. It has the major role in deciding the main plasma purity and different confinement times, namely the energy and the particle confinement time[1].

[1]Particle confinement time is the average time spend by the particles in the main plasma and the energy confinement time is the average time spend by the energy in the main plasma.

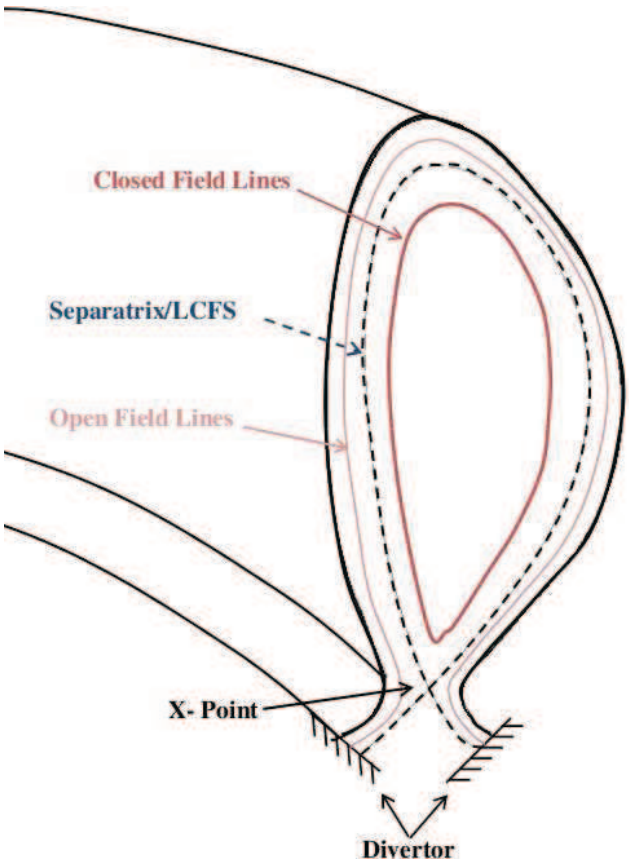

Figure 1.6: *A single null (X-point) divertor tokamak scrape-off layer and main plasma. The field lines inside the separatrix/LCFS are the closed field lines and outside the separatrix field lines are opens up at the divertor. The benefit of divertor tokamak over the limiter tokamak is that in the divertor tokamak, the main plasma is not in the direct contact with the material surface. In single null the outboard field lines connects to the inboard field lines from the other side of null point but in the double null (i.e., with two X-points) the outboard field lines do not connect to the inboard field lines as the both top and bottom paths are blocked by the null point.*

1.2 Scrape-Off Layer (SOL)

Scrape-off layer (SOL) is the outer layer of tokamak plasma [See Fig. 1.5 and Fig. 1.6]. As mentioned before, the SOL keeps the hot plasma away from the material surface, so that the interaction of the main plasma and the material surface is minimum. In the limiter tokamak the last closed flux surface (LCFS) location

is decided by the material surface (limiter) and in the divertor tokamak the LCFS is decided by the magnetic field. The LCFS is the magnetic flux surface after which the field lines touch the limiter/divertor and the magnetic field lines on the inner side of this flux surface are closed. Due to this proximity of the main plasma with the material surface in limiter SOL, the plasma surface interaction is large as compared to the divertor SOL. This interaction is mainly the sputtering of the material surface by the plasma ions. In an ideal condition, we want to isolate the main plasma from any kind of material surface, so that there is no impurity ion in the plasma to dilute it. These impurity ions take useful energy of the plasma and radiate it. The radiation cools the plasma and makes the temperature rise of the plasma difficult. In reality, we cannot completely isolate the plasma from the material surface effects. The SOL provides an isolation cover to the main plasma. In limiter SOL, it is believed that all the plasma solid interaction takes place at the limiter which is in the direct contact of the plasma. A number of attempts has been carried out to minimize the material damage due to sputtering [18]. In case of divertor SOL, the divertor is very far away from the hot plasma which results in low temperature plasma contact with the divertor and less impurity. The impurity which is generated at the solid surface has to travel through the SOL region to reach main plasma. Once it reaches the main plasma, it partially ionizes there and starts radiating.

An important source of the plasma in the SOL is the plasma diffusion from the main plasma. A slab model of SOL is presented in the Fig. 1.7 [17]. As shown in the Fig. 1.7, the diffusion of the plasma across the toroidal magnetic field populates the SOL. The SOL width is determined by the diffusion coefficient and the limiter type and the ion sound speed [18]. The simple SOL width can be written as $\lambda_{SOL} = \left(\frac{D_\perp L_\parallel}{C_s}\right)^{1/2}$, where $D_\perp$ is the diffusion coefficient, $L_\parallel$ connection length and C_s is the ion acoustic speed[1].

The SOL plasma controls the impurity level along with the energy confinement time (τ_e) and particle confinement time (τ_p) [17]. Thus the understanding of the SOL plasma is essential. The complete control over the impurity generation in the

[1]The number of limiters decides the parallel connection length $L_\parallel$ of the field lines and hence the SOL length.

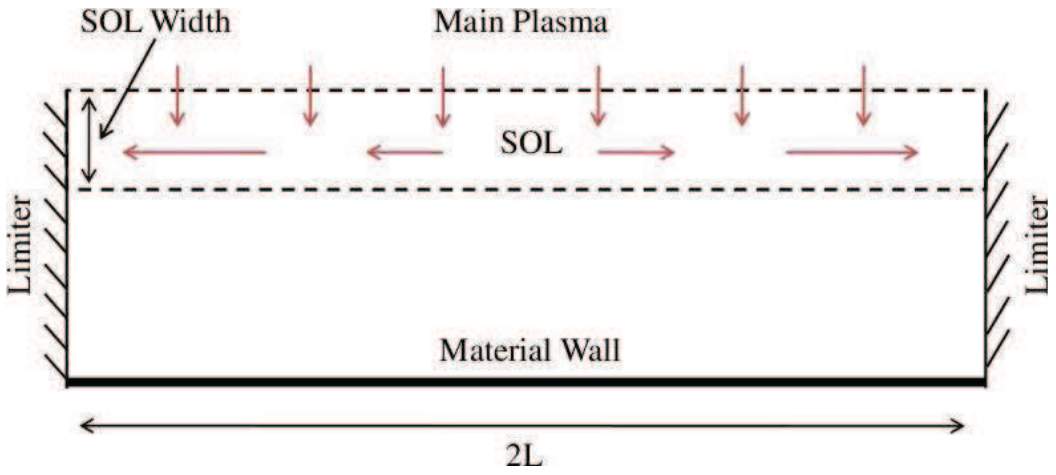

Figure 1.7: *Schematic of the plasma diffusion from the main plasma to SOL. The diffusion of the plasma from the main plasma is shown by the vertical arrows. The SOL width, shown by the double arrow, is controlled by the parallel connection length $L_{\parallel}$, diffusion coefficient $D_{\perp}$ and ion sound speed C_s. The $L_{\parallel} = \pi R$, for the single poloidal limiter SOL, where R is the major radius. Two hatched lines are the two faces of the limiter and the material walls is shown by the thick line.*

SOL is not possible but the impurity generated in the SOL can be moved by the plasma flows in the SOL [19]. This makes SOL region more important from the point of view of strong plasma flows, which may also influence the confinement of the main plasma. These flows may have components in the toroidal and the azimuthal (poloidal) directions. The SOL plasma flows are described in the next section.

1.3 SOL Plasma Flows

The continuous movement of the plasma is termed as the plasma flow. The flow in the plasma may be due to some drift or by forces due to the pressure gradient and the electric field. Plasma flows are present throughout the plasma device including tokamak SOL. The toroidal geometry of the tokamak makes SOL plasma flows interesting. In the simple SOL model[1] it is expected that plasma flow should be present near to the material boundary surface, and there is a stagnation point in-between the two faces of limiter/divertor. Here the sink ac-

[1]In the simple SOL the diffusion from the main plasma is the only source of the plasma

tion of the limiter/divertor is the only source of the plasma flow, as indicated in Fig. 1.8. It is expected that the particles leave the main plasma by cross field diffusion and enter into the SOL and taken away by the plasma flows to the nearest face of the limiter/divertor by the sink action. But in the SOL, plasma flows are observed at all locations and even away from the limiter/divertor. [3, 4, 5, 12, 19, 20, 21, 22, 23, 24, 25].

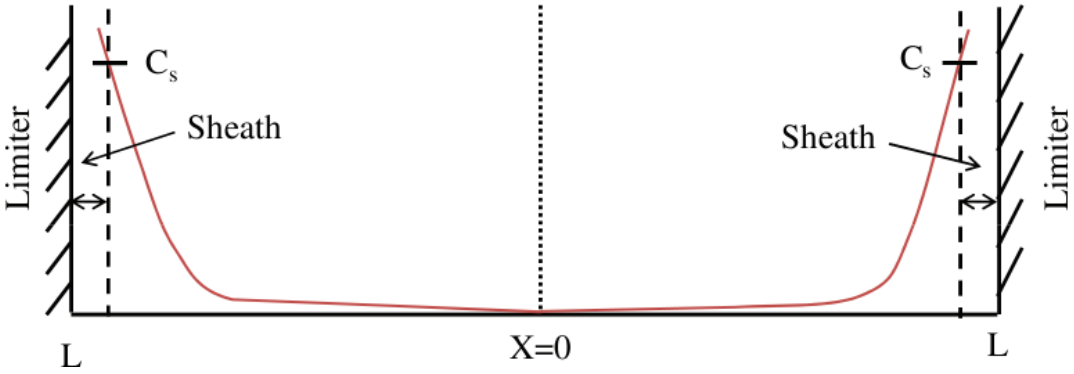

Figure 1.8: *Schematic of simple scrape-off layer plasma flows. Here the only deriving term behind the plasma flows is the limiter sink action. The speed of ions reaches to C_s at the sheath edge, which is $\sim 10\lambda_D$ thick (exaggerated). The midplane between the two faces remain stagnated and plasma accelerates on both sides of this midplane.*

The SOL flows play significant role in the transition between low (L) and high (H) confinement modes. The SOL flow can affect the direction of rotation of the main plasma [12]. It is observed that the SOL flow in the co-current direction helps in achieving the L/H transition at lower power. The L/H transition in tokamaks is accompanied by the sudden increase in the mean poloidal velocity [26]. The increase in the poloidal flow velocity sets a transport barrier, which in turn increases the confinement. This transition is triggered by the onset of fluctuation suppression by the sheared SOL flows. The SOL flow also helps in impurity removal and thus screens the main plasma from impurities [19, 27]. This impurity removal is done through the increase in the frictional force between plasma and impurity ions.
Plasma flows are very complex and this complexity can be seen in the form of differences in simulated/analytical/measured SOL flows [28]. The SOL plasma flow in the neoclassical picture is due to forces on the ions caused by pressure difference along the field lines and various components of electric field. All these

effects are unique to the tokamak. The advantage of tokamak shape in the plasma confinement comes with some toroidal effects, which makes plasma confinement somewhat difficult. These effects include the curvature drift, gradient drift and the outboard shift of the plasma due to bad curvature of magnetic field. Thus the pressure along the field lines is different on the outboard and inboard side. This difference generates the plasma flow from the high pressure to low pressure region. On the other hand, the presence of the material body in the plasma generates a presheath which gives rise to a flow. Some flows are self organized, they come into picture because of presence of some other drifts. The Pfirsch-Schluter (PS) flows comes into this category; it helps to sort out the charge separation at the top and bottom of the plasma column. Its direction on the outboard side is in co-current direction and at the inboard side it is in counter-current direction [4].

Major causes of plasma flows are similar in all tokamaks, but their magnitude and radial profiles depends on the plasma properties there, geometry, and location of limiter/divertor. In poloidal limiter, if plasma touches the limiter in full poloidal plane, the outboard SOL field lines are not connected to the inboard field lines, as they open up at the limiter before tracing one full toroidal rotation. In such a situation the particle pressure rises on the outboard side due to transport asymmetry (ballooning transport). On the other hand, in case of limited area contact in poloidal limiter plasma, the outboard field lines are connected to the inboard side field lines. Thus the outboard-inboard flow due to pressure asymmetry is possible. Parallel flow components which are driven by PS ion current and $E \times B$ flow reverses with the reversal of B_T and I_p, on the other hand the sink action of limiter/divertor and the ballooning transport driven flows are independent B_T and I_p directions. On the basis of this, the flows are divided in two components, drift driven and transport driven which are B_T and I_p direction dependent and independent, respectively.

1.4 Brief review of earlier works

The SOL plasma flow has been studied in most of the tokamaks, including, DIII-D, JT-60, JET, Tore Supra, ASDEX Upgrade, Alcator-C Mod, TCV, TdeV and DITE

[3, 4, 5, 6, 11, 12, 13, 22, 29]. The Mach probe(s) and Hutchinson's model are used to calculate the flow Mach number, $M = Kln(J_{UP}/J_{DN})$ where K=0.35-0.45, and J_{UP} and J_{DN} and the ion saturation current density at the two sides of the Mach probe [30]. In divertor tokamaks, the flow pattern is more or less same in spite of differences in the divertor geometries. The limiter tokamaks, Tore Supra [6, 31], Alcator [32], DITE [29, 33] and T-10 [34] show all the flow properties which are observed in the divertor tokamaks. The main purpose of study is to know the causes and the flow drive mechanisms behind the observed flows and to know their effects on the main plasma properties. The known causes behind the plasma flows are PS flows, $E \times B$ drift, ionization imbalances, poloidal asymmetry by the ballooning transport and limiter/divertor sink action [35].

The SOL flow measurements are carried out at different poloidal locations in tokamaks. In Alacator C-Mod, the measurements have been carried out at the low field side (LFS), high field side (HFS) midplane, and at LFS near to the divertor [12, 25]. Mach probe measurements are also carried out at the outer midplane to remove the effect of ionization and poloidally asymmetric transport generated flows [36]. Alcator C-Mod is the first tokamak in which flow measurements in the HFS midplane are carried out. In the same tokamak, the parallel flow Mach number that peaks ∼2 mm from the LCFS and the poloidal flow of ∼ 0.2 to ∼1 times of electron diamagnetic velocity are observed [12, 37].

It is observed that both $E \times B$ drift and pressure asymmetry play major roles in Alcator C-Mod SOL flow. On the other hand, the plasma flow measurements in JT-60U, at the LFS midplane, near the HFS divertor plate and near the X-point in the LFS are carried out, and shown that the flow reversal (flow away from divertor plate) occurs at the main plasma edge [4, 19, 38].

It is found that PS flow is the driving mechanism in this case. The analytical model gives similar results [4]. On the other hand, the measured flows in JET are large as compared to the model prediction [5, 28]. Flows in the JET [5, 28] and Tore Supra [6] are measured at the top of the plasma column, and in DIII-D at the X-point location [3]. In JET, the flow Mach number of ∼0.5 is observed and it is from outboard to inboard SOL, which changes sign when the field direction is re-

versed. It is shown that the Mach number is maximum at ~ 25 mm away from the LCFS and measurements are consistent with the PS flows. In TCV, measurements are carried out at the LFS below the midplane [13] and in the ASDEX-Upgrade at the LFS midplane, and at the inboard divertor location [11]. The PS flows are observed to be consistent with the magnitude and direction of the measured flows in TCV. In DITE, both $E \times B$ and PS flows are major factors behind the flows [39].

The pressure asymmetry in the LFS and HFS due to ballooning type of transport plays a significant role in generating SOL plasma flows. In JT-60U, the quantitative evaluation of the plasma flows shows that they are generated to maintain the same pressure along the field lines [38]. The measured SOL flows in JT-60 [38], ASDEX [11], ALCATOR C-Mod [12] and JET [28] are found to be from the LFS to HFS in single null divertor configuration. It may be due to the pressure difference between the LFS and HFS. In Alcator C-Mod, experiments in all possible magnetic topologies, which includes: lower single null (LSN), upper single null (USN) and double null (DN) have been carried out. It is found that the pressure e-folding length is nearly 4 times less on the HFS SOL as compared to the LFS SOL. Whereas, supersonic Mach number at the HFS is observed in both single null configurations and, in the DN configuration the HFS Mach number is zero. On the other hand, the Mach number on the LFS is ~ 0.3 in case of LSN, and nearly zero in the USN. In the HFS, flow is in the co-current direction for LSN and in the counter-current direction in the USN. The pressure asymmetry effect is also observed in Tore Supra. In Tore supra, the location of limiter plasma contact point is varied and the Mach number from subsonic to supersonic range are observed. In JET, measurements are carried out by changing the direction of B_T and Mach number is found to differ by ~ 0.2 [5, 28]. The increase in the ballooning transport induced Mach number with plasma density is observed.

The effect of the density ($\bar{n}_e$) on the SOL flow have been observed in ASDEX [11], JET [28], ALCATOR C-Mod [12], TCV [13] and JT-60U [4, 38]. The effect of the increase in the $\bar{n}_e$ is also studied on the radial profile of Mach number. In JT-60U, a density scan in the range $\bar{n}_e \sim (1-3) \times 10^{19}\ m^{-3}$ has been carried out and a decrease in the flow Mach number are observed at large density for both directions of B_T. On the other hand in JET, both decrease and increase in the

Mach number have been reported at large density for the two directions of the B_T. In ASDEX, high density experiments show the flow reversal at the far region from the LCFS whereas near the LCFS region the flow remains in co-current direction. It is explained by the possible effect of the divertor detachment at large density. Mach number measurement at the TCV shows decrease in the Mach number from $\pm$ 0.6 to ~ 0 in the density range of $(1-8)\times 10^{19}\ m^{-3}$ for the two directions of B_T. In Alcator C-Mod, decrease in the Mach number at one location and insensitivity of $\bar{n}_e$ increase at two other locations have been reported.

The SOL flow can effect the L/H transition and the main plasma rotation [40]. The SOL flow effect on L/H transition have been studied extensively in Alcator C-Mod [12]. In Alcator C-Mod, the importance of the SOL flows on the L/H transition has been studied. It is found that the change of the core plasma rotation is directly related to the SOL flow at the separatrix. It has been reported that the L/H transition requires less power when the SOL flows are is in the co-current direction. The SOL flow does not play any role in the core rotation once the H mode is achieved. In Mast, modification of SOL flow during the L/H transition is observed [8]. The effect of the SOL comes in terms of the decrease of particle flux by the $E \times B$ flow shear, which in turn helps in L/H transition [22].

Turbulence is one more possible source for the SOL plasma flow. The study of interplay between turbulence and mean flows are carried out by measuring the Reynolds stress. Reynolds stress is the medium of coupling between flows and turbulent transport. The link between the turbulence and the mean flows have been studied in many tokamaks. JET experiments [41] shows a dynamic coupling between parallel flows and radial turbulent transport, experiments shows that turbulence can drive parallel flows in the SOL region of the tokamak. Another experiment in JET tokamak [42] have shown the dual role of turbulence as a damping and deriving source for the SOL flow. In the TJ-II stellarator, the plasma profile and turbulence was investigated [43], and found that above a certain density threshold, the production term $P = -\langle \tilde{v}_r \tilde{M}_\parallel \rangle \frac{\partial M_\parallel}{\partial r}$ can act as an energy sink ($P > 0$) for the mean flow or energy source ($P < 0$). Where $M_\parallel$ and v_r are the parallel Mach number and the radial velocity respectively. In the HT-6M tokamak, the first experimental evidence of the correlation between the Reynolds

stress gradient and the poloidal flow acceleration in the tokamak edge have been reported [44]. It has been observed that the turbulence induced Reynolds stress might be the dominant mechanism to create the poloidal flow and $E_r \times B$ flow shear.

Scrape-off layer flows can be modified by a small puff of working gas during the discharge. Experiment have been carried out in JT-60U [19] to establish the effect of the gas puff on the SOL plasma flows. It has been observed that the parallel SOL flow towards the divertor increases with the gas puff by $\sim (20-25)\%$. In DIII-D [27] and JT-60U, the effect of gas puff on the impurity screening have been studied. In JT-60U, reduction in Z_{eff} from range (1.47-1.53) to (1.29-1.33). In DIII-D, decrease in the Z_{eff} is explained by the establishment of the SOL plasma flow by the divertor pumping or increase in the SOL shielding. In JT-60U, the improvement in the impurity shielding with the gas puff is explained by the increase in the SOL flow and electron density at the HFS. It may be because of increase in the frictional force of bulk ions on the impurity ions. In Alcator C-Mod [12] the effect of the SOL flows on the impurity removal is studied by the impurity puff injection. It has been found that the impurities born at the inside midplane wall migrate towards the inner divertor, regardless of the single-null X-point location. In ADITYA, the increase in the Mach number at the top of the machine and above the LFS midplane during the gas puff is found [15]. The flow reversal is observed at the LFS midplane.

The SOL plasma flows can be divided in two categories, namely drift-driven flow and transport-driven flow. Transport driven flows are B_T and I_p direction independent, on the other hand the drift driven flows are B_T and I_p direction dependent. Transport driven flows include the flow generated by the LFS and HFS pressure asymmetry, sink action of limiter/divertor and the drift driven flows include $E_r \times B$, diamagnetic drift and PS flows. Using this symmetry and asymmetry, transport and drift driven flows are estimated from the measured Mach number. In Alcator C-Mod [12, 25, 37], experiments have been carried out by reversing the B_T and I_P. The estimation indicates the strong presence of ballooning transport in the Alcator C-Mod. In TCV, the experiment carried out by reversing the B_T and I_p and the reversal of the flow direction have been observed, which, indicates the dominance of the drift driven flows [13]. In JET [28], the estimated transport driven Mach

number is ~ 0.2.

1.5 Thesis Outline

The study of SOL plasma flow along with other plasma parameters is carried out in the ADITYA tokamak at different toroidal and poloidal locations. The motive behind these studies is to construct the SOL plasma flow pattern and to find out factors which can effect flows and to determine possible causes behind these flows. The review of earlier work show that the SOL flows are very complex in nature, so to understand these flows in better way their measurements in all the tokamaks are necessary, including ADITYA. This thesis on ADITYA SOL flow measurements help to make a global picture of the SOL flows with different tokamaks. The thesis is divided into seven chapters including introduction which is the first chapter.

Chapter II describes about the basic concept of the ADITYA tokamak design. The basic operational diagnostics including loop voltage, plasma current, plasma position measurement, μm interferometer (cord average density), soft X-ray (core T_e), hard X-rays are discussed. The schemes used for the vessel cleaning are also discussed.

Chapter III discusses about the theory and design of probes used to study the SOL plasma flows and other SOL properties. They include Langmuir probe, Triple probe, and Mach probe.

Chapter IV describes the results of plasma flows measurements at low $B_T = 0.2$ T and low $I_p = 25$ kA [15].

Chapter V addresses the effect of a small gas puff of the working gas on the SOL plasma flow along with other SOL plasma properties. A controlled puff of working gas is allowed during the flat top period of plasma current. The parallel flow Mach number $M_{\|}$, radial particle flux ($\langle \tilde{n}\tilde{v}_r \rangle$), plasma density, Reynold stress components ($\langle \tilde{v}_r\tilde{v}_\theta \rangle, \langle \tilde{v}_r\tilde{M}_{\|} \rangle$), and floating potential are measured at two toroidal/poloidal locations. Measurements shows the poloidal asymmetry in the SOL parameters [45].

The measured $M_{\parallel}$, $V_\theta = E_r \times B_T$ and corresponding Reynolds stress radial profile shows the coupling between mean SOL flow and turbulence [42, 43, 46]. Significant effect of gas puff are observed on the $M_{\parallel}$, V_θ, T_e and the turbulence mean flow coupling. These measurements are carried out in high $B_T = 0.75$ T and high $I_p = 80$ kA.

Chapter VI describes the estimation of both drift driven and transport driven flow components from the measured Mach number in high B_T and I_p [15, 45]. The drift driven flow component are asymmetric and the transport driven flow component is symmetric with respect to the change in the B_T and I_p directions [12, 25]. We have carried out experiments with the aim to separate out the drift and transport driven flow in four different combinations of B_T and I_p. Measurements are carried out at two different toroidal/poloidal locations [47].

The conclusions and future scope are presented in chapter VII.

Chapter 2

Different Subsystems of ADITYA Tokamak

2.1 Introduction

The ADITYA tokamak is a medium size tokamak [48] at the Institute for Plasma Research, India. ADITYA commissioned in 1990's with scientific objectives of (a) study of density and current limits, (b) study of novel regimes of operation and (c) investigation and control of edge phenomenon. The other motive behind the ADITYA is to train the manpower in various diagnostics and other operation related issues of the fusion grade machine. It will be helpful for the future large tokamak machine operation. The machine parameters were chosen in accordance with the available indigenous technology and to provide sufficient access for the different diagnostics [see Table (2.1) for ADITYA design parameters]. In this chapter, we have discussed the ADITYA tokamak design and the various basic operational diagnostics.

The rest of the chapter is organized as follows: Sec. II describes the vacuum vessel of ADITYA, Sec. III describes the limiter , Sec. IV describes the electro-magnets of ADITYA and plasma equilibrium, Sec. V deals with the preionization filament, Sec VI discusses about the vessel cleaning techniques, Sec. VII describes the basic diagnostics, and Sec.VIII describes the various operational limits of ADITYA.

Table 2.1: ADITYA Design Parameters

1.	Plasma major radius	R	0.75 m
2.	Plasma minor radius	a	0.25 m
3.	Toroidal magnetic field	B_T	1.5 T
4.	Safety factor	q(a)	2.5
5.	Plasma current	I_p	250 kA
6.	Electron temperature	T_e	500 eV
7.	Ion temperature	T_i	200 eV
8.	Energy confinement time	τ_E	5 ms
9.	Plasma duration	τ	300 ms

2.2 Vacuum Vessel

The vacuum vessel of the ADITYA tokamak is made up of non-magnetic SS 304L material in four quadrants. Toroidal electrical discontinuity is provided at two locations for fast penetration of the loop voltage [see Fig. 2.1]. The vacuum vessel is designed in such a way that it can easily withstand the static and dynamic forces. The estimated maximum dynamic force under the worst conditions is $\sim 5 \times 10^4$ Newtons and displacement is ~ 0.4 mm. To avoid the displacement during the dynamic force a suitable clamping is provided. The base pressure of the vacuum vessel is $\sim 1 \times 10^{-7}$ $Torr$, which is maintained by two turbo molecular pumps of 2000 l/s speed each and two cryopumps with 10000 l/s speed each. The turbo molecular pumps are backed by the rotary pumps of 60 cubic meters per hour pumping speed. The pumping system is chosen in such a way that it can withstand the high gas load during the plasma discharges and glow discharge cleaning. The good clean vacuum is kept by using glow discharge cleaning and pulse discharge cleaning of vessel every day. The vacuum vessel is of major radius 75 cm with the square cross section of 60 cm. The wall thickness of top and bottom part is 20 mm, and for inner and outer part of the vacuum vessel it is 10 mm.

2.3 Limiter

The side by side existence of solid and plasma is not possible without any interaction. This interaction is mainly controlled by the toroidal magnetic field in the tokamak by restricting the radial motion of plasma particles. But still a significant

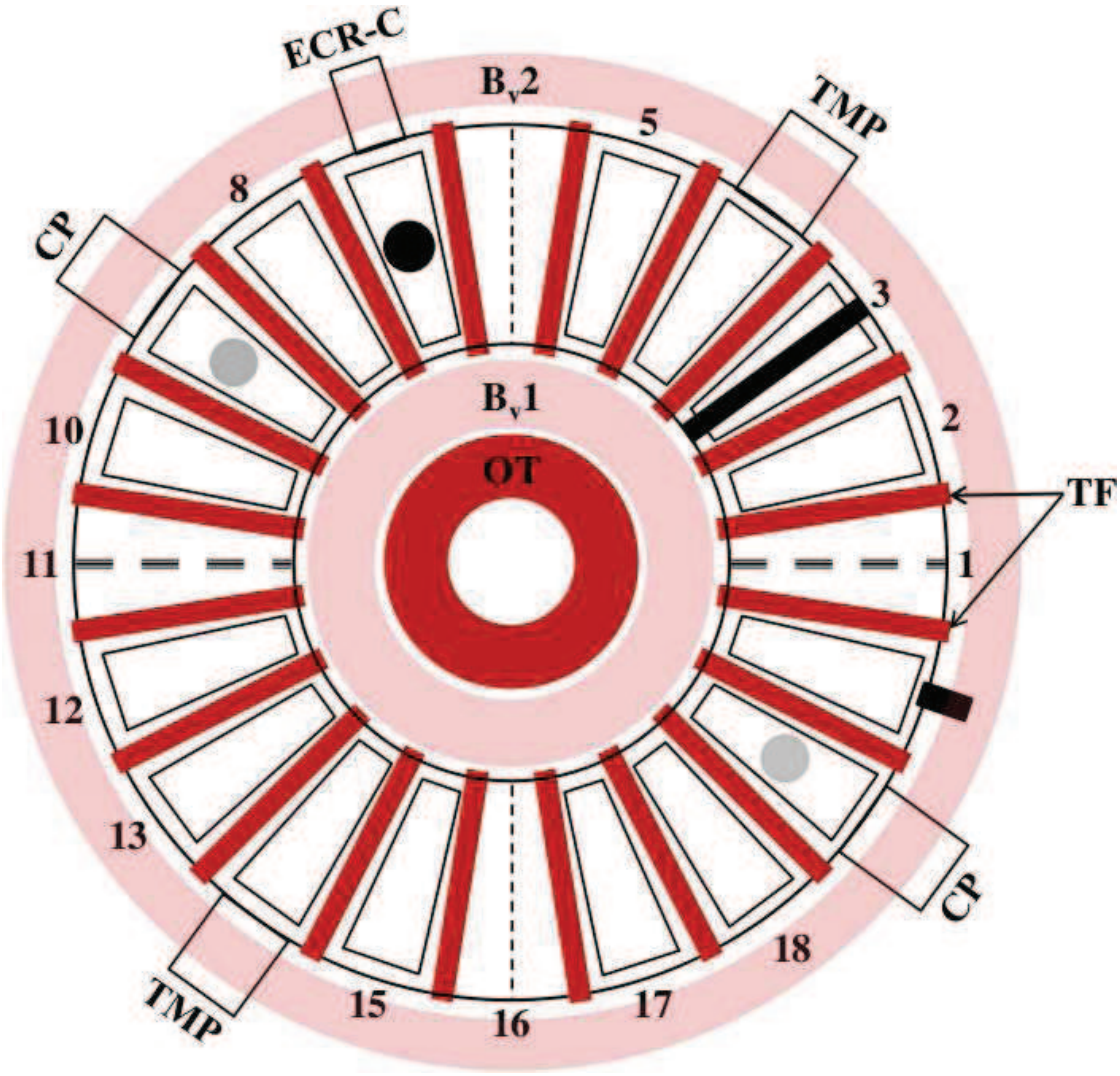

Figure 2.1: *Top view of the ADITYA tokamak. Twenty toroidal field coils "TF" are used to generate the B_T. Two pairs of vertical field B_v coils are used for the plasma position stability, shown in light red color and by labels "B_v1" and "B_v2". The main ohmic transformer "OT" is placed inside the central bore of the machine, shown by the red circular strip. The machine is made up of four quadrants and two isolations are provided, shown by triple dashed lines, and other two joints are conducting. The machine has twenty ports, and out of those four are used for the joints. For the vacuum, two cryo pumps "CP" and two turbo molecular pumps "TMP" are installed at the radial outboard ports. Limiter is shown by the black strip.*

particle flux can go to the boundary walls. To restrict the plasma flux on the whole surface of the plasma chamber, a limiter is inserted. ADITYA is a poloidal ring limiter tokamak, with 25 *cm* radius, and is made up of graphite tiles. The limiter protects the solid wall from the hot plasma. All the plasma surface interaction takes place at the limiter. Number of attempt have been made by modifying the limiter surface area in contact with the plasma, which helps in reducing sputtering [18, 49].

2.4 Electro-Magnets in ADITYA

The toroidal magnetic field B_T is the main confining field in the tokamak, shown in the Fig. 2.2. It can confine the charged particles and restricts their loss. However, only B_T is not enough to confine the plasma because of the curvature and gradient drift of charged particles. These drifts cause separation of charged particles at the top and bottom of the plasma column and generates a vertical electric field [see Fig. 2.2]. The resulting electric field together with the B_T causes the $E \times B$ drift of the plasma column and thus the column is unstable. This is overcome by the rotational transform of the magnetic field by superposing the poloidal magnetic field B_θ with the B_T. The B_θ twists the magnetic field lines into a helical shape. In such a situation the charge particles can travel along the field lines from top to bottom [see Fig. 2.3]. The B_θ is produced by the plasma current. In the helical magnetic field lines the particle at one poloidal plane arrives at the different poloidal location at the same poloidal plane after a toroidal rotation [see Fig. 2.4]. The change in the poloidal angle of the particle after one full toroidal rotation is called the rotational transform angle, ι. It can be defined by

$$\frac{\iota}{2\pi} = \frac{R}{r}\frac{B_\theta}{B_T}. \tag{2.1}$$

Inverse of the rotational transform angle ($2\pi/\iota$) is known as the safety factor.

ADITYA has three main field coils. They include toroidal field coils, vertical field coils, and ohmic field coils.

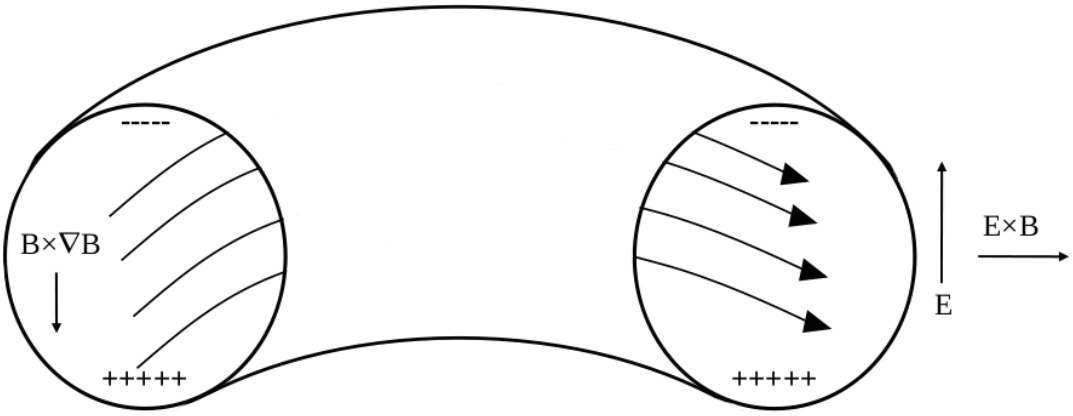

Figure 2.2: *The vertical charging of plasma column by $B \times \nabla B$ and Curvature drift. The B_T magnitude in the inboard side is large as compare to the outboard side, it gives a gradient in the B_T. This ∇B and the curvature in the B_T, both causes the vertical charging of the plasma column, by $\pm\frac{1}{2}v_\perp\rho_{i,e}\frac{\mathbf{B}\times\nabla\mathbf{B}}{B^2}$ and $\frac{mv_\parallel}{qB^2}\frac{\mathbf{R_c}\times\mathbf{B}}{R_c^2}$, where $\pm$ is for ions and electrons, $V_\parallel$, and $v_\perp$ are the parallel and perpendicular velocity components of the particles, $\rho_{i,e}$ are the ion and electron Larmor radius, q is the charge, and R_c is the radius of curvature. The vertical charging generates Electric filed (E), which causes $E \times B$ drift of the plasma column.*

2.4.1 Toroidal Field (TF) Coils

In ADITYA, twenty toroidal magnetic field (TF) coils are used, and each coil has six turns and can be used to carry a maximum of 50 kA current which is equivalent to the magnetic field of 1.5 T at the center. The field ripple at the plasma edge is < 2.5 %. The coils are shown in Fig. 2.1.

2.4.2 Ohmic Transformer

The gas discharge is produced and the plasma current (I_p) is driven by a loop voltage generated by an air core ohmic transformer with a capacity to carry a maximum of 20 kA and can store magnetic flux upto 0.6 Vs. The ohmic transformer consists of a main solenoid and compensating coils. The main solenoid having 290 turns is placed inside the bore of the machine [see Fig. 2.1] and all other compensating coils are placed equidistant from the machine center. The ADITYA design parameters of plasma current up to 250 kA and plasma duration of $\sim$ 300 ms require the flux swing of $\sim$ 1.2 Vs in the ohmic transformer. To minimize the stresses in

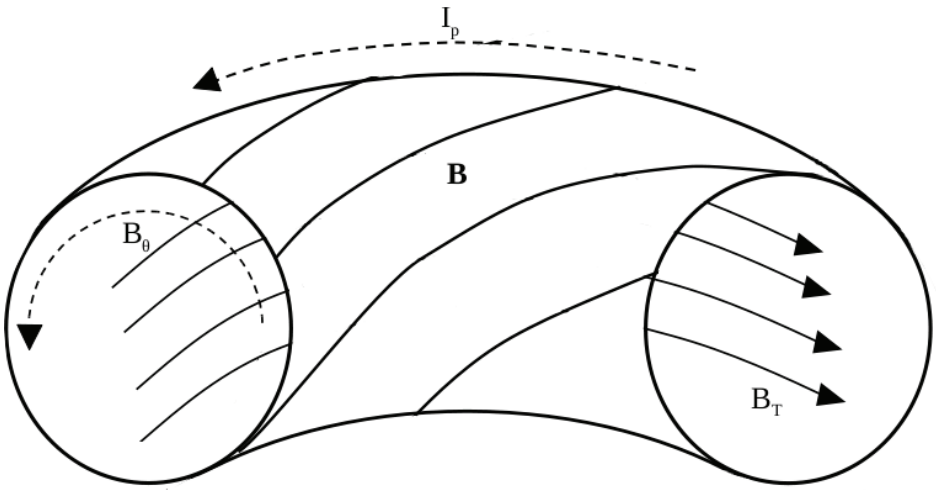

Figure 2.3: *The resultant total helical magnetic field* $\mathbf{B} = \mathbf{B_T} + \mathbf{B}_\theta$ *lines. The* B_T *is shown by the solid lines,* B_θ *by the dashed half circle and* I_p *is shown at the top by dashed line. The helical magnetic field lines connects the top and bottom of the plasma column, which causes the short circuiting of the vertical charging. In tokamaks, the poloidal magnetic field* (B_θ) *is generated by the plasma current, and* $B_\theta \ll B_T$.

the ohmic transformer, the flux is swung symmetrically from + 0.6 *Vs* to - 0.6 *Vs*.

The loop voltage along with the other important parameters are shown in Fig. 2.5 and 2.6. A high value of the loop voltage is required for breakdown of the gas; once the initial breakdown is over the loop voltage decreased to the lower value which is sufficient for the current to build up, temperature to rise, and overcoming the radiation barrier by the impurities. Once this is achieved, we need loop voltage just to sustain the plasma current as during this phase, the plasma resistance is very low. The last spike in the loop voltage is caused by the sudden fall in the plasma current, as both are magnetically coupled.

Lenz's law $e_L = -\frac{d\phi}{dt}$ gives a strong tool for magnetic measurements, where e_L is loop voltage and $\phi = BA$ is the magnetic field (B) flux through area A. The change in the magnetic field in time generates the loop voltage. The loop voltage can be measured by placing a toroidal loop around the vacuum chamber. It senses the change in the flux by ohmic transformer and plasma current. To increase the

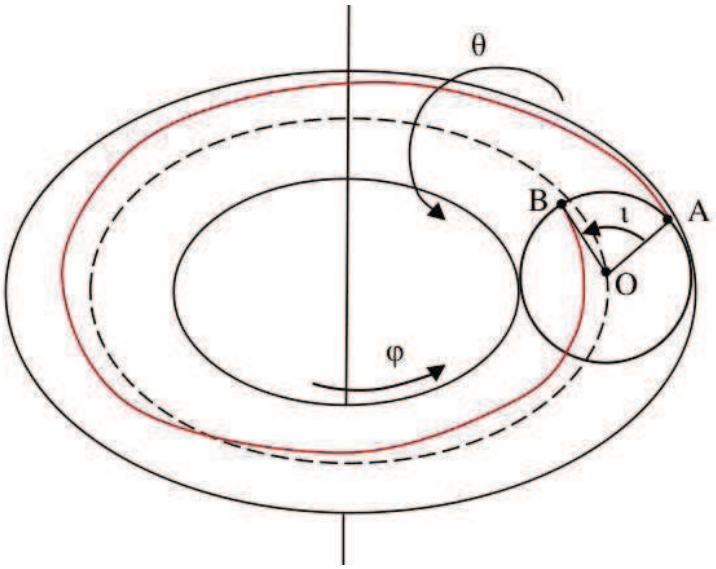

Figure 2.4: *The particle motion along the helical field lines. Particle starts from a poloidal position A and lands up at a different poloidal location B, after completing of one full toroidal (ϕ) rotation. The change in the poloidal angle of the particle after one complete toroidal rotation is called rotational transform ι. The dashed line is the 'locus of the center' of the machine.*

reliability of the measurement 13 loops are used in ADITYA. Each loop is passed through a guiding tube to ensure their position and safety. A coaxial cable RG188 A/U is used for the loop. The plasma current I_p is measured by using a Rogowski coil. The plasma current can be measured by using,

$$e_L = K_p \frac{dI_p}{dt} \tag{2.2}$$

$$I_p = \frac{1}{K_p} \int_0^t e_L dt \tag{2.3}$$

where $K_p = \frac{nA\mu_o}{2\pi r}$, n is the number of turns and A is the area of cross-section of each turn of Rogowski coil, a is the plasma column radius.

The time profile and magnitude of the I_p is very important as it is used to control the plasma position by the vertical magnetic field (see next subsection). The Rogowski coil has 4600 turns of Teflon insulated copper wire. A copper foil of

0.25 mm thickness is used to shield the Rogowski coil from external stray fields. The output of Rogowski coil is taken by the shielded twisted pair. The frequency response of the Rogowski coil is 1 kHz and the resolution is $1kA$. The sampling rate for both plasma current and the loop voltage signal is 5 kHz.

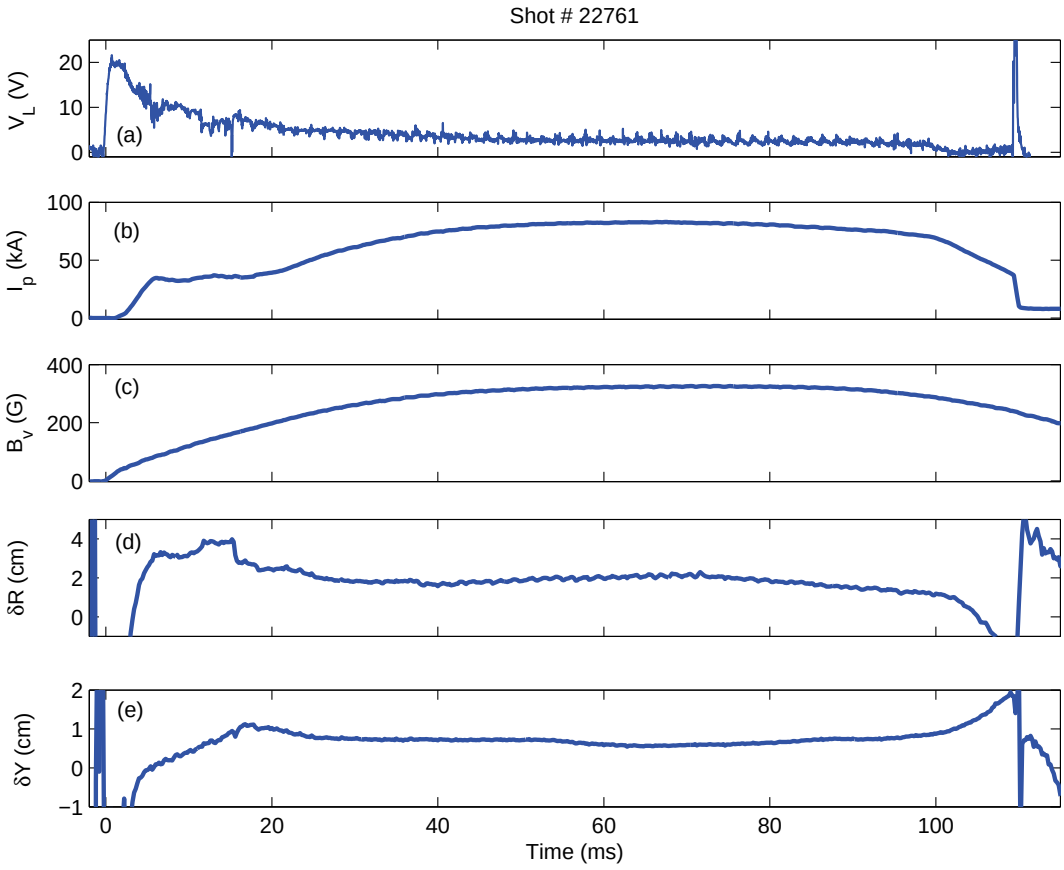

Figure 2.5: *Typical plasma shot of ADITYA, (a) loop voltage V_L, (b) plasma current I_p, (c) vertical field B_v, (d) horizontal shift in plasma column δR and (e) vertical shift in the plasma column δY. The V_L is measured by a toroidal loop outside the torus. I_p is measured by Rogowski coil placed around the torus in poloidal plane. The δR and δY are estimated by the four position coils placed around the torus in poloidal plane [see Fig. 2.9]. The estimation of the B_v for the ADITYA plasma equilibrium is carried out by the calculations shown in the "Vertical magnetic field" section. For the first hand calculation, we are using $I_p(kA) = \frac{B_v(G)}{4.05}$ for the B_v estimation, to control the plasma position for a given I_p.*

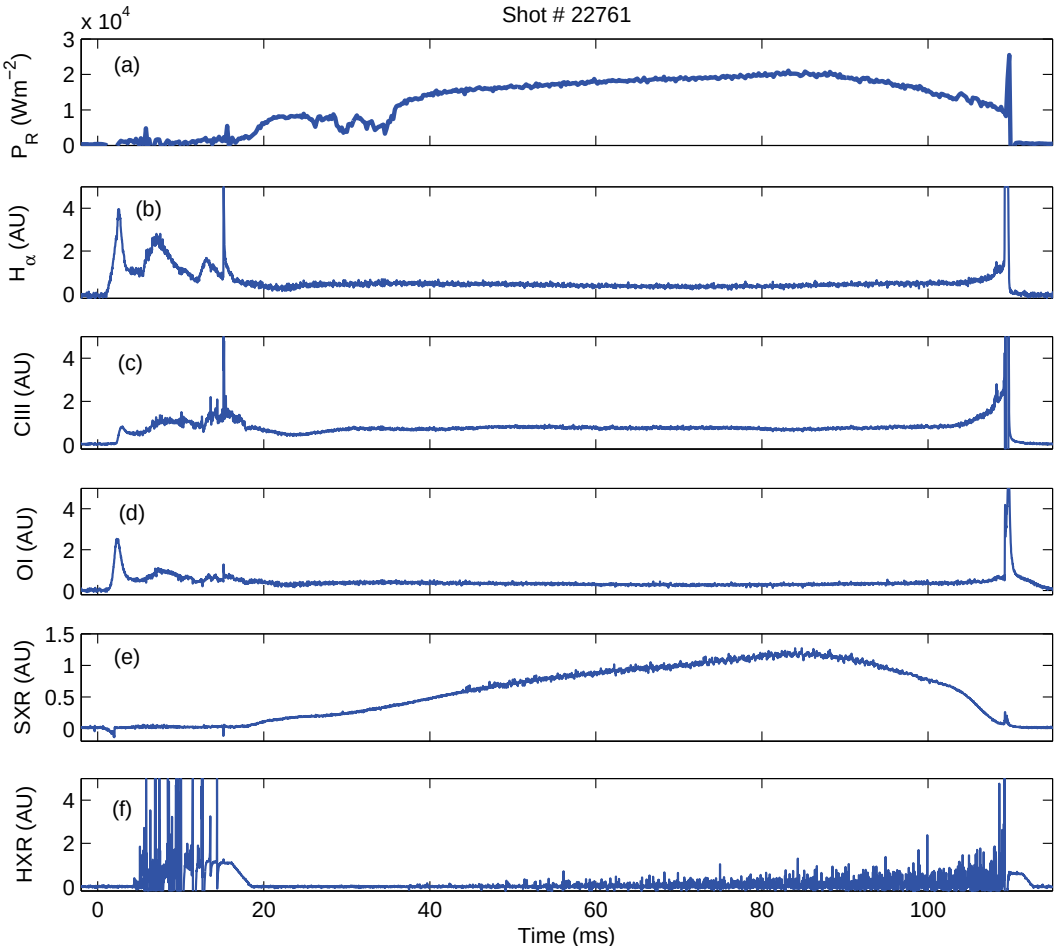

Figure 2.6: *Typical ADITYA shot data in continuation with Fig 2.5, (a) radiated power P_R measured by the bolometer, (b) H_α line radiation, (c) CIII line radiation, (d) neutral oxygen line radiation, (e) soft x-ray (SXR) and (f) hard x-ray (HXR). The H_α signal gives us the ionization information, the first peak shows the ionization of neutral H atoms. The second and third peak is the result of two small puff of hydrogen gas to increase the density, and to control the runaway electron generation, whose production is large at the first $\sim$ 15 ms because of large loop voltage. The CIII and OI measurements give information about the impurities burn through in the initial phase and we can compare the relative impurity level in the two shots just by CIII and OI signals. The SXR signal gives the core electron temperature. The HXR signal measures the presence of runaway electron.*

2.4.3 Vertical Field Coils and Plasma Equilibrium

The magnetic pressure on the inboard side is large as compared to the outboard side. This difference in the magnetic pressure gives plasma an outward shift. To

keep equal magnetic pressure at both inboard and outboard sides, we have to add an extra field which can enhance the field on the outboard side and reduce the field on the inboard side. It can be possible by the vertical field B_v [see Fig 2.7]. The B_v in ADITYA is generated by two pairs of field coils. Each pair of coils is placed symmetrically about the midplane. The maximum vertical field required for ADITYA is 0.4 T per MA of plasma current. The vertical field is used to control the plasma position, which depends on the I_p. To vary the B_v with the temporal evolution of I_p, we have a feed back system.

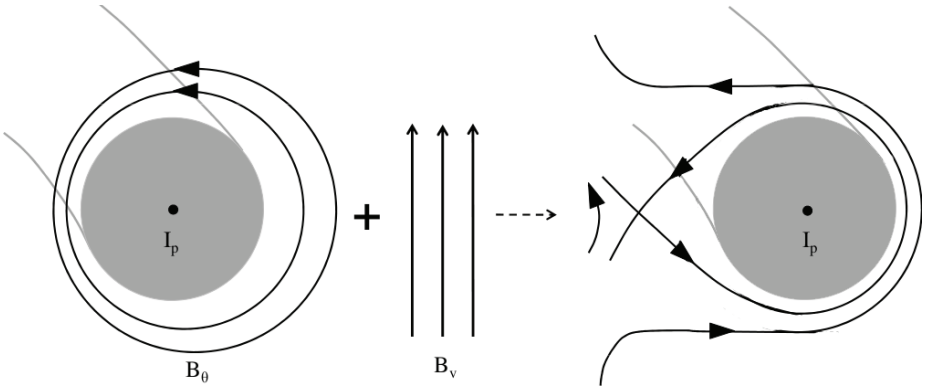

Figure 2.7: *The resultant of the poloidal magnetic field B_θ and the vertical magnetic filed B_v. The magnetic pressure due to B_θ at the inboard side is large as compared to the outboard side (shown by different spacing of circles of B_θ). This inboard-outboard side asymmetry in B_θ gives an outward shift to the plasma (hoop force). To balance this, we need to apply a external field which can increase the outboard B_θ and decrease the inboard side B_θ simultaneously.*

The need of the B_v and its magnitude can be seen by the force balance among the hoop force $F_h = \frac{\mu_o I_p^2}{2}\left(ln\frac{8R}{a} + \frac{l_i}{2} - 1\right)$ due to imbalance in the magnetic pressure on inboard and outboard side, the plasma expansion force $F_p = \langle p \rangle 2\pi^2 a^2$, the radial force because of plasma paramagnetic and diamagnetic nature $F_B = \frac{B_T^2(a) - \langle B_T \rangle^2}{2\mu_o} 2\pi^2 a^2$, and the force on the plasma current by the vertical field $F_v = I_p B_v 2\pi R$. Where l_i is the internal plasma inductance and $\langle\ \rangle$ is represents the average over cross-sectional area. For plasma position equilibrium (against the expansion in the radial direction) all these above forces should balance to give

$$\frac{\mu_o I_p^2}{4\pi R}\Big(ln\frac{8R}{a}+\frac{l_i}{2}-1\Big)+2\pi^2a^2\Big(\langle p\rangle+\frac{B_\phi(a)^2}{2\mu_2}\ -\ \frac{\langle B_\phi^2\rangle}{2\mu_o}\Big)+2\pi RI_pB_v=0. \quad (2.4)$$

From Eqn. (2.4), the vertical magnetic field for the position equilibrium can be expressed as,

$$B_v\ =\ -\frac{\mu_o I_p}{4\pi R}\Big(ln\frac{8R}{a}-\Lambda-\frac{1}{2}\Big) \quad (2.5)$$

where, $\Lambda=\beta_p+\frac{l_i}{2}-1$, and $\beta_p=\frac{\langle p\rangle}{B_\theta^2(a)/a\mu_o}$ is the poloidal plasma beta. To know the equilibrium position and shape of the plasma, we need an equation which can tell position and shape of the plasma in the form of magnetic field lines. This is done by solving Grad-Shafranov equation that connects the plasma current distribution and pressure in terms of magnetic flux. It determines the equilibrium configuration of the magnetic field as follows:

$$R\frac{\partial}{\partial R}\frac{1}{R}\frac{\partial\psi}{\partial R}+\frac{\partial^2\psi}{\partial z^2}=-\mu_oR^2\frac{\partial p(\psi)}{\partial\psi}-\mu_o^2f(\psi)\frac{\partial f(\psi)}{\partial\psi} \quad (2.6)$$

where $\psi=(1/2\pi)\int\mathbf{B}_\theta.\mathbf{ds}$ is the equilibrium flux function and $f(\psi)=RB_\phi$. The 1^{st} order solution of Grad-Shafranov equation gives the circular magnetic flux surfaces and the 2^{nd} order gives elliptic surfaces. The 1^{st} order solution in inverse aspect ratio gives the magnetic flux function ψ, equilibrium vertical magnetic field B_v, plasma shift Δr and the field outside the plasma [50, 51]. The Magnetic field components in the r and θ directions are:

$$B_\theta=\frac{1}{R_o}\frac{\partial\psi}{\partial r}=\frac{1}{2\pi}\Big[\frac{\mu_oI}{r}+\frac{1}{R_o}\Big(-\frac{1}{2}\mu_oI(ln\frac{8R}{r})-\frac{C_1}{r^2}+C_2\Big)cos\theta\Big] \quad (2.7)$$

$$B_r=-\frac{1}{R_o}\frac{1}{r}\frac{\partial\psi}{\partial\theta}=\frac{1}{2\pi R_o}\Big[-\frac{1}{2}\mu_oI\Big(ln\frac{8R}{r}-1\Big)+\frac{C_1}{r^2}+C_2\Big]sin\theta \quad (2.8)$$

where $C_1=a^2\Big(\Lambda+\frac{1}{2}\Big)$, $C_2=-\Big(ln\frac{8R_o}{a}+\Lambda-\frac{1}{2}\Big)$ and $\Lambda=\beta_p+\frac{l_i}{2}-1$. These two equations [Eqn. (2.7) and Eqn. (2.8)] are the basis of plasma position determination. Thus, the equilibrium position depends on current profile and kinetic energy of plasma particles along with B_v and I_p [52].

2.4.4 Vertical Stability

In the last subsection, we have find out that for plasma stability against the radial expansion we need a vertical field. A uniform B_v can not give the stability against the vertical shift in plasma position. For stability in vertical shift, we need to have a radial magnetic field. This radial magnetic field can be generated by the B_v curvature. The stability depends on the direction of the curvature, as one curvature can increase the accidental vertical shift and other can move the plasma back to machine center. We can put the stability condition in terms of curvature index or the decay index as

$$n = -\frac{R}{B_v}\frac{\partial B_v}{\partial R} > 0. \tag{2.9}$$

Curvature in the B_v is necessary to control the vertical shift but if the curvature is large it will make the plasma horizontally unstable against an accidental change in the horizontal position of the plasma column. It puts an upper limit on the decay index which is [50]

$$0 < n < \frac{3}{2}. \tag{2.10}$$

In ADITYA, vertical field coil positions and ampere-turns are chosen to make n in the range of 0.4 to 1.2.

2.5 Preionization

For gas breakdown, we normally depend on stray electrons, which are present in the atmosphere because of ionization by cosmic rays. These electrons help in the avalanche process. If we put some extra electrons other than stray electrons, we can reduce the applied voltage and the breakdown time. The process involved in providing the source of extra electrons before the main ionization is defined as preionization. Preionization is used extensively in all tokamaks, including ADITYA. In tokamaks, the preionization is done by the microwaves, ECR (electron cyclotron resonance), and by the filaments. In the presence of the preionization, there is less delay in the startup, low loop voltage for discharge, and hence less consumption of Vs, and less runaway electrons production [53, 54, 55, 56].

In ADITYA, we are using thorium coated tungsten wire of 0.5 mm diameter and 12 mm length. The heating current in the wire is 19 Ampere and biasing with respect to the vessel is 150 V. All these values have been chosen after number of small experiments to optimize the use of preionization filament to reduce the ionization time. We have observed that if we do not use the preionization filament the ionization time increases 2-3 times. Thorium oxide coating of the tungsten filament or its 0.5 % to 2.0 % doping to the tungsten can increase the electron emissivity by order of three, by reducing the work function of the tungsten wire [57]. The preionization filament is shown in Fig 2.8.

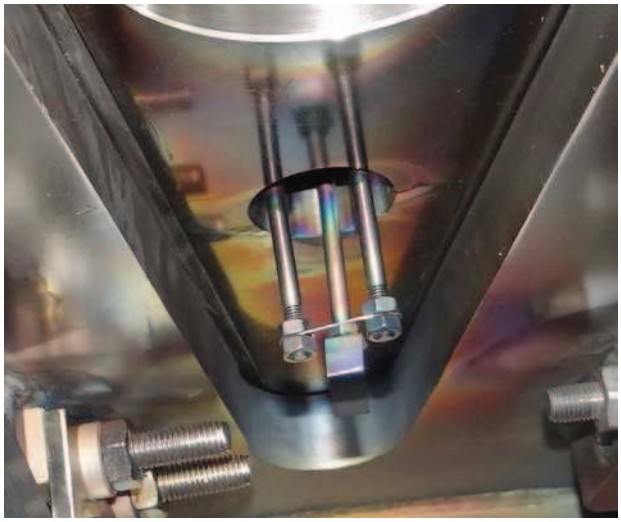

Figure 2.8: *Tungsten filament for the preionization in the ADITYA tokamak. It is of 0.5 mm diameter and 12 mm length. It is installed at the top port of the machine. Filament is negatively biased by 150 V with respect to the vessel. The heating is carried out by a supply of 19 Ampere current. The biasing voltage and current is chosen after optimization with the number of preionization experiments in ADITYA.*

2.6 Vessel Cleaning

Plasma purity is a very important issue in tokamaks. The impurity level of plasma discharge mainly depends on the vessel condition before the plasma discharge. The vessel condition includes the wall contamination, which in the forms of monolayers

of oxygen and carbon [58]. The oxygen and carbon are the most abundant impurities in the tokamaks. The level of impurities should remain below a permissive level, as the high level of impurities takes away the useful energy of the plasma and makes the temperature rise difficult [49].

The adsorbed impurities at the vessel walls desorb thermally and by the chemical reactions with the plasma hydrogen. In this way, water (H_2O) carbon di-oxide (CO_2) and hydrocarbons are released and get dissociated in the main plasma and become the main sources of C and O impurities. Impure plasma is also susceptible to high production rate of runaway electrons [59]. They will further create problems in the discharge formation and in the temperature build up of plasma. Thus, the control of impurity level is a necessary step to have a good quality plasma discharge [60]. The requirements for the discharge cleanings are: low density, low temperature, and evenly distributed plasma with high pumping speed. This ensures that the impurity source molecules (H_2O, CO_2, etc.) are pumped without dissociation, ionization and redeposition onto the walls.

The main discharge cleaning techniques are: glow discharge cleaning (GDC), pulse discharge cleaning (PDC), and electron cyclotron discharge (ECR) cleaning. In ADITYA, we are using all of them along with occasional baking, bronization and lithimization.

2.6.1 Glow Discharge Cleaning

The glow discharge cleaning (GDC) involves biasing of the vessel with respect to positive electrode [61]. In ADITYA, we are using $\sim 700V$ bias for two electrode with respect to the vessel, which is grounded. In GDC, a low electron temperature plasma is created with hydrogen or helium. In ADITYA we are using the hydrogen GDC. The vessel walls are bombarded with the hydrogen ions; these ions desorb the adsorbed impurities in the form of hydrogen compounds: H_2O, CH_4 etc., from the vessel walls. After desorption, these will be pumped out by the continuous pumping. The GDC parameters in ADITYA are given in Table 2.2.

Table 2.2: ADITYA Glow Discharge Parameters

1.	Current Density	J_s	$\sim 0.05\ Am^{-1}$
2.	Electron Temperature	T_e	~ 2 eV
3.	Anode Voltage	V	$\sim 400V$
4.	Magnetic field	B	Nil
5.	Plasma Density	n_e	$\sim 1 \times 10^{15}\ m^{-3}$

2.6.2 Pulse Discharge Cleaning

Pulse discharge cleaning uses low density, low temperature and small duration tokamak plasma discharges. The main drawback of the PDC is that it put lots of stress on the machine by the repetitive number of shots. The ADITYA pulse discharge cleaning parameters are given in the Table 2.3.

Table 2.3: ADITYA Pulse Discharge Cleaning Parameters

1.	Ohmic Capacitor Voltage	$\sim 5\ kV$
2.	Toroidal Magnetic Field	$\sim 0.1\ T$
3.	Hydrogen Pressure	$\sim 2{\times}10^{-5}\ Torr$
4.	Pulse Duration	$\sim 4\ ms$
5.	Pulse Repetition Rate	$\sim 900\ pulse/hour$

2.6.3 Electron Cyclotron Resonance Cleaning

Electron cyclotron resonance (ECR) heating cleaning is performed by using a standard magnetron source of 2.45 GHz frequency in extraordinary mode [62]. A continuous microwave is launched perpendicularly to the toroidal magnetic field [see Fig. 2.1]. ECR cleaning parameters for ADITYA are given in Table 2.4.

Table 2.4: Electron Cyclotron Resonance Cleaning Parameters

1.	Resonance Frequency	$\sim 2.45\ GHz$
2.	Toroidal Magnetic Field	$\sim 0.035\ T$
3.	Hydrogen Pressure	$\sim 2{\times}10^{-5}\ Torr$
4.	Electron temperature	$\sim 5\ eV$

2.7 ADITYA Basic Diagnostics

Tokamak diagnostics can be divided into two categories: basic and experimental. The basic diagnostics are necessary for the machine operation and the experimental diagnostics are experiment specific. The basic diagnostics involve spectroscopic measurement of various impurity lines, magnetic measurements (loop voltage, plasma current, plasma position measurement, vertical magnetic field measurement), core plasma density measurement (microwave interferometry) etc. In this section, we will discuss briefly the various basic diagnostics of ADITYA.

2.7.1 Position Measurement

The shift in the position of the plasma column with respect to the limiter center can be measured by the use of position probes [63]. To get the both horizontal (δR) and vertical (δY) shift, a set of four poloidally separated magnetic probes at one toroidal location is required; two for the horizontal shift and other two for the vertical shift. The position of four probes are shown in Fig 2.9(a) and Fig 2.9(b). These probes are placed in corners in ADITYA because of the lack of space in the middle of the four sides of the chamber, which would be the ideal position of probes [52]. In ADITYA, the co-ordinates $(\delta R, \delta Y)$ of the plasma centroid position with respect to the limiter center is determined by using equations derived by Raju [52].

2.7.2 Hard X-Ray Detection

Hard X-ray's are related to runaway electrons in the tokamak plasma. When these runaway electrons hit a material target, they produce a continuous spectrum of bremsstrahlung. The label "hard" comes from their ability to penetrate the materials. Typically, photons with energy larger than 100 keV fall into the hard X-ray category. In the runaway dominated discharges, the appreciable content of the plasma current is carried by a small percentage of electrons. The runaway electrons are mostly generated during the plasma breakdown; once they pick up the progress they can be effectively coupled with the ohmic transformer because of low resistance, and consume all the useful loop voltage and hamper the plasma

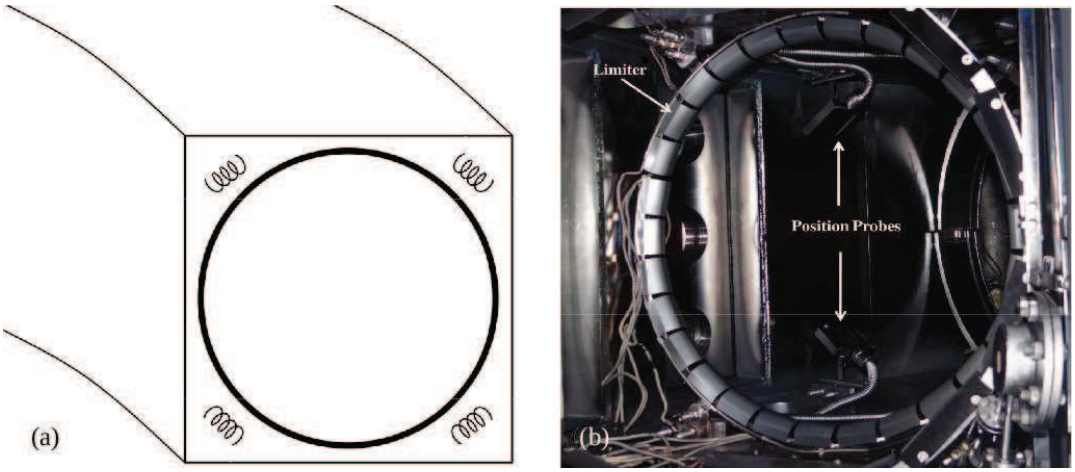

Figure 2.9: *Plasma position measurement coils and limiter, (a) The plasma position measurement coils schematic, shown by spirals. Limiter is shown by the thick black circle. The location of coils should be at the midplane of outboard/inboard and top/bottom. In ADITYA, these coils are installed at the corners because of space limitation at the respective midplanes. (b) The limiter and the position coils in ADITYA. In this photograph only two outboard coils can be seen, and the other two are not in the view. The coils are shielded by the SS box to protect them from the heat and the capacitive pick ups.*

density build up. They are the electrons with the velocity larger than a critical velocity for which the accelerating force is larger than the collisional drag force. Once they cross this limit, there is nothing which can stop continuous acceleration of these electrons. The maximum encounter of runaway electron occurs with the limiter. To measure the energy of these radiations, we have put a hard X-ray detector, which faces the limiter. The detector is the NaI(Tl) detector housed in a heavy but movable Lead cylindrical hollow block. This is done to make sure that the detector is getting the radiations from the limiter side, not from the other sources. The calibration of the detector is done by the standard source of the Cobalt. Normally in ADITYA, it is kept at the 1 V output signal corresponding to the 1 MeV of radiations. The hard X-ray signal is shown in the Fig. 2.6(f).

2.7.3 Electron Temperature Measurement by Soft X-Ray

The soft X-ray (SXR) gets its name from their low penetrating power. The SXR photon energy $h\nu$ is typically in the range 100 $eV \leq h\nu \leq 10$ keV. The intensity

of SXR is a measure of hotness (thermal radiation) of plasma. The expected maximum electron temperature in ADITYA is 350-400 eV. We are using soft X-ray technique to measure the chord averaged temperature of plasma by the method of absorption foil ratio. In ADITYA, the soft X-ray system consists of a 3 mm pin-hole camera with 16 silicon surface barrier detectors (SBD) placed in a linear array, viewing the plasma through a pin-hole geometry [64]. The pin hole is covered by 25 μm Beryllium foil to filter all the radiation below 1 keV. The whole system is pumped by turbomolecular pump and separated from main ADITYA vessel by a gate valve; this is to insure the scattering free path for radiation from the plasma. The energy sensitivity of SBD is 300 eV to 10 keV. The soft X-ray signal is shown in the Fig 2.6(e).

2.7.4 Density Measurement by Microwave(μ) Interferometry

In ADITYA, we have 100 GHz, 7 channel homodyne interferometer system to measure the cord average density and its radial profile. It is based on change in the plasma refractive index. In this technique, one beam is passed through the plasma, and a second one, a reference beam, is used to get the phase shift by the electron density variation. The phase shift, $\delta\phi = \int (N-1)\frac{\omega}{c} dl$, where N and ω are the refractive index and microwave frequency, is directly related to the electron density. The maximum possible density in the ADITYA is $\sim 2 \times 10^{19}\ m^{-3}$, and the plasma frequency is $\sim 50\ GHz$, which is less then the microwave frequency. In the case when the plasma density is larger than the critical density n_c, N becomes imaginary, and the interferometer ceases to function.

2.7.5 Radiated Power Measurement by Bolometry

Bolometry is the most widely used technique to measure radiated power in tokamaks. Generally, two types of bolometer detectors are used in tokamaks. These are the metal foil resistors and the silicon photodiodes [65, 66]. The basis of the measurements are the change of resistance of the detector with the radiation. In recent years, the use of silicon photodiodes, popularly knows as the AXUV photodiodes, in bolometers become very popular because of their fast response time

($\sim \mu s$) as compare to the metal foil detectors ($\sim ms$). It was found in ADITYA that 20% - 40% of the total input power is radiated [67]. The bolometer system comprises of two cameras for the measurement of the radiation power loss and radiation emission distribution. The detectors being used are AXUV photodiodes. The two cameras are mounted on a radial port and a top port at the same toroidal location. Both the cameras have arrays of 16 detectors and see the whole poloidal cross section of the plasma through a slit. The spatial resolution of this camera is 4 cm at the vessel mid-plane and the temporal resolution is 0.2 ms. The detector arrays are mounted in UHV chambers and connected to the electronics in a compact housing mounted on the machine port. The electronics includes current-to-voltage converters, amplifiers, filters, and drivers for all photodiodes.

2.7.6 Spectroscopy

Spectroscopy in tokamaks involves the study of various emission line radiations, like $H_\alpha, H_\beta, CIII, OI$ etc. In ADITYA, the H_α, OI, and $CIII$ are observed regularly at the top/bottom and in/out parts of the limiter. These measurement are carried out to estimate the neutral influx. The $CIII$ lines from the opposite sides of limiter give us the information about the plasma movement. Visible bremsstrahlung continuum radiation is used to estimate the Z_{eff}. The UV radiation is monitored for the higher charge states of impurities, like OVI, CV, and $FeXV$. Both grazing incidence and normal incidence monochromators are used to measure the intensity of resonance line radiation from impurity, and a multitrack spectrometer is used for time and space resolved visible emission spectroscopy [68].

2.8 Various Limits in Tokamak Operation

Tokamak plasma equilibrium is governed by power balance and pressure balance. The rise in loss of plasma energy through radiation or increase in the plasma pressure and its gradient above some certain level gives rise to various types of instabilities, which may give rise to plasma disruption. Some of the basic limits in the ADITYA tokamak plasma operation are; density limit and q limit [51]. The beta limit is small in ohmically heated ADITYA plasma and therefore it is ignored.

2.8.1 Density Limit

The density limit puts an upper limit to the maximum achievable density in the tokamaks. The limit on the density in tokamaks depends on the mechanism of the strong edge cooling. The exact mechanism behind the density limit is still uncertain. The power imbalance between heating and power loss plays important role. It is observed in different tokamaks that a very dirty plasma can not be operated at high densities [69]. It has been observed that by operating in the peaked density profile, we can increase the line averaged density; this is the evidence of strong edge role in setting the density limit. The density upto 1.4 n_G is observed [69], where n_G is the Greenwald density limit [69]

$$n_G\ (10^{20} m^{-3}) \equiv \frac{I_p\ (MA)}{\pi a^2\ (m^2)}. \tag{2.11}$$

Good wall conditioning and boronization methods also help in increasing in the achieved density [69]. There is a lower limit on the density profile which is set by the runaway electrons. This lower limit is $\sim 5 - 10\%$ of the upper limit. The estimated density limit in ADITYA is $\sim 5 \times 10^{19}\ m^{-3}$, we normally operate at $\sim (1 - 2) \times 10^{19}\ m^{-3}$ to avoid the density limit.

2.8.2 Safety Factor Limit

The safety factor limit is related to the plasma current density profile. For the safety against the kink mode instability and the tearing mode instability the safety factor at the plasma boundary $q(a)$ should be $>\ 2$ [70]. In ADITYA, the $q(a) \sim 3.5$, which is above the lower limit [15, 45, 71].

Chapter 3

Probe Diagnostics

3.1 Introduction

Diagnostics are the heart of experimental plasma studies. They gives us eyes to see the plasma. They can be basically divided into two categories: active diagnostics and passive diagnostic. The active diagnostics are in direct contact with the plasma (i.e., electrical probes) or they can send a signal inside the plasma to get its response (i.e, lasers). On the other hand, the passive diagnostics collect the information from plasma in the form of radiations emitted by the plasma. Passive diagnostics includes spectroscopy, infrared diagnostics, optical fibers, and visible camera. Our present studies of SOL plasma properties along with plasma flows makes use of single Langmuir probes, triple Langmuir probes, and Mach probe. Plasma sheath plays important role in all these probes measurements. In this chapter, we discusses about the plasma sheath and various probes.

The chapter is organized as follows: Sec. II is devoted to the plasma sheath study, Sec. III discusses about the Langmuir probe basics, Sec. IV discusses the triple probe basics and Sec. V describes the Mach probe.

3.2 Plasma Sheath

Plasma sheath is the positive or negative charge layer formed by the plasma around any object inserted into plasma, in this process plasma tries to shield itself from any

source (object) of potential other than plasma potential. In shielding process, the plasma forms a protective layer around a potential source in such a way that the bulk plasma does not feel its presence. If the source is at the positive potential with respect to the plasma potential, V_P, the plasma electrons rush to the object and form a negative charge layer around it, in such a way that the potential just outside the sheath is around the V_P. Similarly the ions form a positive charge layer around the negative potential source with respect to the V_P. This positive/negative layer is called sheath. The collection of the electron in the sheath region is by the electron thermal speed, $\sqrt{2T_e/m_e}$. On the other hand, in case of ion sheath, collection of ions at the sheath is at higher than the ion thermal speed. This acceleration to the ions is provided by the presheath region, discussed in the next section.

3.2.1 Presheath and Bohm Criterion

In plasma, the ions are much heavier than the electrons (e.g. 1837 times, for H) and normally the ion temperature (T_i) is much smaller than the electron temperature T_e. Both of these makes ions thermal speed very less as compared to the electrons. The effect of large difference in thermal speeds can be seen in ion sheath formation. The ion sheath formation can be explained by a floating object [1]. In plasma, if we put any floating object, it will charged negative by electrons, as the electrons are more mobile than ions. They reach to the object first and charge it negative before ions start responding. Once it charges negative, it behaves as a $-ve$ potential source. Here we can take the $-ve$ potential source with respect to the V_P inspite of the floating object. Now the plasma ions start moving to shield it. For ion sheath formation, ion flux should be sufficiently large, which is possible only when there is mechanism which can accelerates the ions to match up with the electron flux. This acceleration of ions is done by the presheath. It is region beyond the sheath, in which a residual electric field exists and which accelerates ions to the ion sound speed (C_s) [see Fig 3.1]. In the floating mode the current collected by the probe is zero, as the ion current is equal to the electron current.
The concept of presheath was given by the Bohm, to explain the observed difference in the measured and expected values of the ion saturation current [72]. This difference is because of collection of ions at the sheath edge at the higher speed

[1] Floating object is an object whose resistance w.r.t ground is $\sim M\Omega$.

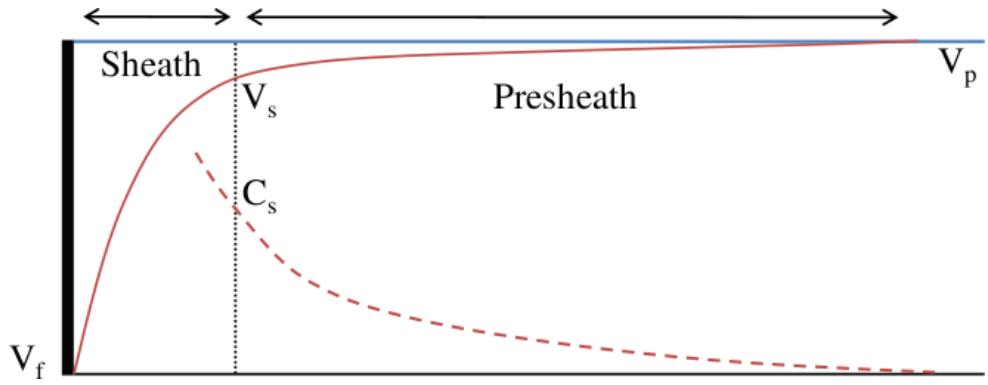

Figure 3.1: *Ion sheath formation at the interface of plasma and floating material. The region before the sheath is called presheath, which accelerates the ions to the ion acoustic speed C_s at the sheath edge. The potential beyond the presheath is the plasma potential. The sheath thickness is $\sim 5\lambda_D$, where λ_D is the Debye length. The speed of ions are shown by the dashed lines. For the electron sheath formation their is no need of presheath region.*

than the ion thermal speed, which is assumed to be the collection speed of ions before Bohm explains the existence of a presheath region beyond the sheath region. It can be explained as follows:

When the probe is biased $-ve$ such that, $eV_B < \frac{T_e}{2}$, electrons are still able to overcome this retarding field and get collected at the probe. It means plasma around the probe is still quasineutral and no ion sheath forms for $0 < -eV_B < \frac{T_e}{2}$. The formation of sheath starts when V_B increases to more $-ve$ than $\frac{T_e}{2}$. Now most of the electrons are repelled by the probe. Here the potential at the sheath edge is $\sim (V_B - \frac{T_e}{2e})$. Between the sheath and undisturbed plasma, there is a quasineutral region in which probe potential penetrates, and where the ions gain energy of the order of the potential drop in this region. This is called presheath. The potential drop in the presheath is $\sim \frac{T_e}{2e}$. Therefore the minimum required energy by the ions, for the formation of an ion sheath is $W_+ \geq \frac{T_e}{2e}$. This criterion was deduced by Bohm. The electron density at an arbitrary point in the presheath of a probe: $n_e = n_{es} exp\big(\frac{e(V(x)-V_s)}{T_e}\big)$, where the n_{es}, V_s and $V(x)$ are the electron density at the sheath edge, sheath potential, and potential at any arbitrary point in the presheath respectively. Assuming $n_{is} = n_{es} = n_s$, where n_{is} and n_{es} are the ion and electron density at the sheath edge. Using the continuity and Poisson's equation, Bohm

drives a condition for the ion sheath formation at the probe, which is:

$$|eVs| \geq \frac{T_e}{2} \tag{3.1}$$

This is Bohm criterion for ion sheath formation. Now, the ion saturation current for sufficiently negative probe can be written as:

$$I_s = eA_s n_{is} v_{is} \rightarrow I_s = eA_s n_\infty \sqrt{\frac{-2eV_s}{M_i}} exp\Big(\frac{eV_s}{T_e}\Big) \tag{3.2}$$

where v_{is} and n_∞ are the ion speed at the sheath edge and density of the undisturbed plasma, and A_s is the sheath area. For $V_s = -\frac{T_e}{2e}$, Eqn. 3.2 becomes

$$I_s = 0.61eA_s n_\infty \sqrt{\frac{T_e}{M_i}} \tag{3.3}$$

which is greater than the previous one (i.e., $I_s \sim A_s n_\infty e\sqrt{T_i/M_i}$) [73]. We can see from above that ion saturation current depends on the electron temperature , so we can not calculate ion temperature from the Langmuir probe. In ADITYA, we use $I_s = 0.5 n_\infty A_s C_s$ to estimate the plasma density, where $C_s = \sqrt{(T_e + T_i)/M_i}$ and T_i is the ion temperature [73].

3.2.2 Sheath Thickness

We can get an approximation of the sheath thickness (X_s), by assuming that electron density is negligible in the sheath, and solving the Poisson's equation (by putting $dV(x)/dx = 0$ at the sheath edge). We get:

$$\frac{X_s}{\lambda_d} = \frac{2}{3}\Big[\frac{2}{exp(-1)}\Big]^{1/4}\Big[\Big(\frac{-eV_B}{T_e}\Big)^{1/2} - \frac{1}{\sqrt{2}}\Big]^{1/2}\Big[\Big(\frac{-eV_B}{T_e}\Big)^{1/2} + \sqrt{2}\Big] \tag{3.4}$$

putting $V_B = V_f$, it is ~ 3.75 for hydrogen plasma, and then the sheath thickness is $\sim 4\lambda_D$ [73]. Thus the sheath thickness order is comparable to the Debye length (λ_D)[1].

[1]Debye length is associated with the plasma screening property; it is the length over which the potential falls to 1/e.

3.3 Langmuir Probe

Langmuir probe (LP) is a small metal electrode inserted into the plasma. This electrode may be biased or floating. The current collected by the electrode gives the information about the local electron temperature, plasma density, floating potential, plasma potential, electron distribution function and by special arrangement it can also determine the plasma flows (Mach probe). It is the simplest in term of design and at the same time, one of the complex diagnostics in terms of data analysis. Langmuir probe is named after the noble prize winner Irving Langmuir [74]. It can be cylindrical, spherical, or flat in shape. The size and shape of LP is governed by the plasma properties like: plasma density, electron temperature, ion larmor radius, and electron larmor radius ($\rho_{i,e}$). The LP dimensions should be small enough so that the probed plasma is not affected by the probe itself. This puts an upper limit on the probe size. On the other hand the lower limit of probe radius is constrained by the requirement, $a >> \lambda_d$. The choice of probe material should consider the plasma duration and T_e. For T_e ($\sim$ 2-3 eV) steel or iron metal is sufficient, but for high temperature plasma $\sim$ 20 eV, molybdenum or tungsten metal should be used. However, Langmuir probe can not be used in hot plasma continuously. In the presence of magnetic field there are three cases, (i), weak magnetic field ($\rho_{i,e} \gg a$), (ii) moderate magnetic field ($\rho_e \ll a \ll \rho_i$), and (iii) strong magnetic field ($\rho_{i.e} \ll a$), where a is the probe dimension. The weak magnetic field and the moderate magnetic field case can be explained by the theory; the strong magnetic field case is generally avoided because of lack of simple theoretical explanation [73].

The main advantage of using Langmuir probe over other diagnostics is that it gives local measurement of plasma parameters. This advantage of LP, however, is directly connected to its shortcomings. For local measurements, probe has to be inserted in plasma by means of a probe holder whose area is larger than the probe itself. This arrangement forms a wall (boundary) in addition to the existing plasma boundaries and in the close proximity, plasma parameters may deviate from those in the absence of the probe.

There are three commonly used Langmuir probe arrangements, (i) single Langmuir probe, (ii) double Langmuir probe, and (iii) Triple Langmuir probe. The single

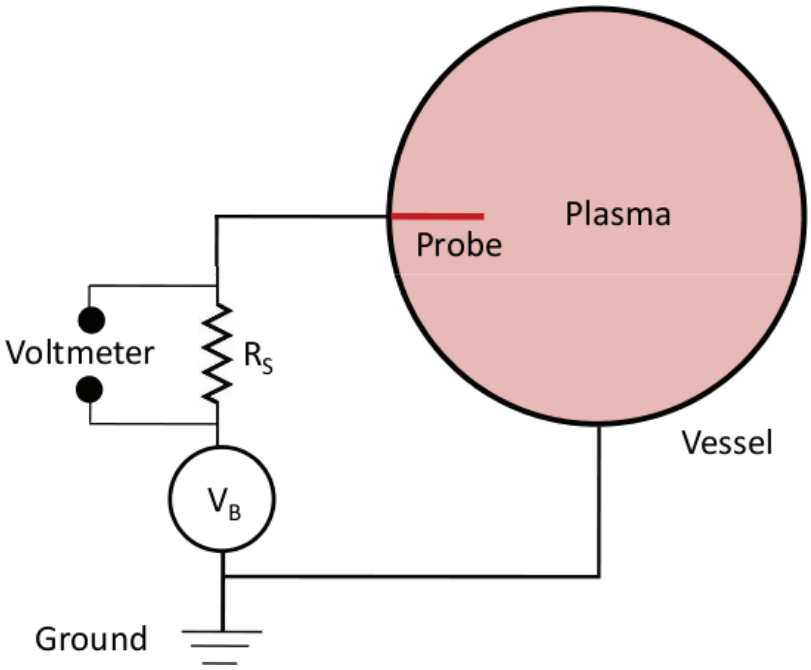

Figure 3.2: *Schematic of probe biasing scheme, where V_B and R_s are biasing voltage and sensing resistance to measure probe current, respectively. The probe is biased with respect the the vessel. The value of the sensing resistance should be chosen in such a way that the potential drop in R_s does not effect the potential at the probe tip. For the floating potential (V_f) measurement, there is no need of V_B and the value of R_s should be chosen to minimize the the current drawn by the probe. The choice of R_s for V_f measurement depends on the sheath resistance [75, 76], for tokamak like plasma R_s should be of the order of $\sim M\Omega$ and for the low density and low temperature plasma it should be of the order of $\sim 100\ M\Omega$.*

Langmuir probe is the most fundamental and widely used probe; the other two are extended versions of the same one. Once Langmuir probe is inserted in the plasma it collects both ion and electron currents depending on its biasing. The schematic of probe biasing is shown in Fig. 3.2.

The use of Langmuir probe is bounded by certain number of assumptions:

- The plasma is infinite, homogeneous and quasineutral in the absence of the probe.
- Electrons and ions have Maxwellian velocity distributions, with $T_e >> T_i$.

- The mean free paths of electrons and ions are large as compare to the sheath thickness.
- Charge particles do not react with the probe material.
- The region of deviation from the undisturbed values forms a space charge sheath.
- The sheath thickness is small as compare to the lateral dimensions of the probe.

3.3.1 The Probe Characteristic

The current drawn by the probe is measured as a function of the applied bias voltage. The resulting relation between the probe current and the bias voltage is called the probe characteristic. A sketch of ideal probe characteristics is shown in Fig. 3.3. The V_B is the bias voltage, its variation from negative to positive with respect to the plasma potential scans the plasma electron and ion distribution function.

We can divide the Fig. 3.3 in three parts, left flat part of the characteristics shows the ion saturation current (I_s) collected by the probe, right side shows the electron saturation current (I_{es}), and the middle exponential part is a combination of both ion and electron current. The potential at which the current collected by the probe is zero is called the floating potential (V_f). Between V_f and V_p, there is a transition to electron current dominated region. At the V_p, both electron and ions are collected at the probe thermally. At the V_P there is no sheath around the probe. The density distribution of the electrons in the sheath is governed by $n_e = n_\infty exp\Big(\frac{e(V_B - V_P)}{T_e}\Big)$, for $V_B < V_P$. The random electron current to the sheath is given by $\sim \frac{1}{4} e n_\infty v e A_s$. The probe current can be written as:

$$I_p = I_s + I_{es} exp\Big(\frac{e(V_B - V_P)}{T_e}\Big) \tag{3.5}$$

where $I_{es} \sim \frac{1}{4} n_\infty C_e A_s$ is the electron saturation current and C_e is the electron thermal speed. Here, the ion current is assumed constant and equal to the I_s, and the electron current I_e varies according to the V_B, below the V_P. The V_B

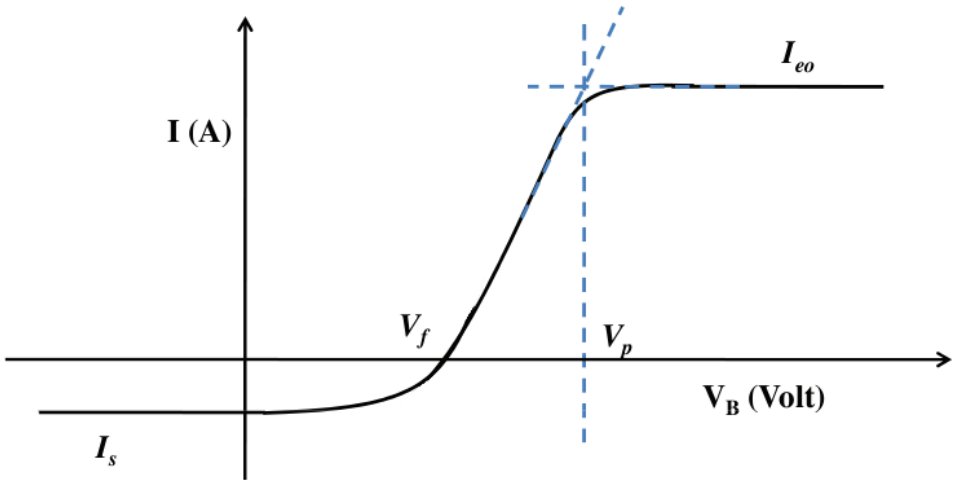

Figure 3.3: *The probe current variation sketch with respect to the bias voltage V_B. This variation is normally referred as the probe characteristics. Probe current can be divided into three regions: (a) ion saturation current I_s region, below the floating potential V_f, in this region only ions are collected at the probe and nearly all the electrons are repelled by the probe, (b) increasing part, this part is combination of ion current and increasing electron current, and (c) electron saturation current I_{eo}, above the plasma potential V_P, in this region all the ions are repelled and only electrons are collected at the probe. The two dashed line represents the tangent to the rising part of the current and on electron saturation current, the intersection of two tangent lines is the V_P.*

just above V_P repels all the plasma ions. In this region, electron sheath is formed around the probe and the current to the probe is I_{es}. Below the V_P, probe starts repelling electrons according to the magnitude of their thermal speed; low speed electrons are repelled near to the V_P and very high energy or tail electrons of the Maxwellian are repelled only at high negative V_B as compared to the V_P. In this region, the ion collection remains ineffective and remain nearly constant, except very near to the V_P, where ion sheath starts depleting [see Fig. 3.4]. Ion current show some decrement near to the V_P, as the V_B here is not sufficient to accelerate to the plasma ions to Bohm speed. Sometimes the saturation parts of the probe characteristics does not show the current saturation. It is caused by finite thickness of the sheath which changes with the V_B. In case of thick sheath the area of the probe should be corrected. In such cases, the collection area for spherical probe is $A_s \sim A_p(1 + X_s/a)^2$ and for cylindrical probe is $A_s \sim A_p(1 + X_s/a)$. For $X_s \ll a$,

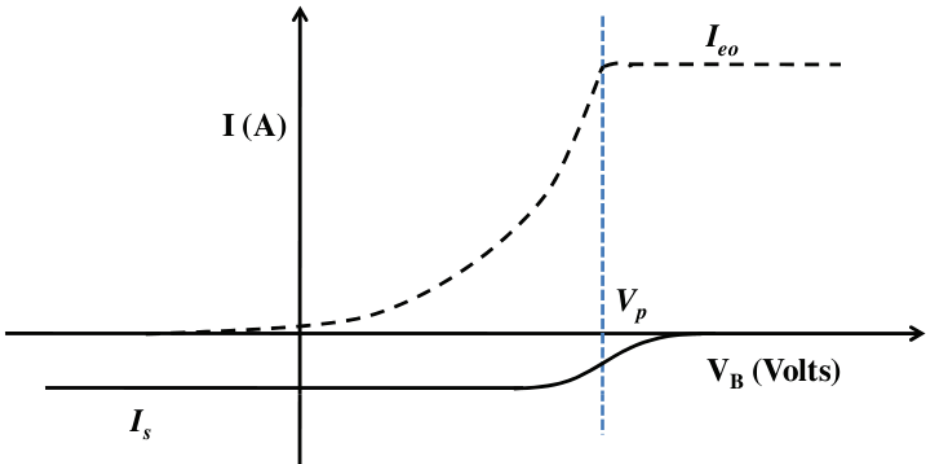

Figure 3.4: *A sketch of the electron and ion current variation with respect to the probe bias voltage. Above the V_P, the probe current is only the electron current as the ion current is zero. On the other hand, the electron current to the probe at large $-ve$ V_B is zero, here the only current to the probe is the ion saturation current. At the intermediate biasing (between V_f and V_P), both electron and ion current contributes to the probe current.*

the A_s becomes A_p in both cases [73].

3.3.2 Collision Effects

In the discussion of the current collected by the probe, we have not included the effect of collisions. The electron saturation current to the probe when collisions are negligible is

$$I_{es} \sim \frac{1}{4} e A n_\infty C_e \tag{3.6}$$

In collisional plasma, current to the probe is less than the above mentioned value [73]. I_{es} in collisional plasma can be written as:

$$I_{es} \sim \frac{1}{4} n_\infty e A_p C_e \left(\frac{1}{1 + \frac{C_e a}{4D}} \right) \tag{3.7}$$

where a is the radius of the probe, D is the diffusion coefficient $l = \frac{3D}{v}$, and l is the mean free path. Then

$$I_{es} \sim \frac{1}{4} n_\infty e A_p C_e \left(1 + \frac{3a}{4l} \right)^{-1}. \tag{3.8}$$

For $l >> a$, collisions are ignorable, and for $l << a$ collisions are going to reduce the current collected by the probe. In case of highly ionized plasma, collisions with the neutrals can be ignored; then the mean free path is $l \sim (n_\infty \lambda_D^3)\lambda_D$. By using the plasma condition ($n_\infty \lambda_D^3 >> 1$), we can get $l >> a$. In weakly ionized plasma, collisions with the neutrals are sufficient, and the l may be shorter than λ_D. In ADITYA, collisions are ignorable, as $l \sim 2\ m$.

3.3.3 Analysis of Probe Characteristics to get T_e and n_∞

- Subtract the value of I_s from I_p to get I_e, which is governed by the $I_e = I_{es} exp\Big(\frac{e(V_B - V_P)}{T_e}\Big)$ below V_P. Assuming that V_P is known. In ADITYA, the I_p measurement are carried out near the V_f and in the I_s region. For this, we used $I_p = I_s\Big[1 + exp\Big(\frac{e(V_B - V_f)}{T_e}\Big)\Big]$.
- Take the log of the electron current and plot it against the V_B,
- The slope of this log curve is proportional to $1/T_e$.
- By using this value of T_e in ion saturation current, we can evaluate plasma density, n_∞.
- If the Debye length is significant compared to probe radius a, then the effective area may be corrected with this value of λ_D. This provides a correct value of the plasma density. This situation is avoided by choosing the probe size so that thin sheath approximation is valid.

3.4 Triple Langmuir Probe

The triple Langmuir probe (TLP) as the name suggest, is a combination of three Langmuir probes, shown in Fig. 3.5. It consists of the three Langmuir probes, identical in size and shape, and at different static potential. The whole probe arrangement is floating, so the current collected by the TLP is zero [77, 78, 79]. It means relatively small disturbance of the plasma results, just as in the case of the double probe [80]. Temperature measurement by single Langmuir probe requires rising bias voltage (voltage sweep) and a long procedure to calculate T_e from the measured probe current. The TLP gives us freedom from the voltage sweep and

the cumbersome post processing of data. In single Langmuir probe, temperature measurement is limited by the time period of the sweep bias voltage; there is no such restriction for TLP and the time response limit is imposed by the intrinsic response time of the probe. Triple probe popularity comes from its ability to give instantaneous T_e measurement, and easy data evaluation procedure.

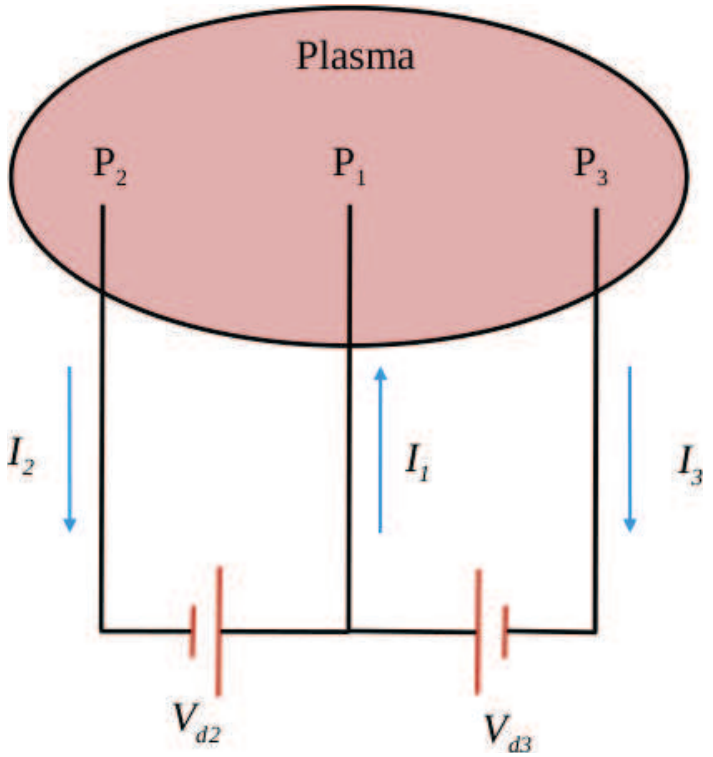

Figure 3.5: *Triple probe biasing scheme. Two floating power supplies are used to bias the probes. To keep the whole system floating, all measurements should be carried out carefully by taking one of the three probes as a reference (P_1, is reference probe).*

The pins of triple probe are placed in close proximity of each other. This proximity is determined by the sheath thickness. Its lower limit is such that, there should not be any overlapping of sheaths of the adjacent probes. All other assumptions and precautions are same as for the single Langmuir probe. Shape of the three probes can be cylindrical, spherical, or plate. The plasma is assumed same at all the three pins locations. If the plasma is not same at the all the probe locations then the difference in V_P gives rise to extra current in the probes.

3.4.1 Triple Probe Theory

Figure 3.6 shows bias voltage at the three probe pins P_1, P_2, and P_3 with respect to the V_P. From Fig. 3.5 and 3.6, we can write:

$$I_1 = I_2 + I_3 \tag{3.9}$$

$$V_{d2} = V_2 - V_1 \tag{3.10}$$

$$V_{d3} = V_3 - V_1 \tag{3.11}$$

Where I_1, I_2 and I_3 are the current in the pins and V_1, V_2, and V_3 are bias potentials. If two probe voltages V_{d2} and V_{d3} are zero, the potential of each probe at its floating potential V_f and no current flow into each probe. If two negative voltages, V_{d2} and V_{d3} are externally applied to the probes P_2 and P_3 with reference to the probe P_1 as shown in the Fig. 3.5, then the potential of the probes are lower than the floating potential V_f and currents flowing into them are mainly the positive ion current. Conversely, for this situation, the potential of the P_1 is higher then the V_f, so the current flowing into it is mainly an electron current. The current flowing into the three probes at any instant can be written as:

$$-I_1 = -A_p J_{es} exp(-\phi V_1) + A_p J_s(V_1) \tag{3.12}$$

$$I_2 = -A_p J_{es} exp(-\phi V_2) + A_p J_s(V_2) \tag{3.13}$$

$$I_3 = -A_p J_{es} exp(-\phi V_3) + A_p J_s(V_3) \tag{3.14}$$

where, $\phi = \frac{e}{T_e}$, $J_{es} = \frac{1}{4} n_\infty e \sqrt{\frac{2T_e}{m_e}}$ electron saturation current density, $J_s = exp(\frac{-1}{2}) n_\infty e C_s$ is the ion saturation current density and A_p is the surface area of probes.

3.4.2 Electron Temperature (T_e) Estimation

There are two ways to measure the T_e from the triple probe. For simplicity it is assumed that $J_s(V_1) = J_s(V_2) = J_s(V_3)$, now from Eq. (3.12), (3.13) and (3.14), we get:

$$\frac{I_1 + I_2}{I_1 + I_3} = \frac{1 - exp(-\phi V_{d2})}{1 - exp(-\phi V_{d3})} \tag{3.15}$$

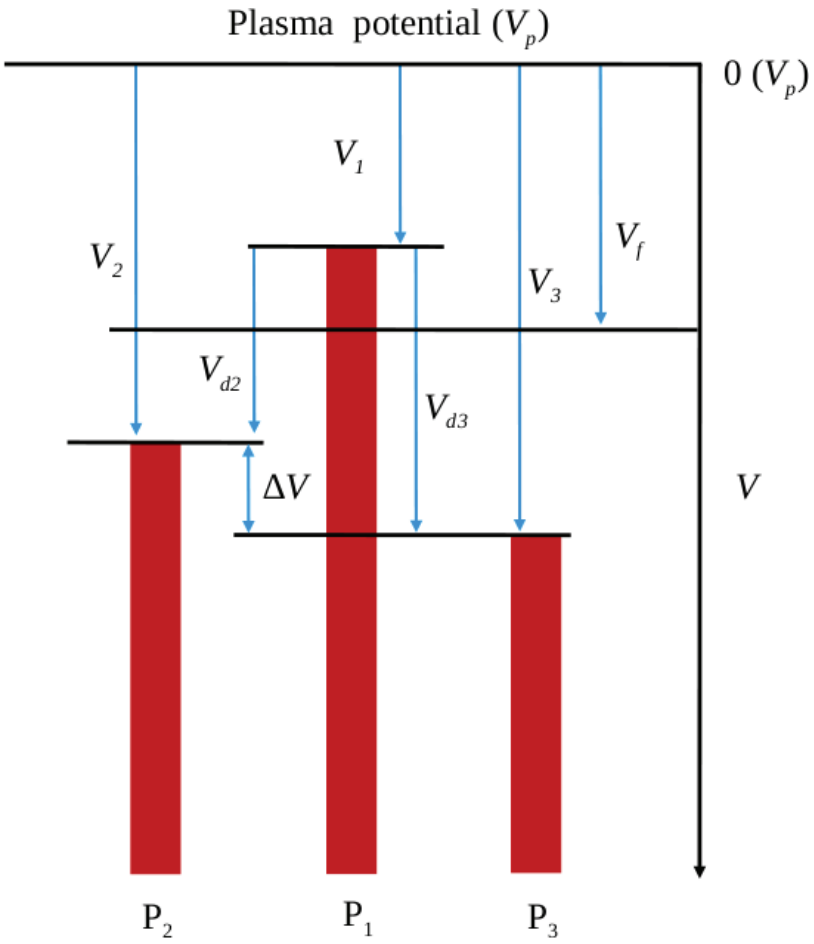

Figure 3.6: *Potential diagram of three probe with respect to the plasma potential* V_P. *Here probes* P_2 *and* P_3 *are biased* $-ve$ *with respect to the probe* P_1. *This biasing shift the potential of probes* P_2 *and* P_3 *below the floating potential and raises the potential of probe* P_1 *above the floating potential. As a whole the complete system is floating.*

and it can be used to determine the value of T_e.

In the direct display method, one of the three pins of TLP say probe 2, is kept at the floating potential by removing the external voltage source V_{d2} as shown in the Fig. 3.7. This means that the condition $I_2 = 0$ and thus $I_1 = I_3 = I$. Thus Eq. (3.15) reduces to:

$$\frac{1 - exp(-\phi V_{d2})}{1 - exp(-\phi V_{d3})} = \frac{1}{2} \tag{3.16}$$

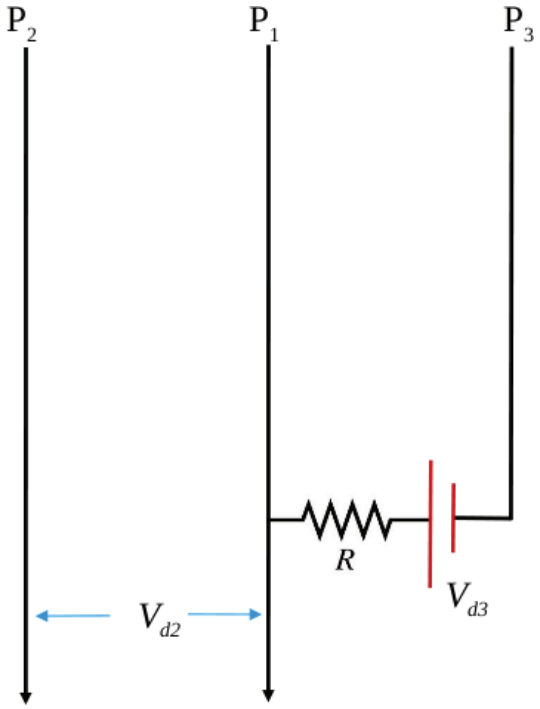

Figure 3.7: *Triple probe biasing scheme for direct display of T_e, where V_B and R is biasing voltage and sensing resistance to measure probe current, respectively. This whole system is floating and the measurements are carried out with respect to the P_1 probe. The voltage measured across the R gives information about the plasma density and the floating potential of probe P_2 (V_{d2}) with respect to the probe P_1 gives the T_e.*

Since V_{d3} in Eq. (3.16) is a fixed voltage which is externally given by a floating power supply, it is possible to determine the electron temperature (T_e) solely from the measurement of V_{d2}. The electron temperature may be displayed directly on an appropriate voltmeter for the case of stationary plasmas, or on an oscilloscope for the case of time varying plasmas.
In Fig. (3.8) the T_e variation with the V_{d2} is shown [77]. The T_e measurements remains linear to the V_{d2} for $T_e < V_{d3}/2$ and divergent for $T_e > V_{d3}/2$ [77]. For $T_e << V_{d3}$, Eq. 3.16 becomes:

$$T_e \simeq \frac{V_{d2}}{ln2} \tag{3.17}$$

The above equation gives us the direct measurement of T_e from V_{d2} for $V_{d3} \geq 2T_e$.

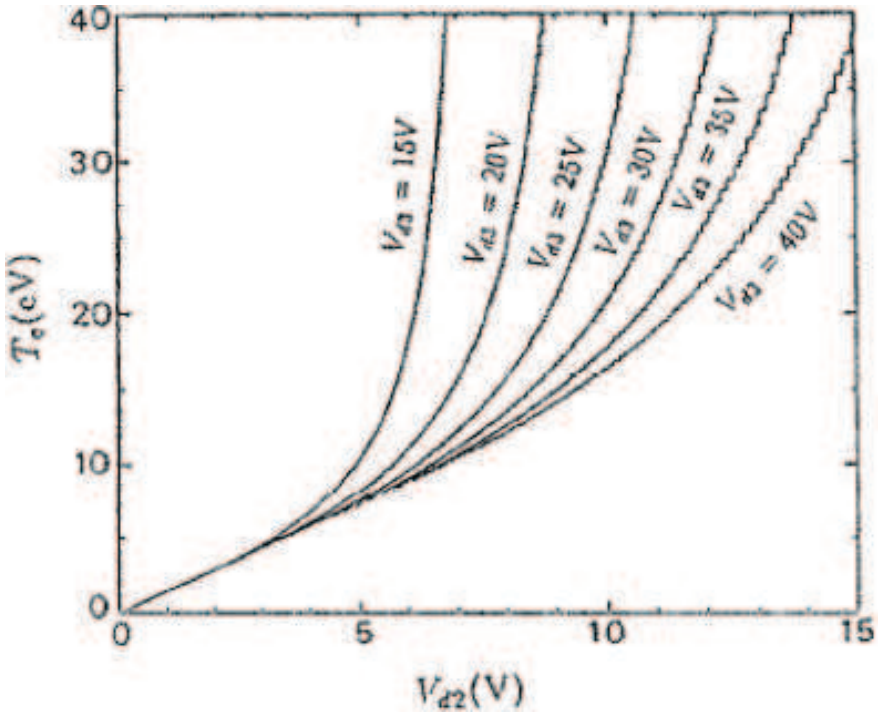

Figure 3.8: *The relation between T_e and measured V_{d2} at different biasing voltages, V_{d3}. It shows the range of V_{d3} for which, T_e is directly proportional to the V_{d2}. The biasing voltage (V_{d3}) should be atleast $\geq 2T_e$, to have a good linearity between T_e and V_{d2}.*

3.5 Mach Probe

The Mach probe is a combination of two Langmuir probes separated by an insulator. It measures the asymmetry in the density in flowing plasma at the upstream and downstream sides of the probe. Here, the upstream and downstream directions represent the two sides of the Mach probe along the ion flow direction (upstream) and opposite to it (downstream) [see Fig. 3.9]. The concept of Mach probe has been developed from the idea of direction dependent collection of probe current by the Langmuir probe in flowing plasma [74]. The probe current is different at different angles with respect to the magnetic field in the presence of plasma flows [81, 82].

After Langmuir, number of models were proposed for the Mach probe. They includes, Hudis and Lidsky [83], Harbour and Proudfoot [84], Stangeby [85] and

Hutchinson [86, 87].

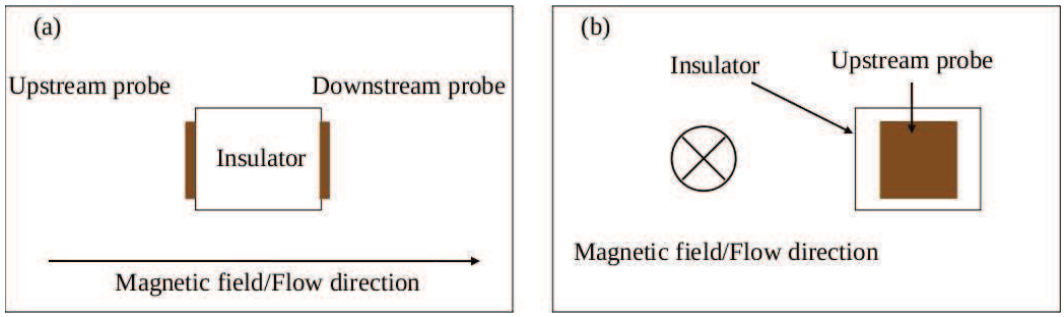

Figure 3.9: *Schematic of Mach probe in magnetic field, (a) top view of Mach probe, (b) view from one side (upstream). The upstream probe is the probe which faces the flow. The nomenclature of upstream and downstream is not universal. In tokamaks, sometimes the probe faces the plasma current is defined as the upstream and the other one as the downstream.*

Hudis and Lidsky gave a one dimensional kinetic model for unmagnetized Mach probe ($\rho_i > a$), to determine the flow speed from the upstream and downstream ion density difference [83], where ρ_i and a are the ion gyroradius and probe radius respectively. The estimated densities at the upstream direction (positive sign) and downstream side (negative) of the Mach probe are given below.

$$n_i = n_\infty \; exp\Big(\frac{-1}{2} - \frac{(v_t \pm v_\parallel)^2}{C_s^2}\Big) \tag{3.18}$$

Where n_i, v_t, $v_\parallel$ and C_s are ion density at the probe, thermal speed of ions, flow speed and ion sound speed respectively. By taking the ratio of ion saturation current derived by the Hudis and Lidsky, Mach number ($M = v_\parallel/C_s$) can be determined by using

$$\frac{J_{UP}}{J_{DN}} = exp\Big(4\sqrt{\frac{T_i}{T_e}}M\Big). \tag{3.19}$$

It can be written as $\frac{J_{UP}}{J_{DN}} = exp(kM)$, where $k = 4\sqrt{\frac{T_i}{T_e}}$. There are some drawbacks of this model , as it depends on the ion temperature which means that we can estimate the ion temperature from current ratio if the flow speed is known. Another demerit is that it is a one dimensional model, whereas ion collection at the probe in the unmagnetized plasma is a three dimensional process.

Stangeby and after that Hutchinson gave models for the magnetized ($\rho_i < a$) Mach probe [85, 86, 87]. The Hutchinson's model includes the viscosity effect by assuming momentum diffusivity equivalent to the particle diffusivity, which is ignored previously in the Stangeby's model. This makes Hutchinson's model more realistic. The theory gives the Mach number in terms of ratio of upstream and downstream currents of Mach probe. In magnetized plasma, the ion collection by the probe across the field lines is possible by the cross field diffusion, shown in Fig. 3.10. Because of this, the presheath is highly elongated along the field lines to compensate the in flux collected by the probe from the diffusion flux.

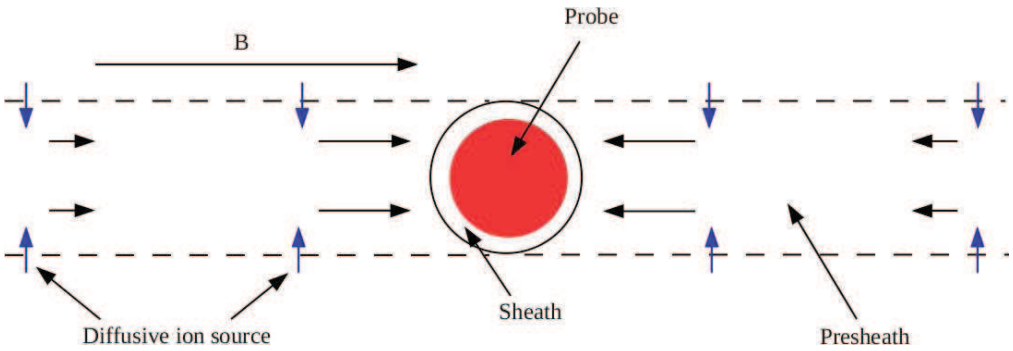

Figure 3.10: *Schematic of ion collection by probe in strong magnetic field ($\rho_i < a$). The ion flux collected at the probe is provided by the cross field diffusion of the ions in the presheath region, indicated by the "Diffusive ion source". Presheath is elongated along the field direction. The length of this collection region along the field lines depend on the diffusion coefficient ($D_\perp$), ion acoustic speed (C_s) and on probe length (l). The collection length is given by $\sim C_s l^2/D_\perp$.*

In 1-D model Hutchinson used a quasineutral two fluid plasma [86]. Approximation for the one dimensional solution are: n_i, v_i and V_P single functions of x, which is the mean value over the lateral extension of the collection region. The collection radius is assumed to be equal to the probe radius (a). The diffusion of particles in the collection region is represented by the source of particles in the equations. This source determines the parallel extent of the collection region. Considering that all the electrons are reflected by the negative biased probe, electron density is governed by Boltzmann factor

$$n_e = n_\infty exp\left(\frac{eV(x)}{T_e}\right) \tag{3.20}$$

where, the subscript ∞ denotes the plasma quantities far from the collection region. The $V_P = 0$ is assumed. The diffusive rate of ion exchange between collection region and the outer plasma is $\Omega \sim \frac{D_\perp}{a^2}$. The rate of loss of particles which has already got some acceleration in the presheath region is $\Omega n_i(x)$, and rate of particle gain is Ωn_∞. Thus, the one dimensional continuity and momentum equations are:

$$\frac{d(n_i v_i)}{dx} = \Omega(n_\infty - n_i) \tag{3.21}$$

$$n_i m_i v_i \frac{dv_i}{dx} + m_i v_i \Omega(n_\infty - n_i) = n_i ZeE - \frac{dp_i}{dx} + m_i v_i \Omega(n_\infty v_\infty - n_i v_i) \tag{3.22}$$

respectively, where Ze is the ion charge, p_i is the ion pressure, and $E = -\frac{dV(x)}{dx}$ is the electric field. By substituting the $\frac{dV(x)}{dx}$ from Boltzmann equation, $C_s = \sqrt{\frac{T_i + ZT_e}{m_i}}$, and using isothermal ions approximation (ignoring $\frac{dT_i}{dx}$), the momentum equation becomes:

$$n_i v_i \frac{dv_i}{dx} = -C_s^2 \frac{dn_i}{dx} + \Omega n_\infty (v_\infty - v_i) \tag{3.23}$$

This equation and the continuity equations are the two governing equations for the presheath [86]. After making some transformations, we can get,

$$\frac{dn}{dM_\parallel} = n.\frac{(1-n)M_\parallel - (M_{\parallel\infty} - M_\parallel)}{(M_{\parallel\infty} - M_\parallel)M_\parallel - (1-n)} \tag{3.24}$$

where, $n = \frac{n_i}{n_\infty}$, $M_\parallel = \frac{v_\parallel}{C_s}$ and $v_\parallel$ is the flow speed. Equation (3.24) [86] has no exact analytical solution. An approximate analytical solution can be written as:

$$n \approx exp(M_{\parallel\infty} - M_\parallel). \tag{3.25}$$

and hence, the ratio of the current densities of the two sides of Mach probe can be written as:

$$R = \frac{J_{UP}}{J_{DN}} = exp(\frac{M_{\parallel\infty}}{K}) \tag{3.26}$$

and

$$M_{\parallel\infty} = Kln(R) \tag{3.27}$$

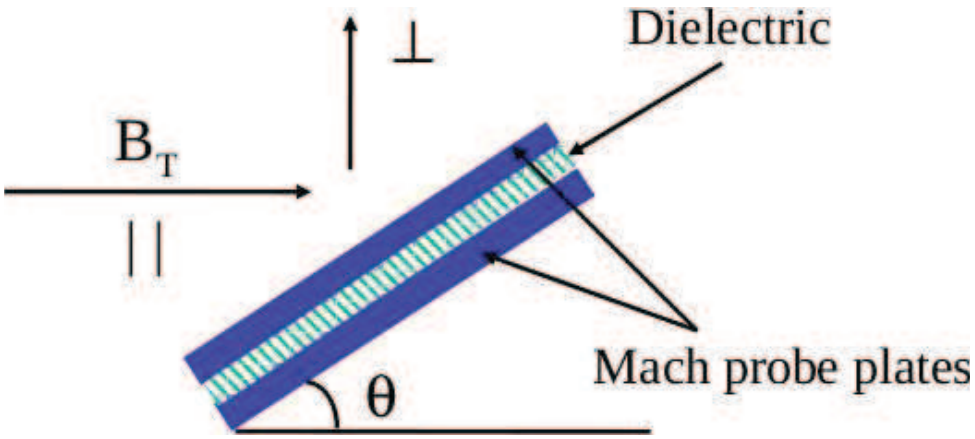

Figure 3.11: *Mach probe arrangement to measure the* $\parallel$ *and* $\perp$ *flows simultaneously. Here the* θ *is the angle of Mach probe with magnetic field. The* $\parallel$ *and* $\perp$ *are with respect to the magnetic field* B_T *direction.*

where the $K \sim$ (0.43-0.45) and independent of the ion and electron temperature. Above, we have considered that there is only parallel flow to the magnetic field, and no perpendicular flow, and the Mach probe is kept along the field direction. The above equation modifies in the presence of perpendicular flow, when we put Mach probe at a certain angle with the magnetic field. The Mach probe at an angle $> 10^o$ with the magnetic field can be used to determine the perpendicular plasma flows also, see Fig (3.11) [88]. In this case, the collection density at the magnetic presheath edge (MPSE)[1] for the Mach probe aligned at a angle other than 90^o is modified by the perpendicular flows, if any [88].

We can estimate both parallel and perpendicular flows simultaneously along with the other direction flow components by using specially designed probe, Gundestrup probe [89]. In ADITYA, we have used the simple Mach probe aligned along the direction of the toroidal magnetic field and $M = 0.43ln(\frac{J_{UP}}{J_{DN}})$, to estimate the flow Mach number.

[1]In the case when the area vector of the probe is along the magnetic field lines, the sheath formation is just like the magnetic field free case, but in case of an angle of area vector with the field, a region between the sheath and presheath is formed with the thickness of the order of ion larmor radius. It is the magnetic presheath. The particles are collected at the MPSE with the speed C_s and MPSE changes the direction of the ions, from along the field lines to the perpendicular to the probe surface.

Chapter 4

Plasma flows in Scrape-off Layer of ADITYA Tokamak

4.1 Introduction

Considering the importance of SOL flows to the main plasma, measurements have been carried out in several tokamaks [3, 4, 5, 12, 19, 20, 21, 22, 23, 24, 25]. The plasma flow is generally presented in the form of Mach number, the ratio of the flow velocity to the local ion sound speed. It is usually measured in the toroidal direction or along the magnetic field, in which case they are named the parallel flows. Measurements show that the flows have significant local variation in all three directions [3, 4, 5, 12, 19, 20, 21, 22, 23, 24, 25]. Since the magnitude and flow pattern depend on locations of particle sources and sinks, estimation of SOL plasma flows is important in every tokamak including ADITYA. In this chapter we report measurement of plasma flows in the SOL region of ADITYA tokamak [90]. We present the measured radial profile of toroidal Mach numbers at one toroidal/poloidal location and put forward reasonable explanation of the measurements.

Although magnetized Mach probe [85, 86, 87] is generally used in tokamak, there are plasma devices where it is not practical to use magnetized probe because they are operated at lower magnetic field and hence the required probe size may be large. When plasma flow is measured with un-magnetized Mach probe [82, 91, 92], its accuracy is questionable because the data interpretation is based on heuristic

model [83]. However, recent 3-dimensional PIC simulations have shown that special probe geometry is required for un-magnetized flow measurement [93, 94].

We carry out measurements of Mach numbers in the SOL plasma by using magnetized Mach probe. In this chapter we report following observations: (i) toroidal Mach number increases with distance in the SOL, and (ii) toroidal Mach number decreases with increasing local density. These results are explained in terms of combined drift driven and transport driven flows.

The rest of the chapter is organized as follows: Sec. II describes the experimental set up and results are presented in Sec. III. We then give estimation of expected ion flows for ADITYA plasma in Sec. IV, and summary of the chapter is presented in Sec. V.

4.2 Measurements and Analysis Procedure

The experiment is carried out with the toroidal magnetic field, $B_T = 0.2$ T. The ohmic and the equilibrium vertical fields are produced by two sets of capacitor banks.

The plasma parameters are as follows: plasma current ~ 25 kA [see Fig. 4.1], edge safety factor q(a) ~ 3.3, plasma duration ~ 25 ms, core electron temperature ~ 100 eV, central chord-averaged plasma density $5 \times 10^{18}\ m^{-3}$, SOL plasma density of $5 \times 10^{17}\ m^{-3}$ and the working gas is hydrogen. Measurements are carried out on different days by keeping plasma current and toroidal magnetic field constant and wall conditioning is done through glow discharge cleaning and pulse discharge cleaning before starting the experimental session on each day. The constancy of wall conditioning (i.e., impurity release during discharge) however cannot be maintained, which may result in large scatter in the data.

The Mach probe is mounted on the outboard side ($\theta = 0^o, \phi = 54^o$). Here we use limiter location for the toroidal reference angle (i.e. $\phi = 0^o$) that increases in the ion drift direction (clock-wise as seen from the top). Similarly the poloidal angle convention is such that its reference (i.e., $\theta = 0^o$) is on the outboard mid-plane

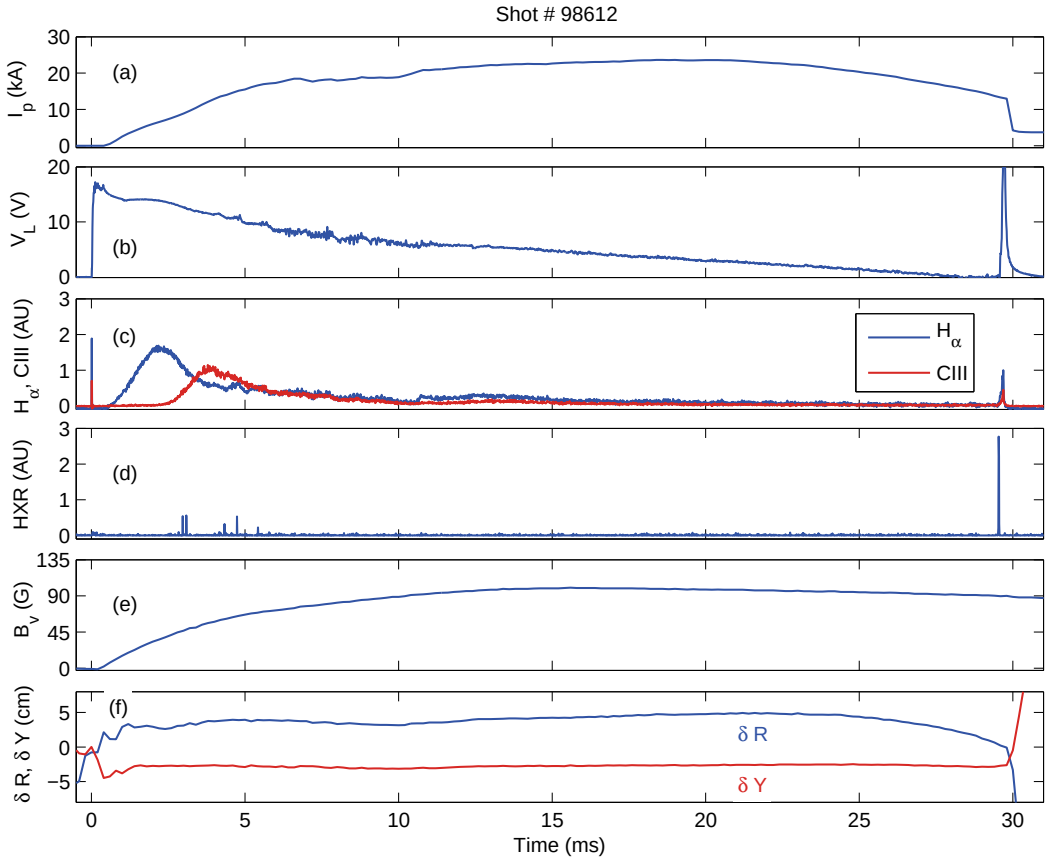

Figure 4.1: *Typical ADITYA capacitor bank discharge, (a) plasma current (I_p), (b) loop voltage (V_L), (c) H_α and CIII emission line radiations, (d) Hard X-ray signal (HXR), (e) vertical field B_v, and (f) horizontal (δR) and vertical (δY) shifts in the plasma column from the limiter center. The capacitor bank discharges are normally $\sim 25 - 30$ (ms) long. Both V_L and B_v are generated by the capacitor banks.*

and it increases above the mid plane. The same probe holder also accommodates another Mach probe that measures the poloidal direction of plasma flows from the ratio of upstream and downstream ion saturation currents.

Figure 4.2(a) shows a front view and a side view of the probe head. The head consists of an alumina ceramic holder on which two pairs of molybdenum plates of dimensions of $4\ mm \times 6\ mm$ are mounted with a toroidal and poloidal separations of 9 mm each [See Fig. 4.3]. Since the ion gyro-radius is $\sim$ 2 mm for the SOL

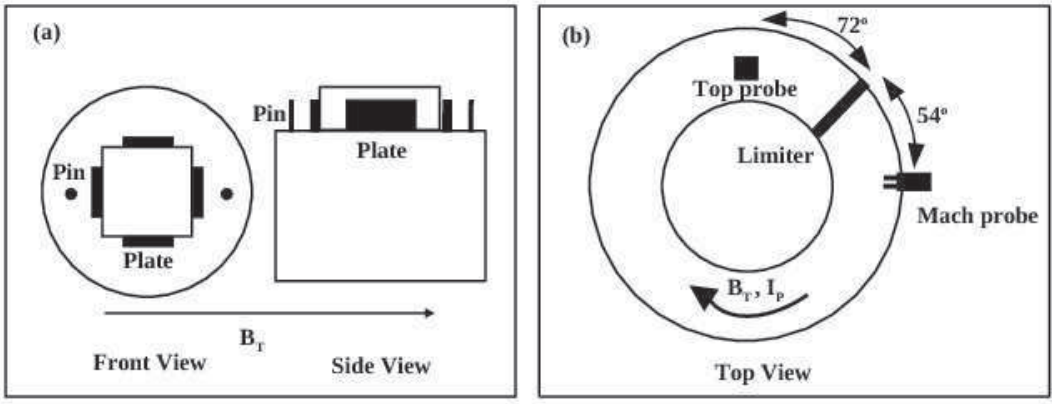

Figure 4.2: *(a) Front and side views of the Mach probe head (schematic), (b) top view of the ADITYA tokamak showing toroidal separation between the limiter and the Top and Radial probe head. The Top probe head consists of a single Langmuir probe and an unmagnetized Mach probe. All the measurements of Mach number are carried out in the ion saturation region. The direction of the B_T and I_p are indicated.*

plasma, the plates form a magnetized Mach probe. Similarly, two molybdenum wires of 1 mm diameter and 4 mm length each are also mounted on the same ceramic holder with a toroidal separation of 17 mm. However, as explained earlier, the pins cannot be used to determine the magnitude of plasma flows. Since probes are in pin-pate configuration and both are biased to $-100\ V$ in order to keep them in ion saturation regimes simultaneously, ion saturation current measurement at the plate is not affected by the presence of biased pins [95].

Since the Debye length of the SOL plasma is $\lambda_D \sim 35\mu m$, the value of the sheath thickness is few times λ_D and thus small compared to the 3 mm separation between the plate and the pin, that avoids sheath-sheath interaction [73]. Figure 4.2(b) shows the location of Mach probe with respect to the limiter and the upstream flow direction is defined as the one in which plasma flows to the ion side of the limiter. The probe collection length or, the shadow length is $C_s l^2/D_\perp$, where l is the probe length, $D_\perp$ is the cross-field diffusivity and C_s is the ion acoustic speed. Assuming C_s= 45 km/s for $T_e = T_i = 10eV$, l = 4 mm and $D_\perp$= 6 m^2/s (determined later), the estimated value of the shadow length is ∼0.12 m, where T_e and T_i are the electron and ion current respectively. Since this distance

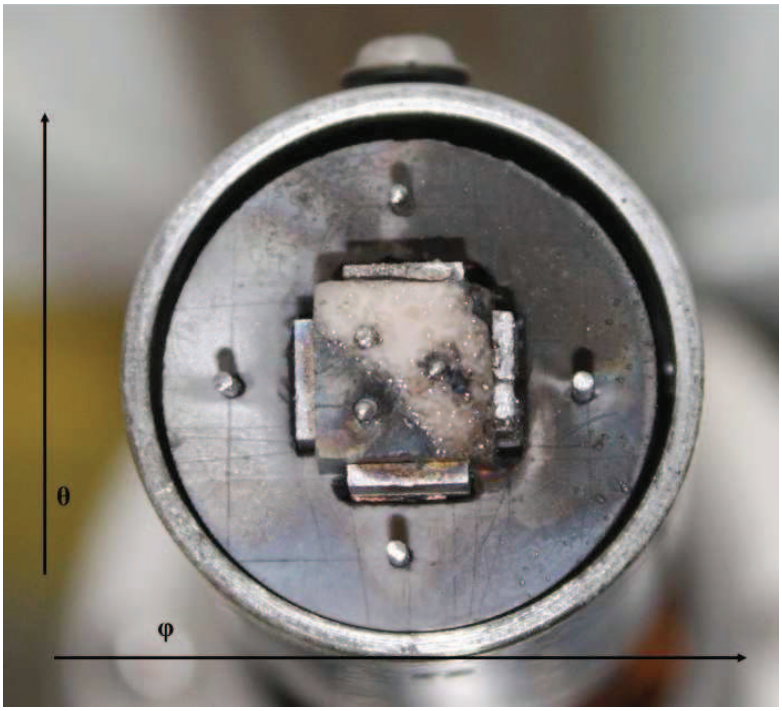

Figure 4.3: *Front view of the Mach probe head (Schematic shown in Fig.4.2). The toroidal/poloidal plates (6 mm × 4 mm) are separated by the 9 mm and the toroidal/poloidal pins (length=4 mm, diameter= 1 mm) are separated by the 17 mm. The toroidal plates, forms a magnetized Mach probe, and used for the parallel Mach number (M) measurement. The toroidal pins forms a unmagnetized Mach probe and used to check its flow direction consistency with the magnetized Mach probe. The poloidal plates are used to measure the poloidal flow direction only. The toroidal and poloidal directions are shown by ϕ and θ respectively. The three central point probes forming a triple Langmuir probe (forming equilateral triangle) and the poloidal separated pins are not used for this experiment.*

is smaller than the distance of the nearest face (electron side) of limiter, which is ∼1 m, the probe does not cast shadow on the limiter.

Another probe head comprising a single Langmuir probe (length=3 mm, diameter=1mm) and un-magnetized Mach probe of same dimension is located on the top port ($\phi = 288^o, \theta = 90^o$). As explained earlier, this Mach probe cannot be used to determine the magnitude of Mach number, it is used only to determine the toroidal flow direction (from saturation currents ratio). The single Langmuir

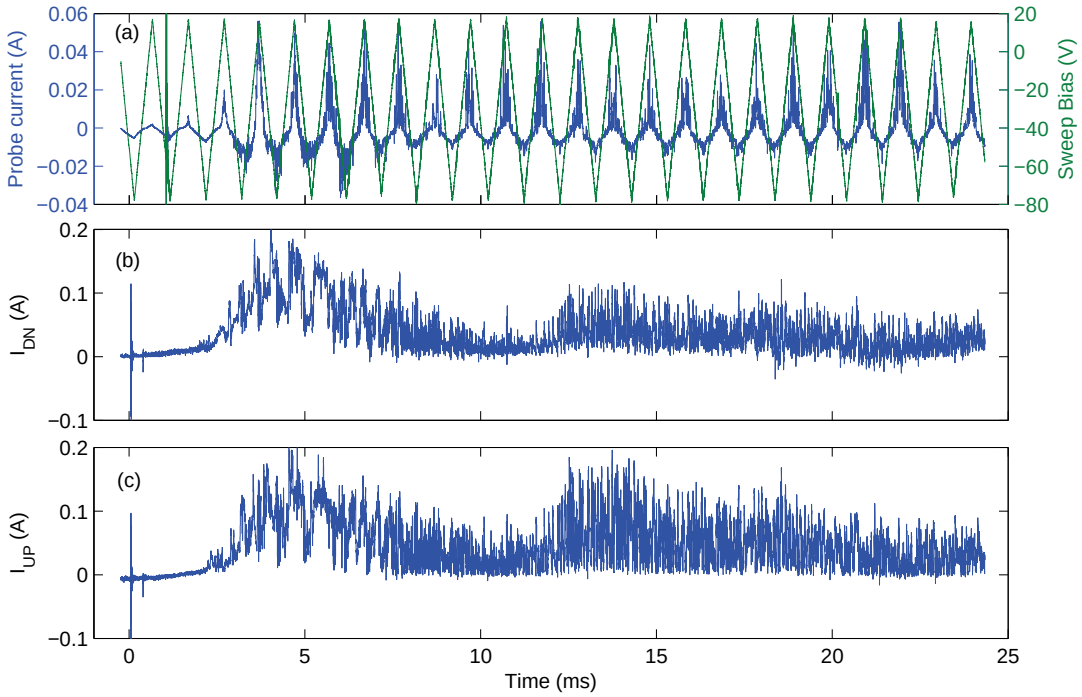

Figure 4.4: *Raw data, (a) sweep bias and corresponding Langmuir probe current, (b) downstream plate current I_{DN} of the Mach probe and (c) upstream plate current I_{UP} of the Mach probe. The Mach number and the electron current estimation are carried out in the window of* $10 - 20$ *ms, during the I_p flat-top.*

probe is used to measure electron temperature (T_e) by applying a sweep bias voltage (-80 V to + 20 V). The waveform had a triangular shape with the frequency of 1 kHz [see Fig. 4.4(a)]. Figure 4.5 shows I-V characteristics measured in the current flat-top duration that typically extends ~ 10 *ms*. At the sweep frequency of 1 kHz, the higher frequency fluctuation exists in the probe current and therefore we have averaged probe characteristics in 6 successive sweeps and smoothened the data by 50 μs moving average before presenting in Fig. 4.5.

We have limited the negative bias voltage to 5 times the floating potential in order to avoid nonsaturation of measured ion saturation current and arching at the probe [96]. Since the positive bias of the sweep does not draw electron saturation current, we assume that the probe does not perturb the plasma. Further, electron temperature is determined from the slope of I-V characteristics in the

neighborhood of the floating potential.

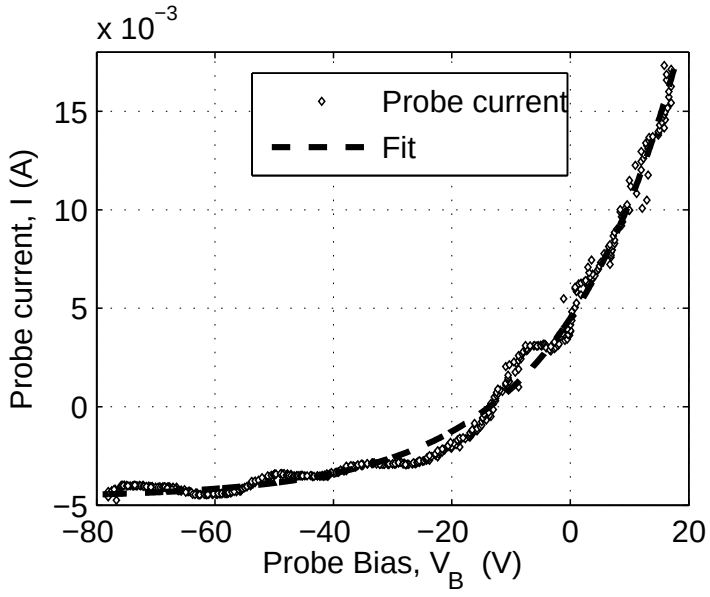

Figure 4.5: *The I-V characteristic of the unmagnetized probe for the probe biasing voltage from -80 V to 20 V. The fitted line indicates* $I = ae^{-bV_B} + c$ *, where a=0.812, b=-0.049 and c=-0.412 and the regression coefficient, R-square=0.99. It is the average of six successive sweeps.*

The electron temperature was determined from probe current in the flattop duration ($\sim$ 10 ms), by removing the ion saturation current and then by fitting an exponential curve in the neighborhood of the floating potential. The radial profile of electron temperature is shown in Fig. 4.6(a), which indicates T_e in the range of 7-15 eV over a distance of 35 mm in the SOL plasma. Here the radial distance refers to the distance between the probe center and the LCFS, which is determined from the plasma centroid position as measured by magnetic probes. These magnetic measurements give the co-ordinates $(\delta R, \delta Y)$ of the plasma centroid [see Fig. 4.1(f)]. The cross-section of the LCFS is a circle with a radius of $r_L - \sqrt{(\delta R)^2 + (\delta Y)^2}$, where r_L is the limiter radius [see Fig. 4.7]. This limited contact of plasma with the limiter in ADITYA allows the outboard SOL field lines to connect with the inboard SOL field lines. Since the probe head is mounted on a movable shaft, which can be moved to different radial locations with respect to

the limiter, the probe-LCFS distance can be determined by combining it with the centroid position. The latter is however not under feedback control and varies from shot-to-shot as per the plasma equilibrium. The variation of equilibrium position is typically within ±5 mm, which is responsible for changes the probe-LCFS distances.

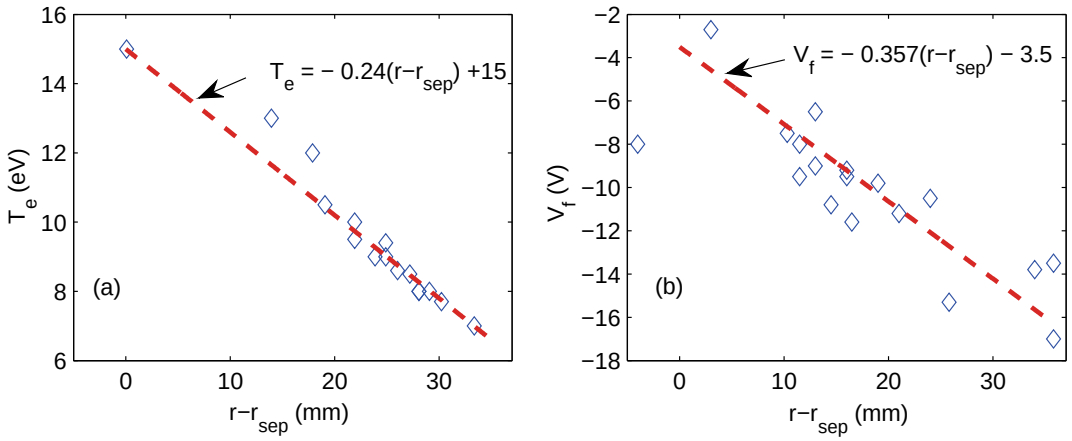

Figure 4.6: *(a) Radial profile of electron temperature measured by a Langmuir probe mounted on the top port in discharges similar to the presented ones; (b) Floating potential profile in identical discharges. The red dashed lines are the fitted lines to the corresponding data points.*

Does the presence of limiter near the probe location affect the plasma flow? Since it is well known that there is toroidal variation in the plasma flow in limiter tokamaks [18], we would like to answer whether the presence of neutral source near the limiter affects the measurement. For this purpose, we have estimated that the probe location is ∼1 m from the nearest (electron) face of the limiter. This distance is small compared to the ion-neutral mean free path, $\lambda_{in} \cong 2$ m for a neutral density of 10^{19} m^{-3} near the limiter. We therefore conclude that the presence of neutral source near the limiter does not affect the flow measurement.

The radial profile of the floating potential is shown in Fig. 4.6(b) and it may be used to determine the radial electric field or the associated drift velocities as discussed in Sec. IV. It should be noted here that the floating potential at the 'Top

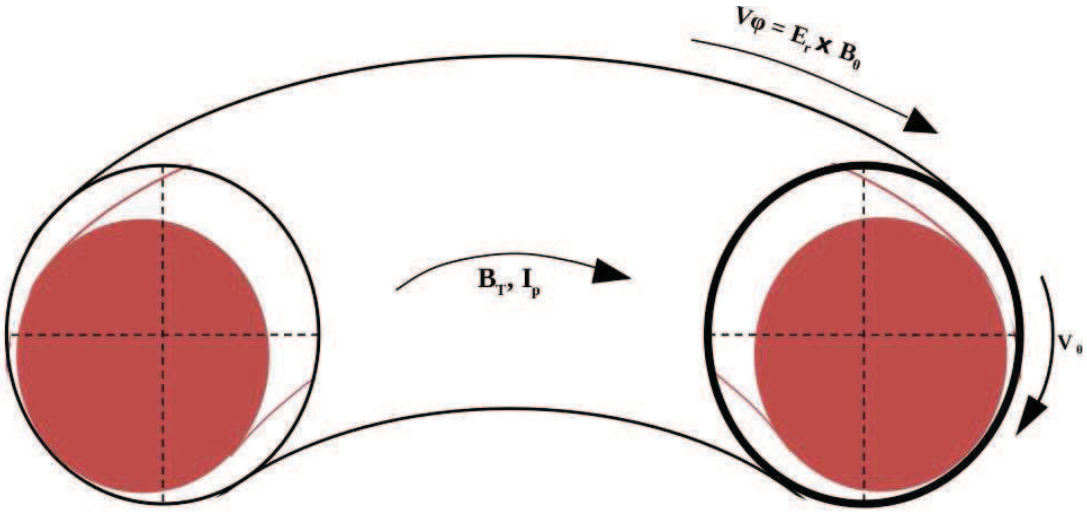

Figure 4.7: *Schematic diagram showing plasma position (exaggerated). The probe positions (on both radial and top ports) are fixed with respect to the limiter, but plasma positions in different discharges may be different. The limiter center is indicated by the two dashed lines. Position probes are used to estimate the horizontal and vertical shift of the plasma column centroid from the limiter center. The* $V_\phi = E_r \times B_\theta$, V_θ, B_T *and* I_p *directions are indicated.*

probe' location is negative, which indicates that the curvature and magnetic field gradient causes electrons to drift upwards [97].

Mach number is determined from the measured ratio $R = J_{UP}/J_{DN}$, where the numerator is the ion saturation current density in the upstream direction and the denominator is that in the downstream direction [see Fig. 4.8]. The Mach number is determined by using the Hutchinson's formula, $M = 0.43ln(R)$, which is independent of the ratio of ion and electron temperatures [30].

4.3 Experimental Results and Discussion

We have determined mean plasma density n_{eb}^{Mean} from Mach probe by using the formula: $0.35en_{eb}^{Mean}C_s = \sqrt{J_{UP} \times J_{DN}}$ [86] and, the plasma density from single Langmuir probe is determined from the relation: $J_s = 0.5en_{eb}C_s$ and making thin sheath approximation [73].

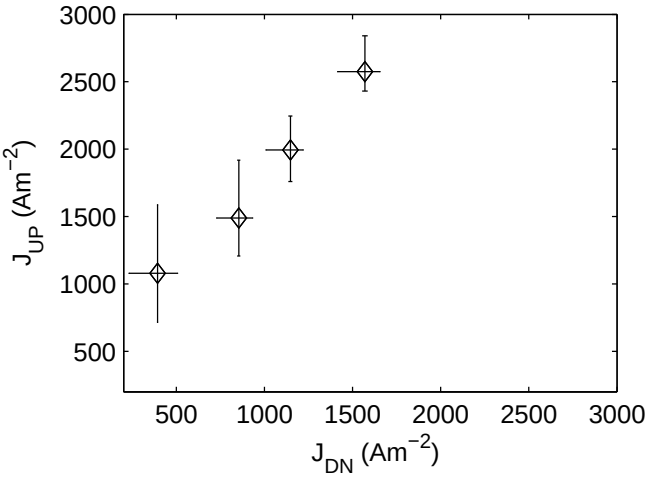

Figure 4.8: *Comparison of the upstream J_{UP} and downstream J_{DN} current densities, measured by the Mach probe plates. The Mach number is estimated by the asymmetry in the J_{UP} and J_{DN}.*

4.3.1 Radial Profiles of Mean Density at the Top and Radial Ports

We have measured plasma density at the radial port by using the Mach probe and that at the top port by using a single Langmuir probe. Results show that the density scale length λ_n (i.e., 1/e decay length) at the top port is typically 3 times of that at the radial port [see Fig. 4.9]. Similarly, the magnitude of the plasma density at the top port is 4-5 times smaller than that on the radial port. The poloidal asymmetry in density is in agreement with similar measurement on DITE tokamak reported by Pitts *et al.* [29]. From simple SOL model $\lambda_n = (D_\perp L_\parallel / C_s)^{1/2}$, where $L_\parallel$ is the connection length and the estimated value of the $L_\parallel$ at the top port is a $\pi Rq \sim 8$ m, and that at the radial port, ~ 1 m. By assuming same C_s at both locations, we obtain $D_\perp \sim 6\ m^2/s$ at both locations. This is comparable to the value obtained from direct measurement [90]. It should be noted that similar equilibrium configuration may be expected in other tokamaks, where active feedback control is not used. The density profile along with temperature profile can be used to determine plasma pressure gradient, while looking for an explanation of measured plasma flows in sec. IV.

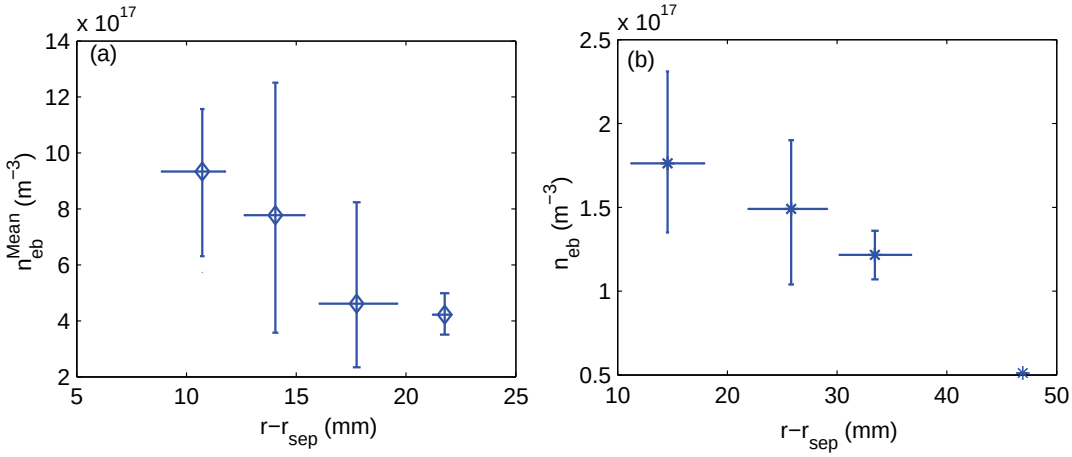

Figure 4.9: *(a) Radial profile of mean plasma densities measured by the Mach probe at radial port, and (b) Radial profile of plasma density measured by the single Langmuir probe at the top port. The error bars indicate the scatter in the data. The difference in the magnitude and the decay lengths can be seen from the figure.*

4.3.2 Radial Profile of Mach Number and its Dependence on Mean Density

We have also measured the radial profile of toroidal Mach number in the SOL plasma [see Fig. 4.10(a)]. It is observed that toroidal Mach number increases with distance from the LCFS. This trend has been seen in several tokamaks, where the Mach number initially increases and then starts decreasing [3, 4, 5, 20, 22, 33, 35] around $\sim$ 20 mm away from the LCFS. The measured toroidal Mach number as a function of the mean density is plotted in Fig. 4.10(b). It is observed that the Mach numbers decrease with increasing density. This observation is also in agreement with measurements from other tokamaks, where Mach number decreases with increasing chord-averaged density [4, 12, 13]. Since the increase in chord-averaged density may also result in increase in the SOL plasma density, it may be concluded that the trend is similar with SOL density. The decrease in plasma flows with increase in plasma density may possibly indicate a role of electron temperature/electric field in the driving mechanism.

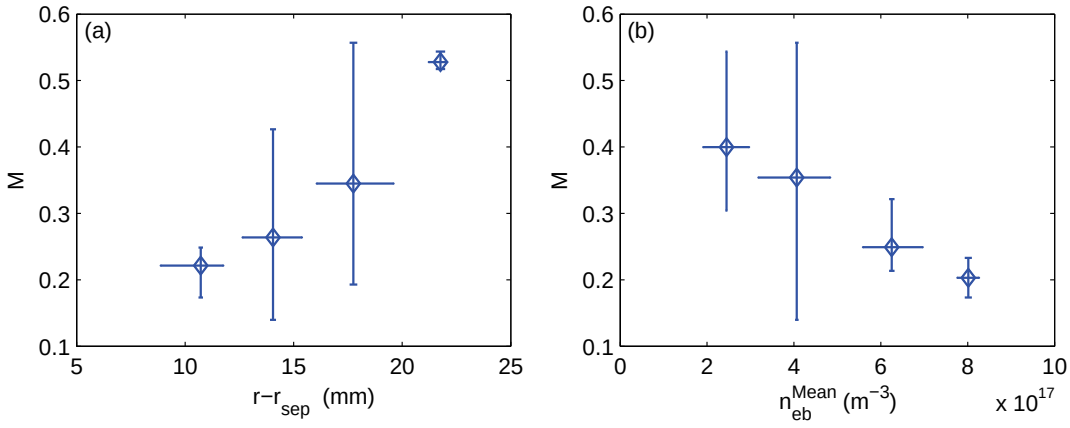

Figure 4.10: *(a) Radial profile of the Mach numbers, and (b) Dependence of Mach numbers on the mean plasma density. The error bars indicate scatter in the data.*

4.4 Possible Flow Mechanism and Flow Estimation

It is important to understand the role of the location of plasma contact with the limiter in deciding the flow direction. For this purpose, we have determined the direction of poloidal flow by using another Mach probe in the same probe head [see Fig. 4.3]. It should be noted that the present probe configuration cannot be used to determine the magnitude of poloidal flow Mach number [89], but the flow direction, which depends on the probe current ratio, can safely be concluded. We observe that the poloidal flow is towards the contact location.

How do we explain the magnitude and direction of the measured toroidal flow? It is well known that in the SOL plasma the measured flow can have several components, namely, the $E \times B$ flow, the ion Pfrisch-Schluter flow, the ballooning transport and the ion flow caused by thermal pressure gradient along the field line due to particle sources and sinks [4, 5, 23]. Since it is difficult to include all above-mentioned factors in a model, we present quantitative estimates of each one separately.

4.4.1 $E \times B$ Flow

We have presented in Fig. 4.6(b) the radial profile of floating potential in the SOL plasma. The measured floating potential is negative and it increases from -18 V in the far SOL to -2 V in the near SOL, i.e., over a distance of ~ 35 mm. We can use the measured electron temperature profile, presented in Fig. 4.6(a), and determine the plasma potential V_p by using the relation, $V_p = V_f + 3.5T_e$. The estimated value of radial electric field in the SOL plasma is ~ 1 kV/m, which is directed outward and constant in the SOL. For ADITYA discharges, the poloidal magnetic field B_θ at the limiter is 0.02 T. The toroidal flow velocity can be calculated from radial component of the force balance equation:

$$V_{\phi e} = \frac{E_{rm}}{B_\theta} - \frac{1}{en_{eb}B_\theta}\frac{\Delta p}{\Delta r} + V_{\theta e}\frac{B_\phi}{B_\theta} \tag{4.1}$$

where, E_{rm} denotes the measured radial electric field, $V_{\phi e}$ and $V_{\theta e}$ are estimated quantities, and Δp is the plasma pressure difference over the distance of Δr. Assuming SOL plasma density $n_{eb} = 5{\times}10^{17}\ m^{-3}$, and both electron and ion temperatures of 10 eV, the SOL plasma pressure can be written as $p = (3/2)n_{eb}k_B(T_{eb}{+}T_{ib})$ and the pressure gradient $\Delta p/\Delta r$ is estimated to be $\sim 120\ Jm^{-4}$. By assuming $E_{rm} \sim 1\ kV/m$, $V_{\theta e} \sim 0.1C_s \sim 4.5\ km/s$, Eq. (1) gives $V_{\phi e} \sim 20\ km/s$ which is $\sim 0.4C_s$. It should be noted that the friction/damping term in the force balance equation is ignored in Eq. (1).

4.4.2 Ion Pfrisch Schluter Flow

The curvature drift in tokamak geometry causes vertical charging. For our experimental conditions, electrons accumulate on the top side and ions on the bottom side. This vertical charging can get shorted either by Pfrisch-Schluter (PS) flow of ions [see Fig. 4.11]. The PS flow velocity is given by $V_{PS} = 2q_sV_\perp cos\theta$ where, $V_\perp = E_r/B_\phi - \Delta_r p/en_iB_\phi$, $\Delta_r p$ is the radial gradient of plasma pressure and θ is the poloidal angle. The direction of PS flow on the outboard side is in the direction of the measured toroidal flow. This mechanism may be important in our case since ADITYA equilibrium allows connection between the top and bottom sides even inside the scrape-off layer [see Fig. 4.7]. The estimated value of the PS flow velocity is $\sim C_s$. It is therefore obvious that PS flow alone cannot be the operating

mechanism and, there should be another mechanism opposing the PS flow velocity.

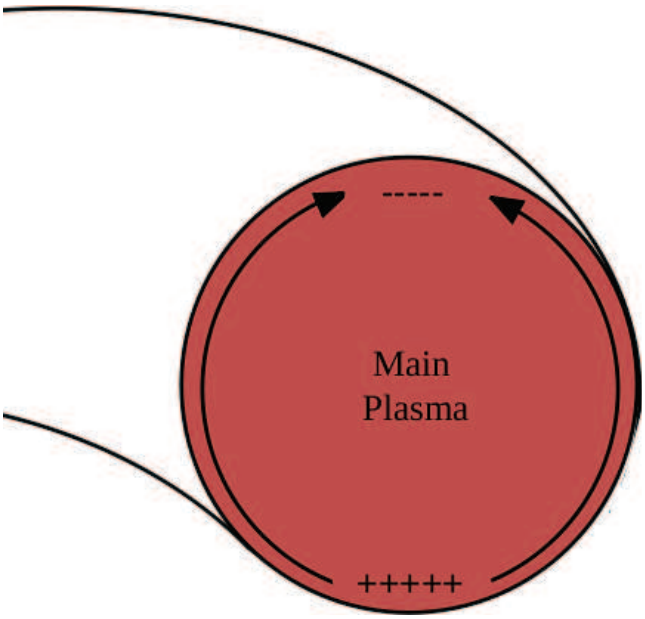

Figure 4.11: *Sorting of the vertical charging by the Pfrisch Schluter (PS) flows. The direction of the PS flows in the outboard side is in the I_p direction and opposite to it in the inboard side. The circle indicates the LCFS and two lines with arrow shows the direction of the PS flows from bottom to top of the plasma column.*

4.4.3 Ballooning Transport

The ballooning nature of cross-field transport [see Fig. 4.12] may be important mechanism of plasma flows in single null (SN) divertor tokamak, where low-field side (LFS) is magnetically connected to the high-field side (HFS) [12, 25]. The plasma equilibrium, in ADITYA tokamak, is such that it can be compared with SN divertor configuration, except that the separatrix is the wet area, which is in contact with the limiter. The field line, even in the scrape-off layer plasma, connects the LFS with the HFS [see Fig. 4.7]. As our probe position is near to the mid point of the LFS plasma, so the contribution of flows due to the ballooning transport is negligible [12].

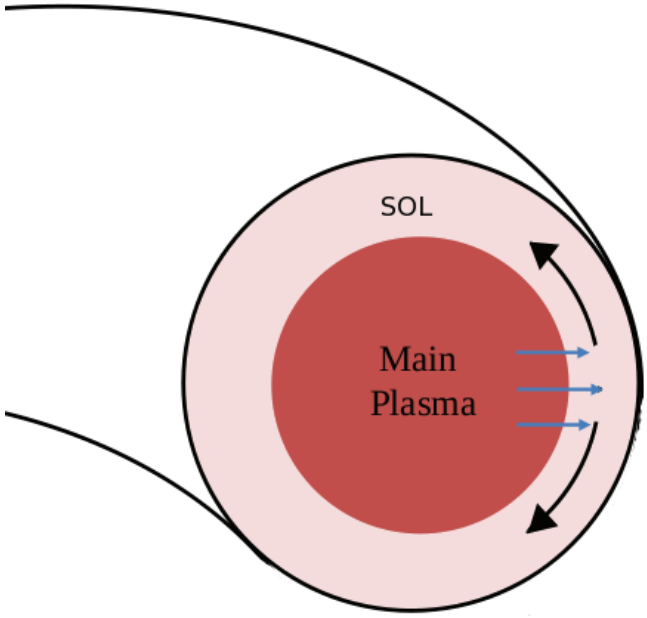

Figure 4.12: *Ballooning transport cartoon. The preferential diffusion of the particles on the outboard side is named as the ballooning type transport. It is because of the bad curvature of the B_T on the outboard side. The blue horizontal arrows shows the plasma diffusion and the the black arrows shows the plasma flow direction.*

4.4.4 Sink Action of the Plasma Contact with the Limiter

Ions and electrons are lost from the main plasma by cross-field diffusion before they enter the SOL plasma. They get collected on two sides of the limiter surface through parallel diffusion, and traverse an average distance of $\pi R q_a$ before being collected at the limiter surface. In a simple 1D SOL model for sink action of limiter [17], it can be shown that $P_e + P_i + mnv_a^2 = constant$, where P_e and P_i are electron and ion thermal pressures and v_a is the ambipolar flow velocity of ions on a field line. Since the ambipolar flow velocity is zero at the stagnation point, the thermal pressure attains its maximum value ($P_0 = P_e + P_i$) at that point. By using the Bohm condition on plasma density, the thermal pressure at the sheath edge is $P_0/2$. Since plasma thermal pressure decreases with radial distance, the values of the constant must also decrease with the radial distance (at the stagnation point) [see Fig. 4.13].

The sink action of the limiter produces plasma flow in the counter clockwise di-

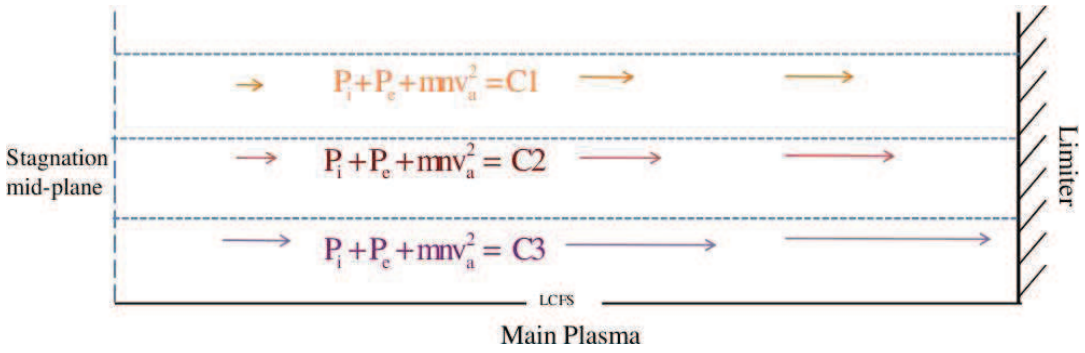

Figure 4.13: *The variation of the plasma pressure along and across the field lines in the SOL plasma. Here C1, C2 and C3 are the constants and C3 > C2 > C1. At the mid-plane, between the two faces of the limiter the flow speed ($v_\parallel$) is nearly zero and it increases towards the limiter face. The speed is shown by the arrows. The increase in the speed ($mnv_\parallel^2$) is to keep the plasma pressure constant on the field line as the static pressure $P_e + P_i$ at the limiter is nearly zero. The plasma pressure decrease as we go away from the the LCFS, so the retardation to the measured flows with $r - r_{sep}$.*

rection, which is in electron side of the limiter and opposes the measured flow. This opposition decreases with the increasing distance from the LCFS and hence explains the increasing trend of Mach numbers with radial distance.

Figure 4.14 shows the slab view of ADITYA SOL plasma along with flows generated by different mechanisms including the sink action of the limiter (Grad p flow). The directions of flow generated by different mechanisms indicate that $E \times B$ and PS flows add to give the flow in the measured clockwise direction, and flows caused by sink action of the limiter are in the opposite direction and most likely explains the measured radial profile of the Mach number. However it is not possible to estimate its contribution on the measured Mach number and separate experiment is required to determine it.

4.5 Summary

We have presented measurements of SOL plasma flows in the ADITYA tokamak by using Mach probe on a movable shaft. Radial density profiles at the top port and the radial port indicate that gradient scale length at the top port is larger

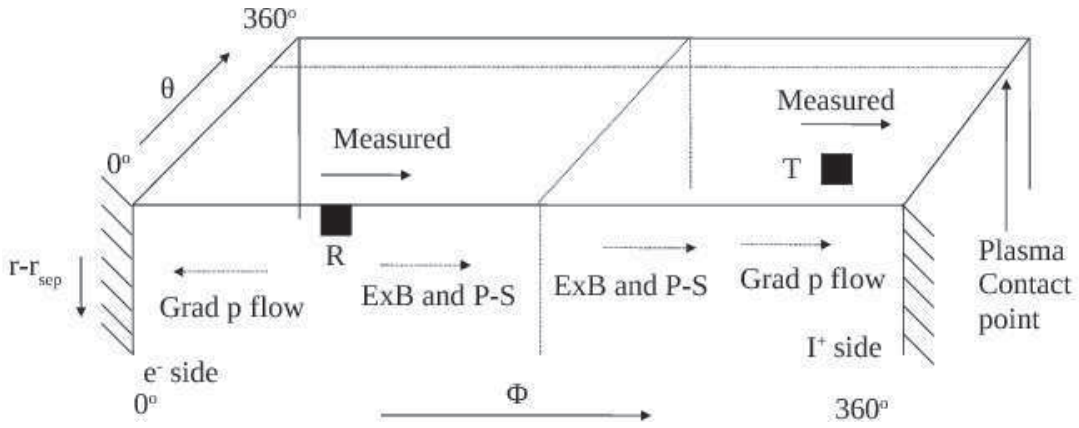

Figure 4.14: *Schematic diagram of ADITYA SOL flows. 'R' and 'T' indicate physical locations of Mach probe on the radial and top ports respectively and 'Measured' indicates the measured flow direction. The hatched lines indicate two faces of the limiter and 'Plasma contact point' indicates the contact of the plasma LCFS with the limiter [see Fig. 4.7]. Note that the connection length at the top probe is $\pi R q_a$ as explained in the text.*

than that at the radial port. This can be explained in terms of larger connection length at the top port compared to that at the radial port. This peculiar situation arises because of shifted plasma column in torus.

We have further reported parametric dependence of Mach numbers. Our observations confirm reports from other tokamaks, and they add to the existing database. For example, we observe that Mach number increases with the radial distance from the LCFS. Similar observations have been reported from many tokamaks and interpreted in terms of sink action of the limiter. Likewise our observation that flow Mach number decreases with the increase in the average local plasma density is similar to observation from other tokamaks.

We have considered mechanisms that may be responsible for the observed flow. It is determined that $E \times B$ drift and PS flows of ions have significant contributions to the measured Mach number, sink action of the limiter opposes the two, and flow due to ballooning transport is insignificant at the outer mid-plane(radial) probe. It may be necessary to carry out further experiment by reversing the toroidal magnetic field and plasma current in order the separate the transport driven flow from

the drift driven flow.

We have also determined that the toroidal flow direction is towards the ion side of the limiter and the poloidal flow direction is towards the contact of the LCFS with the limiter.

Chapter 5

Scrape-off Layer Plasma Flow Modification with Gas Puff

5.1 Introduction

Since scrape-off-layer (SOL) plasma is the interface between main plasma and the material wall, most of the plasma wall interaction takes place in this region. The plasma wall interaction can create impurities, mainly by sputtering of plasma facing components [49]. However SOL plasma parameters, like density, temperature, radial electric field and plasma flows are quantities that determine the levels of sputtering and hence levels of impurities. If these impurities are not removed, they can enter into the core plasma and dilute it [18]. The parallel plasma flows, in particular, play important role in determining the location of the sink of plasma particles as well as impurities, where efficient means of particle exhaust can be deployed. The efficiency of particle exhaust can then determine the impurity content in the main plasma [19]. In recent years a significant progress has been made in understanding the SOL flows keeping in mind its role in impurity removal and in L/H transition [25]. However, there are several other methods, namely, pallet injection, electrode biasing and gas puff (GP) for modifying the plasma edge and confinement improvement in addition to the traditional methods of confinement improvement by H-mode operation [98].

We have used a controlled puff of working gas for modifying SOL plasma pa-

rameters. The GP may increase the local ionization source, affect SOL plasma parameters and hence plasma flows along the magnetic field [3, 99, 100]. The GP may also increase the plasma-impurity friction force [101] which, in turn, may decrease the Z_{eff} [27]. The GP may also alter the radial electric field profile as well as the plasma pressure at the GP location, which may results in the change in the SOL plasma flow pattern. Measurements in a number of tokamaks have shown that the location of GP plays an important role in the modification of SOL plasma parameters and flows [19, 100, 102, 103, 104, 105]. Similarly, the GP may cause the fluctuation suppression, which is accompanied by a flattening of the radial profiles of the floating potential, plasma density and Reynolds stress[90].

The SOL plasma flows can be derived by the neoclassical effects, which includes drifts and pressure gradient along the field lines [15]. However, these neoclassical effects may not be sufficient to explain the measured plasma flows and hence other effects need to be considered. Recently the link between turbulence and plasma flows has been identified as a possible mechanism to explain the SOL flows [42, 43, 44, 46]. In turbulence driven flows, the energy can interchange between mean flows and the turbulence [42, 43]. Turbulence can act as source as well as sink for the mean plasma flows.

In this chapter, we have reported effect of GP on particle flux, Mach number and electron temperature in the SOL region of ADITYA tokamak [48]. The radial particle flux is found to be maximum when the Mach number is nearly zero. We observe that electron temperature reduces to nearly half during the GP. The parallel Mach numbers are also measured at three discrete poloidal angles in order to construct the flow pattern. The Mach number shows change of flow direction from ion side to the electron side of the limiter only on the outboard mid-plane. At other locations the flow direction remains the same, but the magnitude increases. We further observe that there exists gradient in the electrostatic Reynolds stress near the limiter edge and it flattens during the GP.

The rest of the chapter is organized as follows: Sec. II describes the experimental setup and diagnostics and various experimental results are presented in Sec. III. The Summary is presented in Sec. IV.

5.2 Experimental Setup

The ADITYA discharge parameters for this experiment are as follows: toroidal magnetic field on the axis $B_T = 0.75$ T, plasma current ~ 80 kA, plasma duration$\sim$ 80 ms, core electron temperature $T_{eo} \sim 300$ eV, central cord-averaged plasma density $(1-2) \times 10^{19}\ m^{-3}$, edge safety factor $q_a \sim 3.5$ and SOL plasma density $n_{eb} \sim 1 \times 10^{18}\ m^{-3}$.

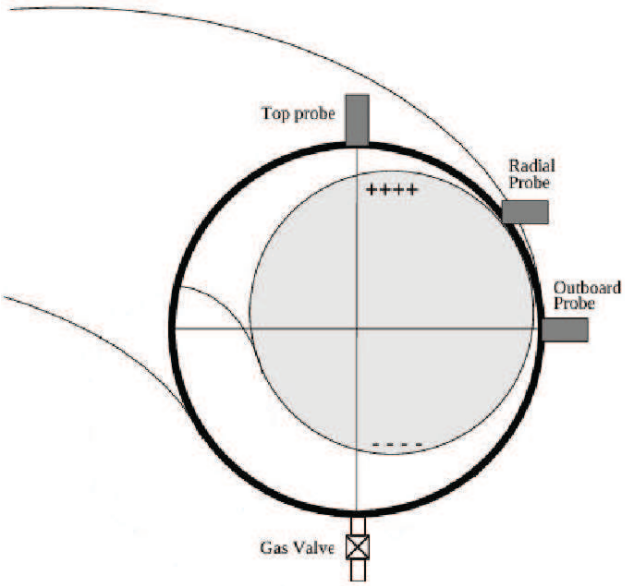

Figure 5.1: *Projections of probe heads and the gas puff valve on one poloidal/azimuthal plane. The limiter is shown by a thick circle. The vertical charging shows that the $B \times \nabla B$ is pointing to the top side of the plasma (B_T, anticlockwise from top of the machine). The plasma column is shifted in the outboard side and to the top side from the limiter center [see Fig. 5.2, for the measured δR and δY shift].*

.

Above parameters are obtained with ADITYA pulse power supply (APPS), which consist of the toroidal field power supply (50 kA, 400 V), the ohmic field power supply ($\pm$20 kA, 2 kV) and the vertical field power supply (12.5 kA, 2 kV)

by using a converters and wave shaping power electronics. The B_T is kept in anti-clockwise as seen from the top of the torus such that $B \times \nabla B$ is pointing towards the top side. The direction of plasma current I_p is clockwise and the centroid of the current channel or contact point of the LCFS with the limiter is in the 1^{st} quadrant on the low field side [see Fig. 5.1]. The measured horizontal and vertical shift of a typical plasma shot w.r.t. the limiter center are shown in the figure 5.2. All measurements are carried out in discharges with same applied B_T, and similar I_p.

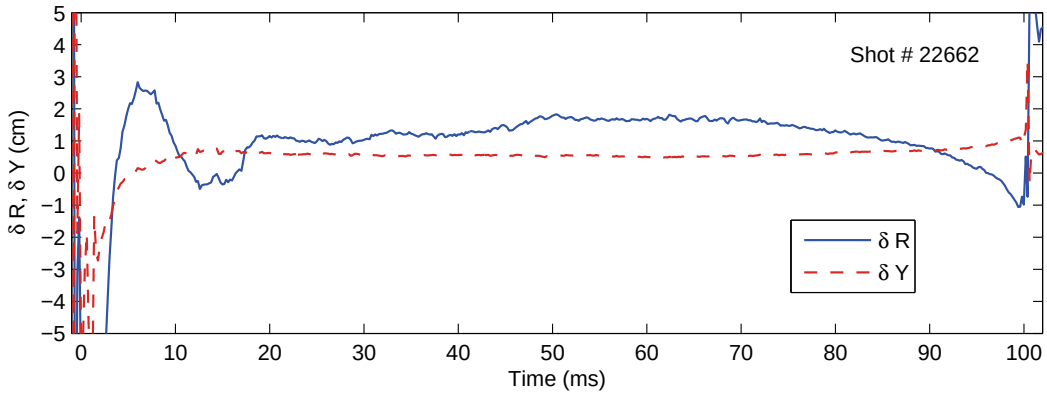

Figure 5.2: *Plasma column position measurement with respect to the limiter center. The δR and δY are the horizontal and vertical shift of the plasma column from the limiter center, respectively. The positive values of both δR and δY show, outboard and top side shift of the plasma column centroid [see Fig. 5.1, for plasma shift schematic].*

.

Measurements are carried out during the flat-top of the plasma current and the flat-top duration is $\sim$ 30 ms. This ensures that plasma is in equilibrium with constant plasma current and vertical field. There is no check on plasma density and electron temperature. The shot-to-shot variation in impurity conditions may also be present. Measurements of the SOL plasma parameters are carried out by using a probe configuration as shown in Fig. 5.3 (a). The probe head is specially designed for simultaneous measurements of plasma parallel flow Mach number, particle flux, poloidal electric field, electron temperature and radial electric field. The results presented in this chapter are obtained from a number of similar hy-

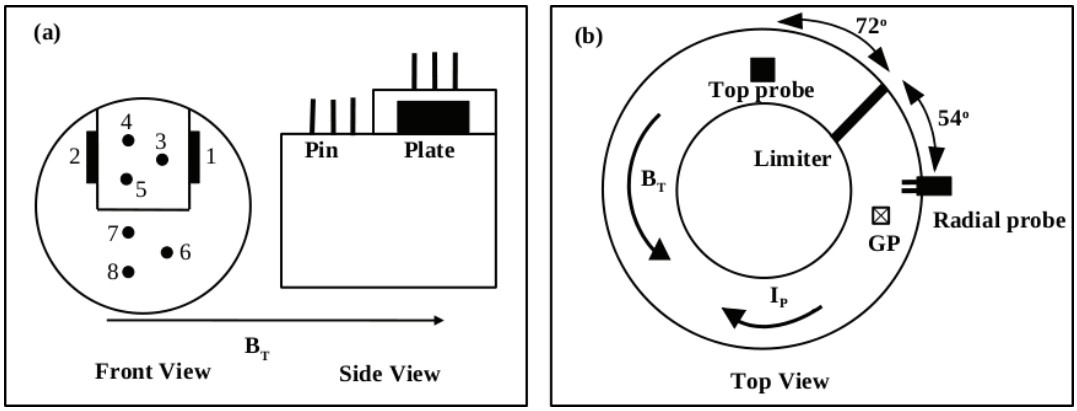

Figure 5.3: *(a) Schematic diagram of the probe head configuration, including pin probes and plate probes that are used for Mach number measurement. Probes 1,2 and 3 are used for ion saturation current and 4,5 and 7 are used for floating potential measurements. (b) locations of the Top probe, the Radial probe and the gas puff valve with respect to the limiter. Directions of plasma current and toroidal magnetic field are also indicated.*

drogen discharges that are taken on different days.

The probe head consists of an alumina ceramic holder on which one Mach probe consisting of a pair of molybdenum plates of dimensions of 3 $mm \times 4$ mm is mounted and toroidally separated by 9 mm [see Fig, 5.4]. The same probe holder supports a pair of triple probe, separated radially by 5 mm. The triple probe consists of molybdenum pins of 1 mm diameter and 3 mm length. The pins are on the vertices of an equilateral triangle of side 3 mm. Since the Debye length of the SOL plasma is ~ 25 μm, 3 mm separation is good enough to avoid overlapping of sheaths.

Probe heads are mounted on movable shafts, one at the radial port ($\phi = 54^o$, $\theta = 45^o$) and another at top port ($\phi = 288^o$, $\theta = 90^o$). Here, we use limiter location for the toroidal reference angle (*i.e.* $\phi = 0^o$) that increases in the ion drift direction (clock-wise as seen from the top), and outboard mid-plane for the poloidal reference angle (*i.e.*, $\theta = 0^o$) that increases above the mid plane. Figure 5.3(b) shows the location of probe heads with respect to the limiter. Another probe-head with only Mach probe plates of 6 mm width and 4 mm height is mounted on the LFS

mid-plane ($\phi = 54^o,\ \theta = 0^o$) so that flow pattern may be constructed.

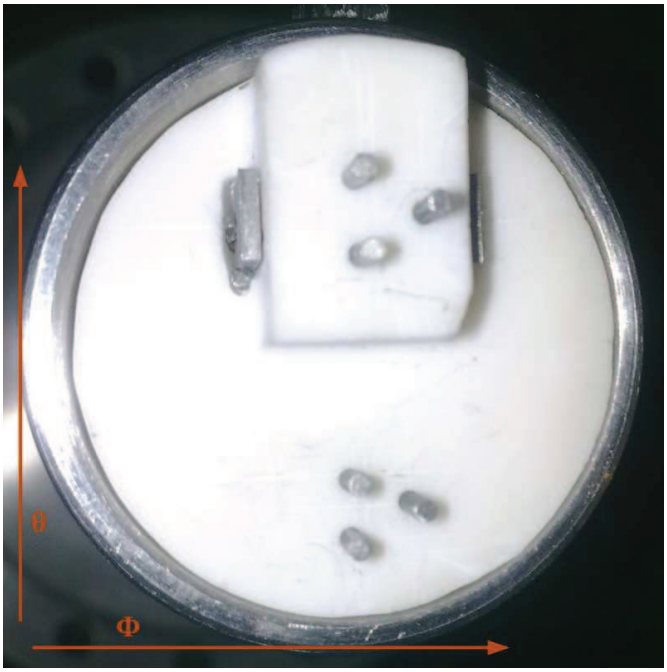

Figure 5.4: *Probe head, where the two Molybdenum plates separated by 9 mm and are 3 mm × 4 mm, and forming a magnetized Mach probe. The two triple probe separated by 5 mm radially are consists of 3 mm length and 1 mm diameter Molybdenum pins. The triple probe pins forms a equilateral triangle with a separation of 3 mm. The upper triple probe is used for the electron temperature and particle flux measurement.*

A piezo-electric valve at the bottom port ($\theta = 270^o, \phi = 90^o$) is used for controlled GP. The amount of injected gas is controlled by varying the valve opening time in the range of 0.5-1.5 ms so that plasma current and its equilibrium position remain unchanged. The valve opening duration is fixed at ~ 1 ms, which is equivalent to adding $\sim 1 \times 10^{18}$ hydrogen molecules. Figure 5.5 shows examples of signals from a particular ADITYA discharge. It should be noted that there is reduction in fluctuation amplitudes and increase in radiation of plasma edge. In addition, the GP causes significant increase in plasma density when the base line density is low [see Fig. 5.5(a)]. However, the density increase is not significant, when reduction in fluctuation amplitude is measured [see Fig 5.5(a) and Fig. 5.5(f)].

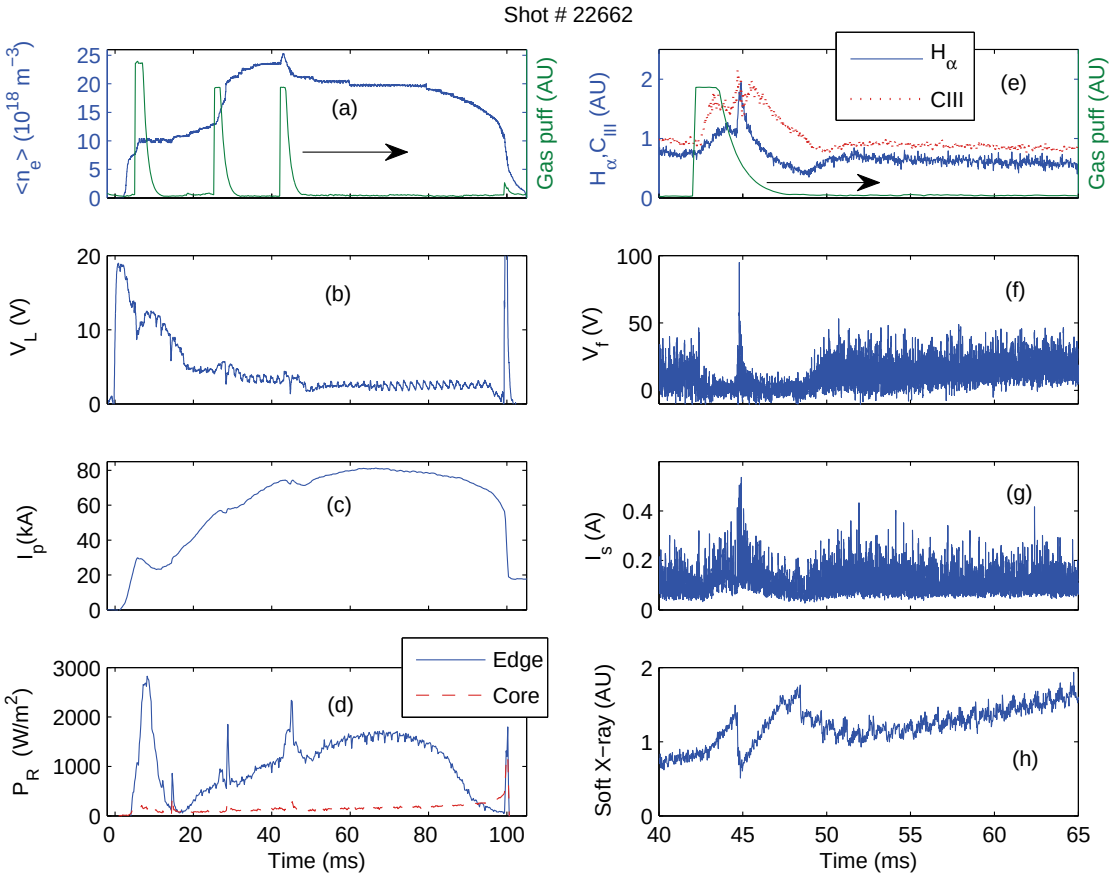

Figure 5.5: *Examples of typical ADITYA discharge: (a) Chord-averaged plasma density measured by μW interferometer and voltage pulses on the gas-puff valve, (b) loop voltage, (c) plasma current, (d) radiated power along edge and core chords as measured by AXUV bolometer camera, (e) shows H_α, C-III and voltage on the gas-puff valve during 40-65 ms into the discharge, (f) floating potential, (g) ion saturation current at probe pins (see 5.3) and (h) soft X-ray signal. The sharp dip in soft X-ray signal is may be ignored as pick up and hence the soft X-ray signal increases during the gas puff.*

5.3 Results and Discussions

The radial profiles of plasma density, measured at both top and radial probes are shown in Fig. 5.6. The radial profiles of the floating potential and the mean poloidal flow velocity, $V_\theta = (E_r \times B_T)/B_T$, near the plasma boundary are shown

in Fig. (5.7). All measured quantities are determined by averaging the data before/without and during GP. For the measurements carried out at the top port, the field line has long connection length, $L_\parallel \sim \pi R q_a \sim 8$ m in the SOL plasma, which is shown by the shadow region in Fig. (5.6) and subsequent figures. The 'zero' of r-r_{sep} represent the LCFS location. The field line has short connection length ($\sim$ 1 m) in the limiter shadow, indicated by 'Short $L_\parallel$' in the figures. On the other hand the field lines at the radial probes has only short $L_\parallel$. The density gradient scale length may be related to the connection length, and it may be shorter for short $L_\parallel$ [see Fig. 5.6(a,b)] [32].

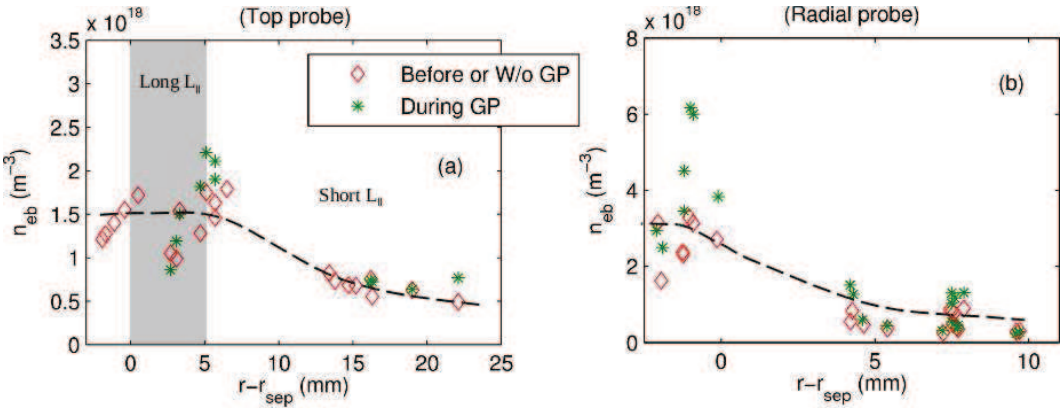

Figure 5.6: *Radial profiles of edge plasma density, measured at the (a) top probe and (b) radial probe. The vertical shadow band indicates the separation of the long $L_\parallel$ region from the short $L_\parallel$ region. Dashed lines are eye fits.*

The radial and parallel particle balance gives the following relation: $L_\parallel/C_s = \lambda_n^2/D_\perp$, and it can be used to determine the relation among the connection length, $L_\parallel$, the ion sound velocity, C_s, the density scale length, λ_n and the perpendicular diffusivity, $D_\perp$. It indicates that larger $L_\parallel$ gives larger λ_n, provided other quantities remain unchanged. This could be the reason behind very large λ_n in long $L_\parallel$ region and small $\lambda_n \sim 15$ mm in short $L_\parallel$ region [see Fig. 5.6(a,b)]. We can estimate the value of λ_n in the long $L_\parallel$ region by assuming, $L_\parallel \sim 8$ m, $D_\perp \sim 5$ m^{2}s^{-1} and $C_s \sim$ 45 km/s. The estimated value of λ_n is 42 mm which is approximately 3 times that of λ_n in short $L_\parallel$ region. We can also estimate the parallel transport time ($\frac{L_\parallel}{C_s}$), as well as the radial transport time ($\frac{\lambda_n^2}{D_\perp}$) from these quantities. The estimated values of parallel transport times for long and short $L_\parallel$ are approximately 200 μs

and 25 μs respectively. Similarly the radial transport times in the long and short $L_{\parallel}$ regions are approximately 100 μs and 12 μs respectively. Thus, nearly constant density at radial distance less than 5 mm may be attributed to the long connection length. The long and short connection lengths in the same discharge may be due to limited contact area of the plasma boundary with the limiter [see Fig. 5.1]. We also observe a small increase in plasma density and significant decrease in floating potential during the GP [see Fig. 5.5(f) and 5.5(g)].

We have measured electron temperature by using floating triple probe system, with a constant battery biasing (V_B) = 80 V for a pair of two pins. The plasma floating potential of the third pin with respect to the positive potential of the pair of two pins (V_d) is measured for determining the electron temperature, T_e. We use the following relation for determining T_e: $T_e = V_d/ln(2)$. In order to obtain good linearity between measured potential V_d and T_e, the following condition satisfies: $V_B > 2T_e$ [77]. Since the maximum expected SOL electron temperature is $\sim 20eV$ [15], the applied V_B is sufficient for application of this condition. Figure 5.7(a) shows the radial profile of the mean potential measured by using all three pins (Pin 4, Pin 5 and Pin 7) in discharges without/before and during the GP. The poloidal flow velocity V_θ is determined from the fitted potential profile and shown in Fig. 5.7(b), and it is in ion diamagnetic drift direction. It is observed that V_θ has a nearly constant value of 0.5 m/s during the GP.

5.3.1 Effect of GP on Electron Temperature, Potential Fluctuation and Density Fluctuation

Figure 5.8(a) shows the effect of GP on the electron temperature T_e and Fig. 5.8(b), shows radial profile of measured T_e before or W/o and during the GP in the SOL region. Before or W/o GP, the temperature vary in the range of 5 eV to 20 eV with a gradient scale length of 15 mm. It is observed that GP leads to about 50% reduction in electron temperature taking place at 1.5-2 ms after the end of voltage pulse on the GP valve. The total time required for recovery of T_e to its original value is in the range 2.7-3.6 ms (not shown). It is possible that this recovery time is related to the global energy confinement time. Similar observation has been reported on the reduction of particle flux with the GP [105].

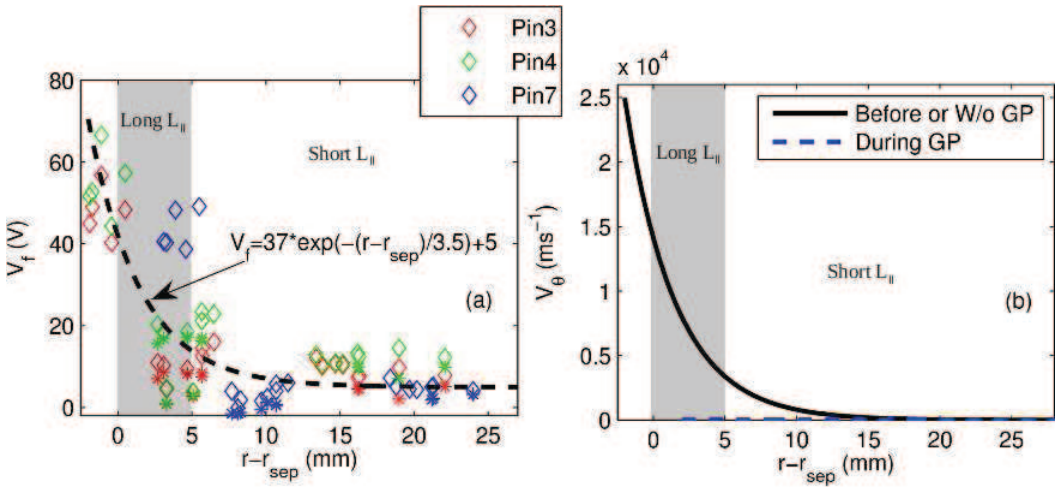

Figure 5.7: *Radial profiles of floating potential, and (b) $V_\theta = V_{E\times B}$. The vertical shadow bands indicate separation of long connection length SOL from the short connection length SOL (Limiter Shadow) region. The star symbol in the (a) are the corresponding measured values of v_f during the gas puff by the three pins.*

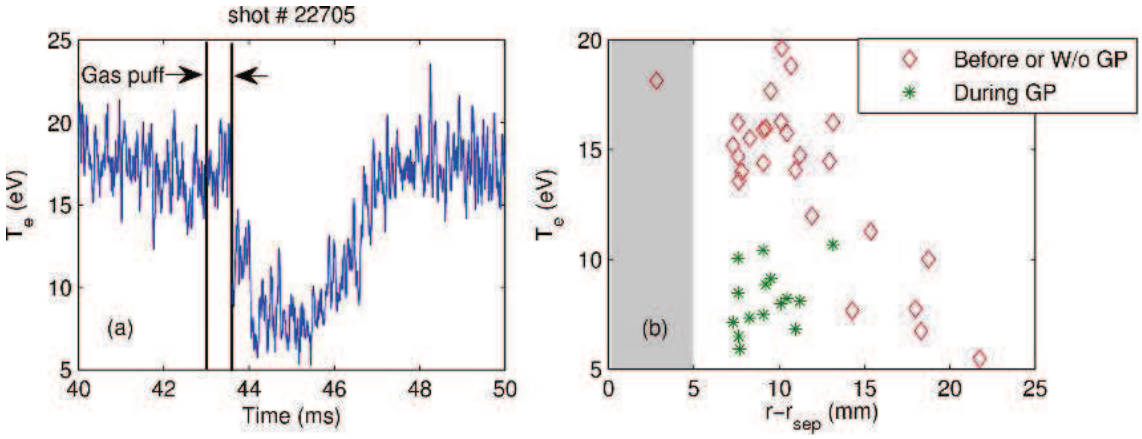

Figure 5.8: *(a) Effect of gas puff on electron temperature measured by the triple probe; the maximum reduction in electron temperature is observed about 1.5 ms after the end of the voltage pulse on the gas puff valve, (b) the radial profile of electron temperature before or W/o and during the gas-puff.*

Figure 5.9 shows the radial profiles of normalized ion saturation current fluctuation ($\tilde{I}_s/I_s$) and root mean square (rms) value of the floating potential (V_f) without/before and during the GP. It is observed that the normalized $\tilde{I}_s/I_s$ remains nearly the same in discharges before/without and during GP. On the other hand,

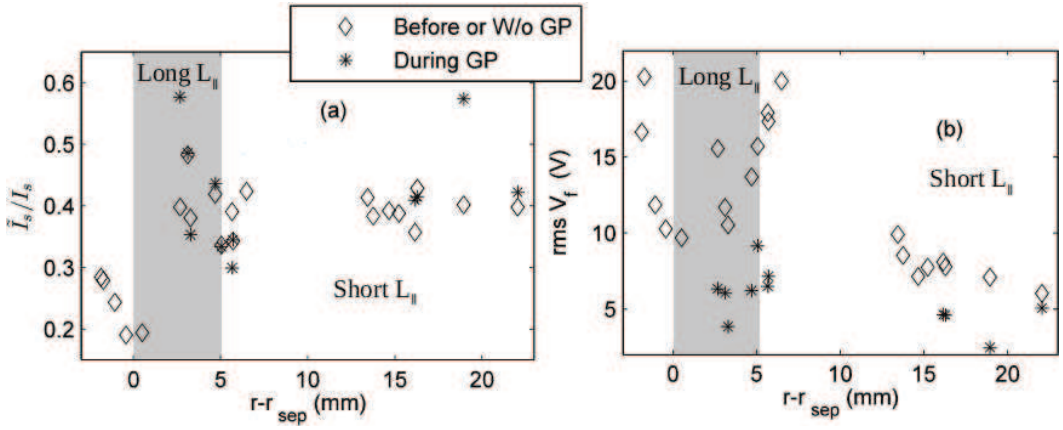

Figure 5.9: *Effect of gas puff on fluctuation of (a) ion saturation current and (b) floating potential. The fluctuation in ion saturation current is normalized but potential fluctuation is shown in the form of its root-mean-square (rms) value. The vertical shadow bands indicate separation of long connection length SOL from the short connection length SOL (Limiter Shadow) region.*

there is significant reduction in the V_f fluctuation during the GP [see Fig. 5.9(b)]. The observed increase in $\tilde{I}_s/I_s$ inside the SOL region is consistent with previous measurements [106, 107].

5.3.2 Effect of GP on Plasma Transport

Figure 5.10 shows the experimentally determined radial profiles of particle flux (Γ_r) and Mach number (M) and Fig. 5.11 shows the dependence of Γ_r on M. We now use the measured values of various lengths in order to show the consistency of measurements. For example, the perpendicular diffusion coefficient ($D_\perp$) can be estimated from the relation: $\Gamma_r = D_\perp\, n_{eb}/\lambda_n$, where λ_n is the density gradient scale length. By assuming $\lambda_n \sim 15\ mm$, the estimated value of $D_\perp \sim 5\ m^2 s^{-1}$. We have estimated $D_\perp$ at the SOL near the radial port and find the value same. The Γ_r decay length, λ_Γ, can be determined from the data in Fig. 5.10(a) and it is ~10 mm. This is comparable to the value estimated from the relation $\lambda_\Gamma = (\lambda_n^{-1} + 0.5\lambda_T^{-1})^{-1}$, where λ_T is the decay length of electron temperature. By assuming $\lambda_T \sim 15$ mm, we estimated value of $\lambda_\Gamma \sim 10$ mm, which is similar to the experimentally determined value.

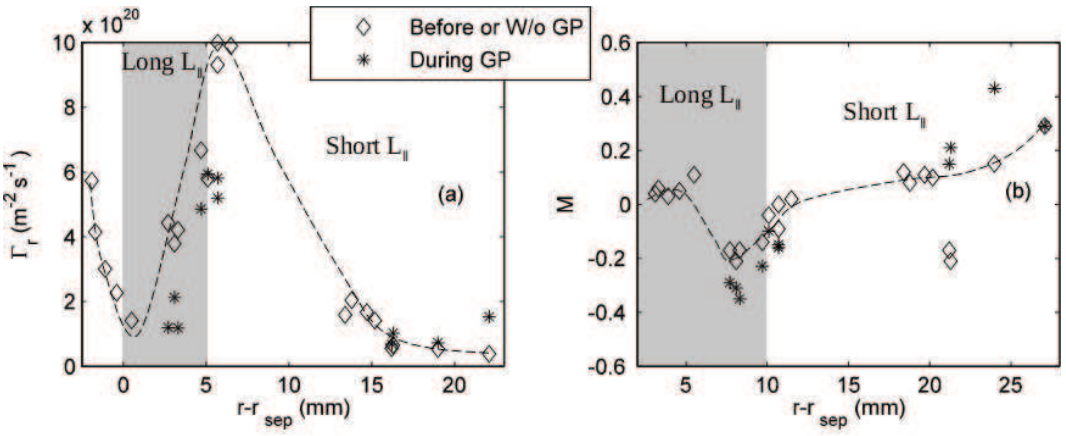

Figure 5.10: *Radial profiles of (a) particle flux, $\Gamma_r = \langle \tilde{n}\tilde{v_r} \rangle$, and (b) toroidal Mach number M. The vertical shadow bands indicate separation of long connection length SOL from the short connection length SOL (Limiter Shadow) region. The dashed lines are eye-fits.*

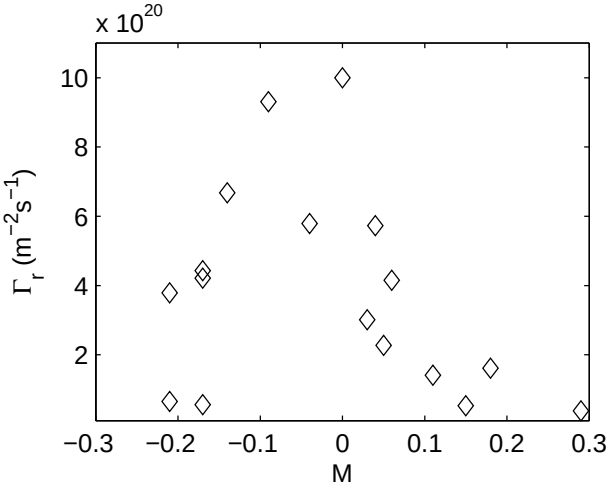

Figure 5.11: *The Particle flux, $\Gamma_r = \langle \tilde{n}\tilde{v_r} \rangle$ variation with the toroidal Mach number M. It indicates the importance of the plasma flows in controlling the radial transport of particles.*

Another observation is the fall in the particle flux in the long connection length region and peak in the short connection length region of the SOL. We have observed that the long $L_\parallel$ region falls into the velocity shear region [see Fig. 5.7(b)], and short $L_\parallel$ region is outside the shear region. The maximum radial transport is

observed outside the velocity shear region [see Fig. 5.10(a)]. The radial profile of particle flux [see Fig. 5.10(a)] shows a minimum at r-r_{sep}= 0 which corresponds to the center of the ∼10 mm shear region, estimated from radial profile of poloidal flow velocity and parallel Mach number from Fig. 5.7(b) and Fig. 5.10(b) respectively. The observed profile [Fig. 5.10(a)] agrees with the profile reported in [40, 108].

The Mach number is defined as $M = v/C_s$, where v is the plasma flow velocity and C_s is the ion acoustic speed. In order to calculate the Mach number, we make assumption of thin sheath and use the relation, $M = 0.43ln(J_{UP}/J_{DN})$, where, J_{UP} and J_{DN} respectively are upstream and downstream current densities of the Mach probe plates [30]. The positive and the negative values of M indicate that flows are towards ion drift face and electron drift faces respectively. The Mach number measurements are carried out at three discrete toroidal and poloidal locations as described earlier. Figure 5.10(b) shows that the Mach number profile has a shear in the long $L_{\|}$ region. Figure 5.11, shows dependence of Γ_r on the Mach number. We observe that the radial particle flux is maximum when the parallel Mach number is minimum. In presence of significant parallel Mach number, there is a decrease in the radial particle flux. It is possible that the shear layer near the LCFS plays a major role in the relation between the parallel Mach number and the radial particle flux as observed in Fig. 5.11.

5.3.3 Observation of Flow Reversal on the LFS Mid-plane with GP

Figure 5.12(a) shows ion saturation currents measured by the upstream and downstream side plates of the Mach probe. These measurements were taken at the LFS mid-plane, about 5 mm behind the last closed flux surface (LCFS). It is observed that the upstream probe current is larger than the downstream probe current, indicating that plasma flow is in the clockwise direction (i.e., towards the ion side of the limiter). This direction is the same as reported in our earlier observation [15]. However, there is flow reversal during the GP, because the probe current on the downstream plate is larger than that on the upstream plate. The direction and magnitude of the plasma flow recovers after the GP effect is over. The flow reversal can be explained as follows: The GP create pressure difference due to

local ionization source. This local buildup of pressure will equalize or wash out by the plasma flows along the field lines. As the GP location is on the ion side of the probe position, it creates plasma flow in the anticlockwise (i.e. towards the electron side of the limiter) direction.

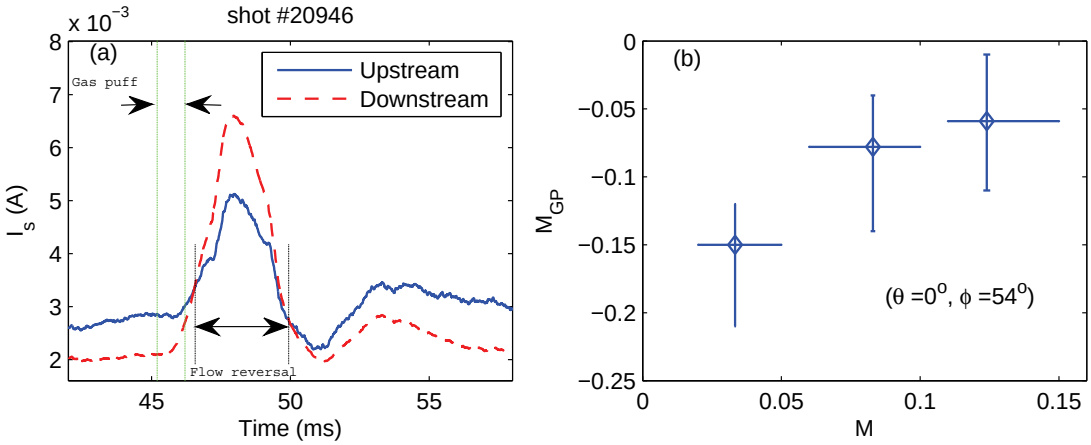

Figure 5.12: *(a) Ion saturation current on upstream and downstream probes before and during gas puff, after 2 ms smoothing, (b) Mach numbers measured before (M) and during gas-puff (M_{GP}) in several discharges. The error bar indicates the scatter in the data.*

Figure 5.12(b) shows the measured values of Mach numbers before (M) and during (M_{GP}) the GP. It is observed the during the GP, the Mach number changes sign, i.e., the flow direction reverses. The magnitude of M_{GP} is maximum, when the the magnitude of M is minimum. The change in Mach number, $M - M_{GP} \sim 0.18$ in all discharges. This indicates that the reversal is caused by the local particle source contributed by the GP.

5.3.4 Flow Pattern Just Behind The Limiter

Figure 5.13(a) shows the Mach numbers measured at three poloidal locations. As already explained, the positive/negative Mach number indicates that the flow is towards the ion/electron side of the limiter. Figure 5.13(b) shows the schematic diagram of the slab model of the SOL. The solid arrow at the probe locations

indicates the direction of plasma flow in discharges before/without the GP and dashed arrow indicates the same during the GP. The measured directions indicate that the flows may have shell structures connecting the long connection length regions with the short connection length (limiter shadow) regions. This may be explained by simulation results reported in [109]. The positive Mach number at $\theta = 0^o$ is consistent with the $E \times B$ drift direction. On the other hand, the negative Mach number at the $\theta = 45^o$ [see 'R' in Fig. 5.13(b)] and $\theta = 90^o$ [see 'T' in Fig. 5.13(b)] can be explained by the plasma flow from the outboard to the inboard. This flow may be caused by the difference in plasma pressure between outboard and inboard sides that is generated by the ballooning transport. This is a possibility because the probes at 'R' and 'T' locations may be connected to the inboard side in our case. The ballooning transport may be negligible on the outboard mid-plane [i.e., at the location 'O' in Fig. 5.13(b)] [25].

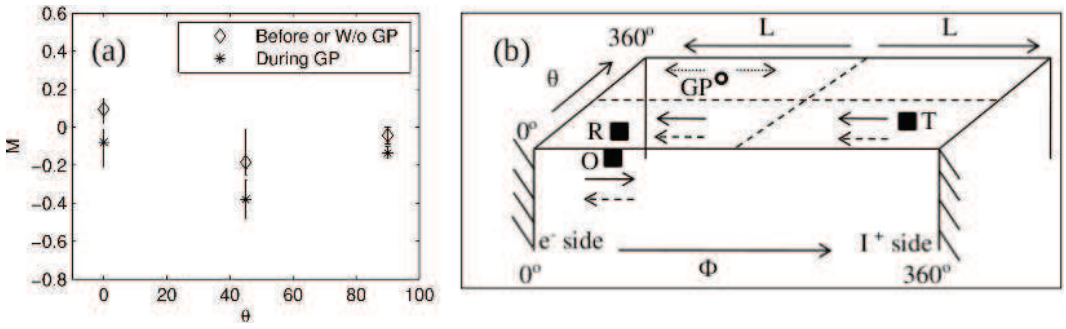

Figure 5.13: *(a) Parallel Mach number measured at three poloidal locations and just behind the limiter, (b) slab model of the SOL showing probe positions and measured flow directions. The probe locations are shown by 'T', 'R' and 'O' indicating Mach probes at the top, radial and outboard mid-plane respectively, 'GP' indicates the location of gas puff valve. The solid and dashed arrows show the flow directions before/without and during gas puff. The dotted lines at the 'GP' location indicate the flow directions because of local ionization source by gas puff. The error bar in (a) shows the scatter in the data.*

During the GP, the flow reversal at the $\theta = 0^o$ and increase in the Mach number at $\theta = 45^o$ and $\theta = 90^o$ is observed. The increase in the Mach number at $\theta = 45^o$ and $\theta = 90^o$ locations can be explained by further increase in the plasma pressure imbalance caused by the GP. It is possible that in the gradient region [see Fig. 5.10(b)], the flow has contribution from other than neoclassical effects

discussed above. In particular, these effects may be caused by Reynolds stresses discussed in the next section.

5.3.5 Radial Profiles of Electrostatic Reynolds Stress During and Without GP

The Reynolds stress has been used to study the role of turbulence in generating mean flows and vice versa [42, 43, 44]. In these studies, the Reynolds stress is calculated from the fluctuating flow velocities, namely δV_r, δV_θ and δM in radial, poloidal and toroidal directions respectively. The ergodic assumption allows using time-averages for ensemble averages, namely, $\langle \delta V_r \delta V_\theta \rangle$ and $\langle \delta V_r \delta M \rangle$ for poloidal and toroidal Reynolds stresses respectively. It should be noted that $\langle \delta V_r \delta V_\theta \rangle$ may be used for studying the poloidal flow generation [44, 46] and $\langle \delta V_r \delta M \rangle$ may be used for studying toroidal flow generation [43, 46]. Figure 5.14 shows radial profiles of both these quantities. It is observed that between 4-8 mm behind the LCFS, $\langle \delta V_r \delta V_\theta \rangle$ have definite gradient in discharges without GP. This gradient gets washed out during the GP. Similarly the $\langle \delta V_r \delta M \rangle$ also have gradient in discharges without GP, which gets washed out during the GP. These observations are in agreement with previous measurements [42, 43, 44].

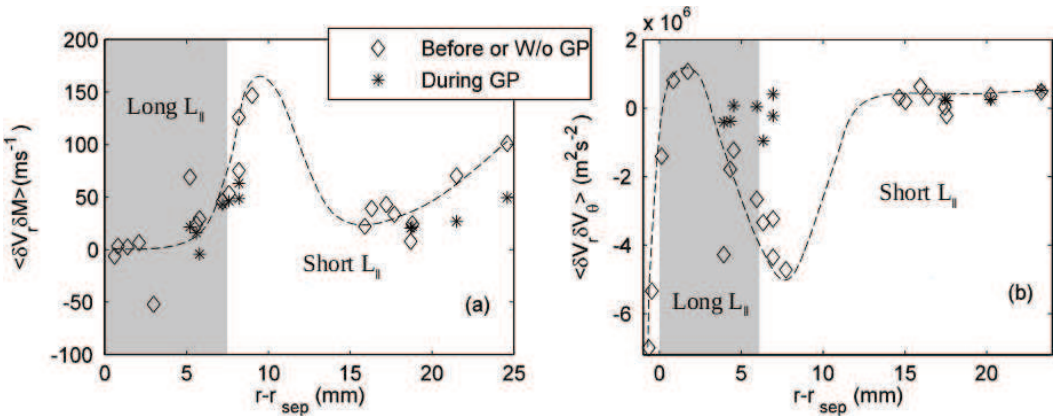

Figure 5.14: *Radial profiles of (a) $\langle \delta V_r \delta M \rangle$ and (b) $\langle \delta V_r \delta V_\theta \rangle$. The vertical shadow bands indicate separation of long connection length SOL from the short connection length SOL (Limiter Shadow) regions. The dashed lines show the eye-fits.*

We have estimated the radial-parallel momentum production rate ($P_{rM} = -\langle \delta V_r \delta M \rangle \frac{\partial M}{\partial r}$),

and radial-poloidal momentum production rate ($P_{r\theta} = -\langle \delta V_r \delta V_\theta \rangle \frac{\partial V_\theta}{\partial r}$), from the experimental data simultaneously. The negative production rate indicates that the turbulence acts as a momentum source for the the mean flow, and positive production rate indicates that the turbulence is the momentum sink. The estimated values of experimental momentum production rate for the parallel flows are $\sim 2.5 \times 10^3$ s^{-1} and $\sim$ -5 $\times$ 10^3 s^{-1} near the shear region [see Fig. 5.10(b), Fig. 5.14(a)]. The gradient in the Reynolds stress appears near the shear region. We now compare them with the rate required for a particular Mach number, $\frac{M_\parallel^2}{2\tau_c}$, from Ref [42, 43], where τ_c is the turbulence auto-correlation time (assumed 10 μs). The parallel momentum production rate, estimated from this equation is $\sim 2 \times 10^3$ s^{-1}, which is comparable to the measured production rate in the shear flow region. Similarly, we estimate poloidal momentum production rates as $\sim 3 \times 10^{12}$ W/kg and $\sim$ -3 $\times$ 10^{12} W/kg near to the shear region [see Fig. 5.7(b) and Fig. 5.14(b)]. We can estimate the power required per unit mass in the turbulence to derive the flows to the measured speed as follows: $\frac{V_\theta^2}{2\tau_c} \sim 1.2 \times 10^{12}$ W/kg, which is comparable to the measured values. The above estimation suggests the importance of production terms in both parallel and perpendicular flow dynamics. We also find that the turbulence acts both as a source and a sink in the SOL region. However, far into the limiter shadow region the turbulence and mean flow are decoupled. The dual role of turbulence acting both the source and the sink of mean momentum has been reported earlier by [42, 43, 44].

It should be mentioned here that our measurements show distinction between long connection length SOL and short connection length SOL, whereas previous measurements [42, 43, 44] report the distinction between the closed field line and open field line regions. Likewise, we use GP for studying connection between Reynolds stress and the mean flows, whereas earlier measurements used increasing plasma density [43], turbulent heating by current pulse [44] and ohmic discharges [42] for this purpose.

5.4 Summary

We have carried out measurements of plasma density, electron temperature, floating potential, Mach number, fluctuation induced particle flux and Reynolds stress near transition between the long connection length and the short connection length SOL regions. These measurements are carried out in ohmic heated discharges with and without GP. The plasma density is nearly flat in the transition region indicating the role of long connection length. Our measurements further show that electron temperature in the SOL region reduces to nearly half during the GP and it recovers to the original value in 2-4 ms after the GP. The poloidal flow velocity reduces nearly to zero during this period. Although the fluctuation in ion saturation current remains nearly same, the fluctuation in floating potential is significantly reduced with the GP.

An interesting observation is that the particle flux peaks when the parallel Mach number is near zero. It is possible that the shear in the poloidal flow velocity and parallel Mach number plays a major role in reducing the radial particle flux, as the maximum in the particle flux is outside the shear layer.

We have also constructed the flow pattern in ADITYA SOL plasma. It is observed that the parallel flow is towards the ion side in the limiter shadow but it is towards the electron side in the long $L_{\parallel}$ region of the SOL plasma at the top port. It is likely that the flow structure is a convective shell in the SOL region because of special SOL configuration in ADITYA tokamak. This has also been observed in the numerical simulation by Sharma et al. [109]. The flow direction is towards the electron side of the limiter at all three locations in the presence of GP near the limiter edge. Thus there is a flow reversal at the outboard midplane in the limiter shadow. This phenomenon can be attributed to the location of the GP valve and the source of local ionization of the gas.

We observe that the turbulence acts as a source and as a sink for both parallel and poloidal momentum in the shear region, which is at the near SOL. However both are decoupled into the far SOL. On the other hand the turbulence and mean flow are decoupled everywhere during the GP.

Chapter 6

Identification of Drift Driven and Transport Driven Flows

6.1 Introduction

The measured Scrape-off layer (SOL) flows, in ADITYA [see Chapter 4 and 5], and in the other tokamaks [5, 6, 11, 12, 13, 15, 19, 22, 23, 25, 28, 33, 36, 37, 45, 84, 89, 110, 111, 112] can be divided into symmetric and asymmetric components with respect to directions of the toroidal magnetic field B_T and plasma current I_p. The latter defines the helicity of the total magnetic field [12, 112], which is classified either as the positive helicity or, as the negative helicity depending on orientations of the total magnetic field.

In any helicity, plasma flows contains both symmetric and asymmetric components. The symmetric component of the flows are transport driven and the asymmetric driven flows are drift driven flows. The symmetric component does not depend on the direction of toroidal magnetic field, B_T and plasma current, I_p, and the asymmetric component depends on the direction of B_T and I_p. The symmetric component, known as transport driven component, is generated by the pressure gradient force. Examples are, difference in the particle flux in the low field side (LFS) and the high field side (HFS). This difference is caused by the ballooning transport perpendicular to the field line [6, 12, 25, 112]. Similarly, pressure gradient along the field line is caused by the particle/energy sink at the limiter. The

asymmetric components, known as drift driven components of the flow, are caused by various drifts, including $E \times B$ drift, diamagnetic drift and Pfirsch-Schluter (PS) flow. Although the flow velocity measured in most experiments refer to the total flow velocity, i.e., the sum of symmetric and asymmetric components, it should be clearly understood that the origin of both components are different. In order to study the role of plasma flow on global confinement times, it is important to determine the transport-driven flow.

Experiments have been carried out in TCV and Alcator C-Mod tokamaks in order to isolate transport driven components [12, 13, 25, 112]. The experiments on TCV tokamak have shown a reversal in the direction of plasma flow when the directions of both B_T and I_p are reversed while keeping their magnitudes and helicity same [13]. This observation indicates that the symmetric, or transport-driven, component is (10-20 %) of the plasma flows near the separatrix. On the other hand, the experiment on Alcator C-Mod tokamak has shown significant amount of symmetric or transport-driven component. In this case also the magnetic field helicity is kept unchanged when directions of B_T and I_p are reversed [12]. More detailed experiment has been reported recently on the transport-driven plasma flows by simultaneous measurements on the low field side (LFS) and high field side (HFS) SOL [112]. The experiment on Tore Supra has shown that the transport-driven flow depends on the location of the plasma contact with the limiter [6]. We have reported similar observation on ADITYA tokamak, where the plasma contact with the limiter is on the LFS [15, 45].

In the present chapter, we report measurements of SOL plasma flow in ADITYA tokamak by changing directions of B_T and I_p and determine transport driven flow component. The measurements are carried out at two different helicities, and it is observed that the transport driven flow depends on the helicity of total magnetic field. We provide a possible explanation of the direction of the transport driven flow. We also determine drift driven flow components and find that the direction and magnitude is consistent with the $E \times B$ and PS flows. The rest of the chapter is organized as follows: Sec. II describes the experimental set up, Sec. III is devoted to the result and discussion and the summary is presented in Sec. IV.

6.2 Experimental Setup

We have carried out experiments in all four possible combinations of B_T and I_p directions by keeping their magnitudes nearly the same [see Fig. 6.1]. These combinations include: (a) $[B_T(C.W), I_p(C.W)]$, (b) $[B_T(C.C.W), I_p(C.C.W)]$, (c) $[B_T(C.W), I_p(C.C.W)]$ and (d) $[B_T(C.W), I_p(C.C.W)]$, where C.W and C.C.W represents clockwise and anti-clockwise direction as seen from the top of the torus.

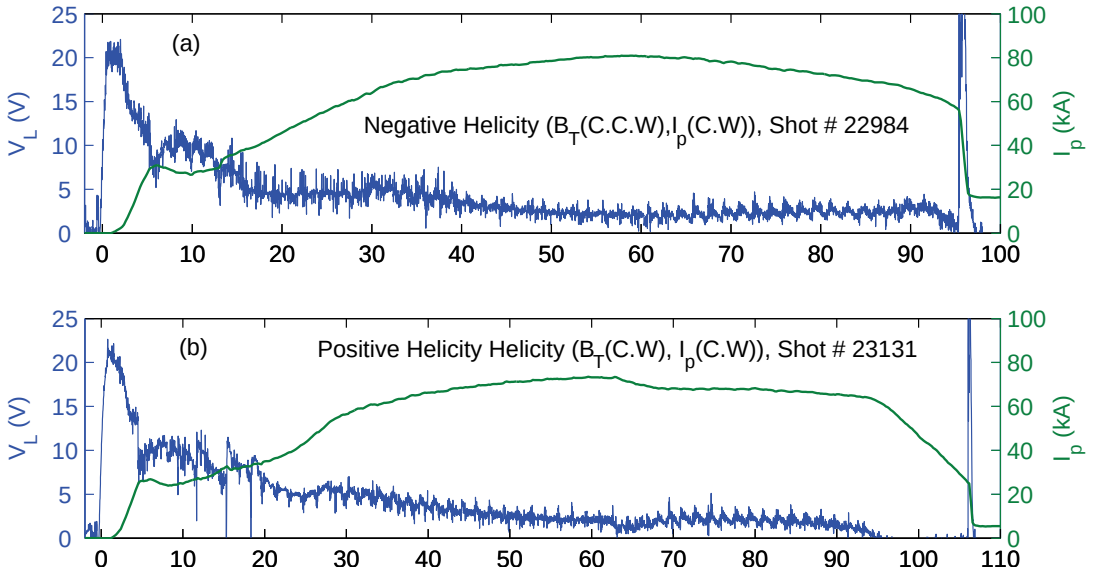

Figure 6.1: *(a) Loop voltage V_L and plasma current I_p signals of the typical ADITYA plasma discharge in (a) negative helicity, and (b) positive helicity. For negative helicity, when B_T and I_p are antiparallel, $[B_T(C.C.W), I_p(C.W)]$ is shown and for positive helicity, when B_T and I_p are parallel $[B_T(C.W), I_p(C.W)]$ case is shown.*

The experimental parameters are: the toroidal magnetic field on the axis $B_T = 0.75\ T$, plasma current $I_p \sim 80\ kA$, plasma duration $\sim 80\ ms$, core electron temperature $(T_e) \sim\ 300\ eV$, central plasma density $\sim (1-2)\times 10^{19}\ m^{-3}$ and scrape-off layer (SOL) plasma density is $(1-15)\times 10^{17}\ m^{-3}$. Measurements in the SOL plasma is carried out by using two identical probe-heads, mounted on the outboard side ($\theta = 45^o,\ \phi = 54^o$) and top port of the tokamak ($\theta = 90^o,\ \phi = 288^o$) respectively. Here, we use limiter location for the toroidal reference angle (*i.e.*, $\phi = 0^o$), and

the toroidal angle increases in the clock-wise direction as seen from the top of the tokamak. The poloidal reference angle (*i.e.*, $\theta = 0^o$) is on the outboard midplane, and the poloidal angle increases above the mid plane. The schematic diagram of the toroidal/poloidal locations of the probe-heads are shown in Fig. 6.2(a) along with the front and the side views of the probe-head. The ion saturation currents are measured at plates 1 and 2 and, pin 3, and, floating potentials are measured at pins 4,5 and 7. The flow Mach number is determined from measurements at the plates and particle flux is determined from measurements at pins 3, 4 and 5. The pins are of 1 mm diameter and 3 mm length and the plate dimension is 4×3 mm^2. The plates constitutes a magnetized Mach probe, because the ion larmor radius ~ 0.6 mm is much smaller than the plate dimension. The direction of B_T is such that the area vector of plates 1 and 2 are approximately parallel to B_T.

Since the plasma Debye length (λ_D) is $\sim$ 25 μm, the thin-sheath approximation is satisfied. Similarly, since the separation between different pins is 3 mm, the sheaths of the pins don't interact. The measurements at the pins are independent. Probe-heads are mounted on movable shafts, and measurements are carried out in a number of similar discharges on different days by moving probe-heads at different radial locations. It should be noted that the probes may be at different distances from the last closed flux surface (LCFS or separatrix) depending on the equilibrium position of the current channel [see Fig. 6.3 and Ref. [45]]. For measuring ion saturation current, all probes are biased to -100 V using the same power supply. The magnitude of the bias voltage is sufficient to keep all probes in the ion saturation regime.

The magnetic measurement shows that the plasma centroid remains in the 1^{st} quadrant in the counter-cases (i.e., B_T and I_p are anti-parallel). On the other hand, the plasma centroid position moves to the 4^{th} quadrant for co-cases (i.e., B_T and I_p are parallel) [see Fig. 6.3 and Fig. 6.4]. The co- and counter-cases represent two different helicities of the total magnetic field line. We have assumed the positive helicity of the total magnetic field for the co-cases and negative helicity for counter-cases. Measurements are grouped on the basis of same helicity.

Although measurements in a single helicity configuration are enough to separate

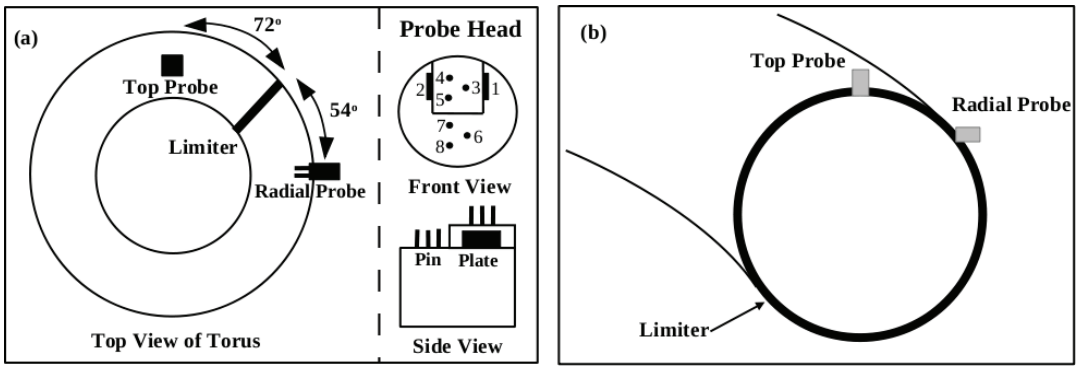

Figure 6.2: *(a) Schematic of the top view of the torus showing toroidal locations of probes with respect to the limiter and, the front and side view of the probe head. (b) The projection of the probes on the poloidal ring limiter (thick circle). The direction of B_T is such that the area vector of plates 1 and 2 are approximately parallel to B_T.*

out the transport-driven flow and the drift driven flow components, our experiments in two different helicities demonstrate that the transport-driven components also depend on the field helicity.

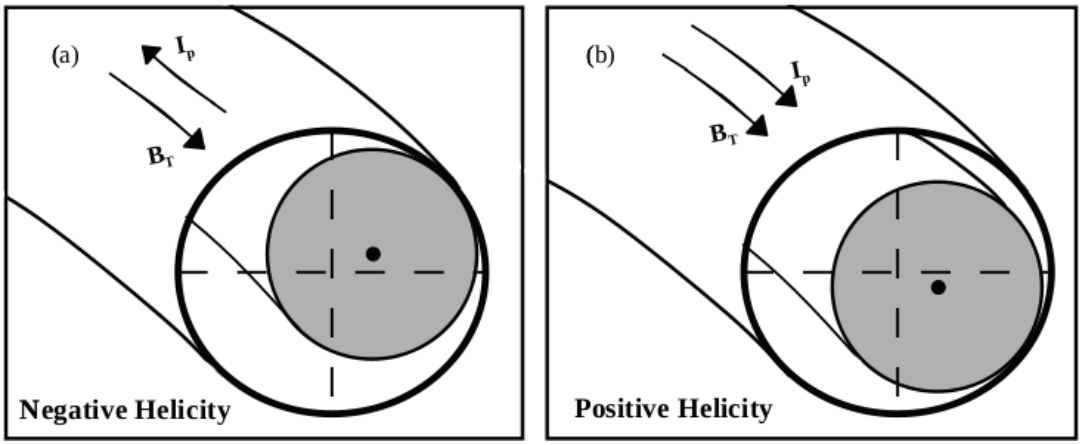

Figure 6.3: *Schematic of plasma position for, (a) negative helicity, and (b) positive helicity cases. The field helicity is determined by directions of the toroidal magnetic field (B_T) and the plasma current (I_p). The positive and negative helicity can be defined by $H = \frac{\mathbf{B_T}.\mathbf{I_P}}{B_T I_p}$, which gives ± 1 for co- and counter-cases. The shaded regions indicate the confined plasma (exaggerated). The limiter center is shown by the intersection of two dashed lines and plasma center by the dots.*

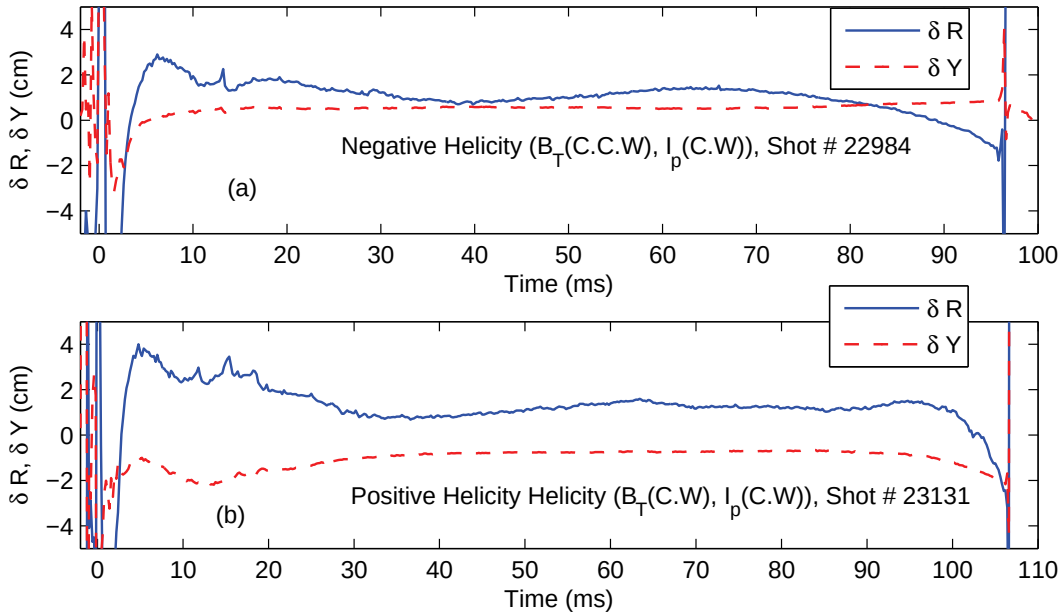

Figure 6.4: *Plasma column shift from the limiter center for, (a) negative helicity and (b) positive helicity. Here δR and δY are the horizontal and the vertical shifts, respectively. The δY shows that in the negative helicity, plasma centroid remains above the midplane, and remains below the midplane for the positive helicity.*

Figure 6.5 shows schematically the orientations of magnetic field line in both negative helicity and positive helicity configurations of the experimental set-ups [see Fig. 6.3].

6.3 Results and Discussions

The plasma flows are measured by Mach probe in terms of Mach numbers (M) by using the formula, $M = 0.43ln(J_{UP}/J_{DN})$, where J_{UP} and J_{DN} are the ion saturation current densities at the two plates of Mach probe [30]. We have taken the thin sheath approximation, the particle diffusivity equals the momentum diffusivity and assumed same ion temperature at two plates of the Mach probe. Here the positive/negative sign of M is assumed for the clockwise/counter-clockwise plasma flow as seen from top of the torus.

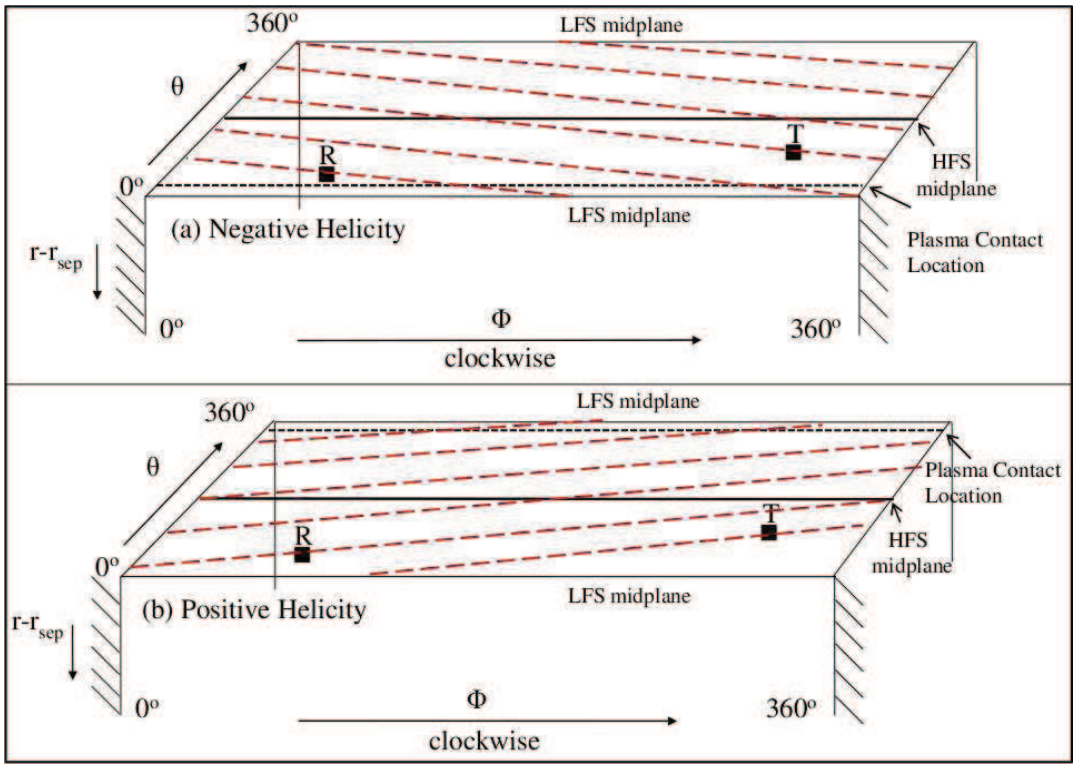

Figure 6.5: *Schematic 3D slab diagram of the SOL showing field line orientations for (a) negative helicity and (b) positive helicity. Two sides of the limiter are shown by hatched lines. The ϕ is the toroidal angle that increases in the clockwise direction as seen from the top of the torus and the θ is the poloidal angle; $\theta = 0^o$ indicates the low field side (LFS) midplane and increases above the midplane. The "T" and "R" indicate locations of the top probe and radial probe respectively. The high field side (HFS) midplane is shown by the thick line at $\theta = 180^o$. The plasma contact locations are $\theta \sim 20^o$ for the negative helicity and $\theta \sim 350^o$ for the positive helicity cases and shown by dotted lines. The total magnetic field lines are shown by the red dashed lines. The high pressure at the LFS midplane gives rise to anticlockwise flow in the negative helicity case and clockwise flow in the positive helicity case. This difference is because of different field line orientations in positive and negative helicity cases.*

The transport driven Mach number (M_{tr}) and the drift driven Mach number (M_{dr}) are related to the measured M by, $M_{1,2} = M_{tr} \pm M_{dr}$, where $M_{1,2}$ represents the measured M in two combinations of B_T and I_p directions for the same helicity [28, 112]. Here we have assumed that M_{tr} and M_{dr} are independent from each other. Experiments are conducted in two helicity configurations in order to deter-

mine if the M_{tr}-values depend on the field helicity and also to determine the effect of poloidal locations of plasma-limiter contact on these values [see Fig. 6.3]. We have shown in the chapter 5 that the limited contact gives rise to both long connection length ($L_{\parallel}$) region and short connection length region in the SOL plasma of ADITYA tokamak. The estimated values of long $L_{\parallel} \sim 8$ m and short $L_{\parallel} \sim 1$ m [45].

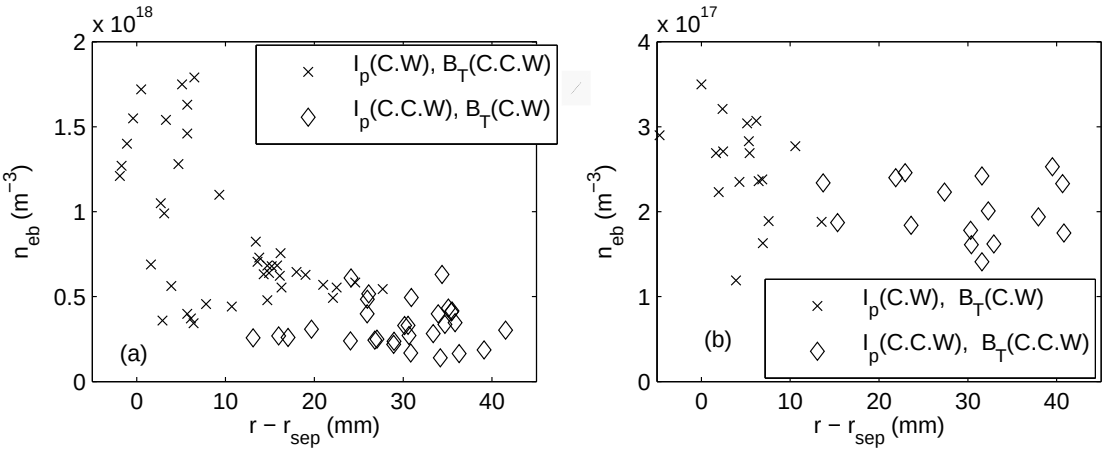

Figure 6.6: *The radial profile of plasma density in the edge region in, (a) negative helicity, and (b) positive helicity configurations of magnetic field, measured at the 'Top Probe'. Here each symbol is from individual shot data. The $r - r_{sep} = 0$ is the location of the LCFS.*

6.3.1 Radial Profile of Density and Floating Potential

Figure 6.6 shows the plasma density measured by the single Langmuir probe pin at the top port for both negative and positive helicities. The ion saturation current of the probe is used to determine plasma density by using the formula: $I_s = 0.5 n_{eb} e A C_s$ [73], where e is the electronic charge, A the probe area and ion sound speed, $C_s = 45\ km/s$. For calculating the value of $C_s = \sqrt{2T_e/m_i}$, we have assumed constant $T_e = T_i = 10\ eV$ in the SOL [15]. The variation in C_s is proportional to $\sqrt{T_e}$. It is observed that the average plasma density near the separatrix for the negative helicity is ~ 3 times larger than that for the positive helicity case. However, a systematic database is required to confirm this difference.

Since the edge plasma densities presented in Fig. 6.6(a) and Fig. 6.6(b) are measured by using the 'Top Probe', which is at ion/electron sides of the limiter for different I_p directions, the difference may not be because of the shadow effect of the limiter. The effect appears to be related to the distance between the probe location (i.e., top port) and the plasma-limiter contact point. In the positive helicity case, the plasma centroid position is shifted to the bottom of the machine [see Fig. 6.3] and hence the effect may be because of the field line orientation, which connects the probe to the limiter [see Fig. 6.5]. It is possible that the longer connection length gives the smaller density.

The distance of both top and radial probe heads are ~ 1 m from the limiter and the estimated probe collection/shadow length ($l^2 C_s/D_\perp$) is ~ 0.1 m for $D_\perp \sim 5\ m^2/s$ [15, 45]. Thus the collection length is 10 times smaller than the distance between the probe and the limiter. In case of flowing plasma, the pre-sheath length increases in the downstream probe and decreases in the upstream direction. The effect of plasma flows on the probe measurements have been studied by Hutchinson [30, 86]. It can be concluded from these studies that some effect may be expected only upto ~ 5 times the shadow/collection length for M ~ 1. Since in our case, the distance of the limiter is 10 times the probe shadow length, its effect on the plasma density measured by the probe is negligible. Since the flow Mach number is determined from the ratio of plasma density in the upstream and downstream directions, we expect that there is no influence of the limiter on the Mach numbers.

In these experiments, the central chord-averaged plasma density is (1-2)$\times 10^{19}\ m^{-3}$ and central electron temperature in the range (275-325) eV and the plasma current is 80$\pm$8 kA. The probe head is kept at some distance from the limiter leading edge. Since the plasma position is not feedback controlled, the probe position with respect to the last closed flux surface (LCFS) vary in different discharges. It makes difficult to measure the full radial profile. The position of the probe head is changed after 10-15 discharges.

The floating potential V_f measured at top and radial locations are shown in Fig. 6.7 for the negative helicity case. As pointed out earlier, even if the helicity is the

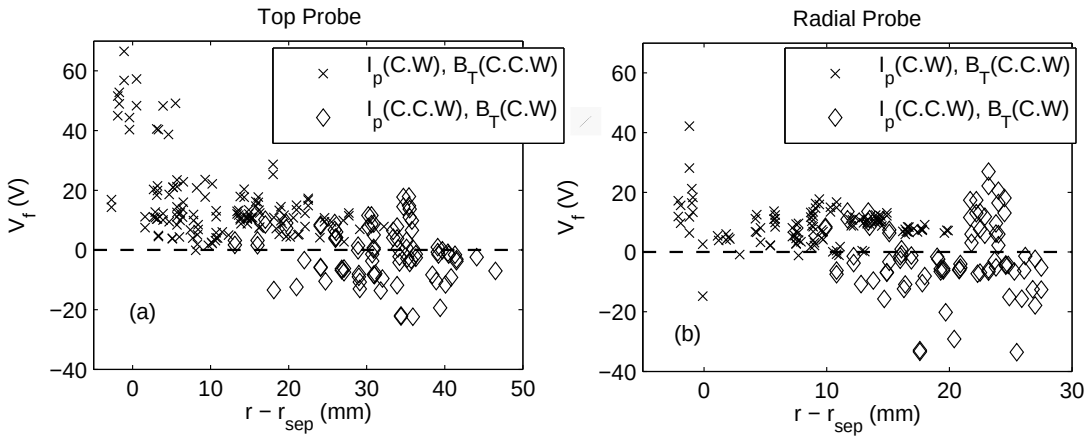

Figure 6.7: *The radial profile of the floating potential at two locations measured by: (a) Top Probe and (b) Radial Probe for the negative helicity case. The data from all three pins are included [45].*

same, the direction of B_T can be either clock-wise (C.W.) or counter-clock-wise (C.C.W.). It is observed that the V_f changes sign with the change in the direction of B_T. Whether the plasma is rich in electrons or ions determines the sign of the V_f. This is consistent with the $B \times \nabla B$ drift of the electrons/ions. Our observation is in agreement with earlier observation on Alcator-C tokamak [97]. It is observed that the gradient in the near SOL is well defined for the 'Top Probe' and not so well defined for the 'Radial Probe'. We expect that the velocity shear layer may have a role to play, which is more pronounced for the long connection length region [45]. It is further observed that at both locations there is a flattening of the floating potential profile in the far SOL.

6.3.2 Poloidal Asymmetry in Particle Flux and Density

Figure 6.8 shows the radial profiles of fluctuation induced radial particle flux $\Gamma_r = \langle \tilde{n}\tilde{v}_r \rangle$ and plasma density, calculated from probe measurements. It shows that particle flux near the LCFS is less on the 'Top Probe' than that on the 'Radial Probe'. This is clearly a signature of 'Ballooning Effect'. We have further verified that the rms (root mean square) values of ion saturation current fluctuations on the 'Top Probe' is between 2 mA to 10 mA and that in the 'Radial

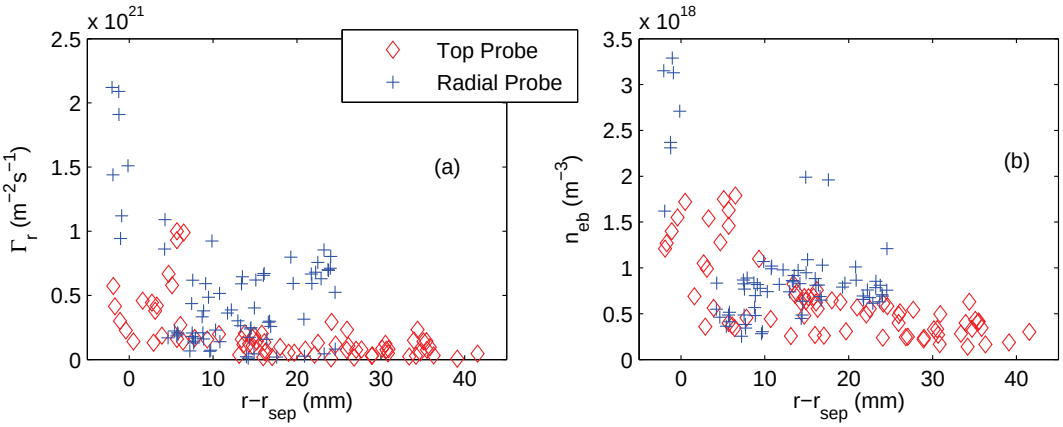

Figure 6.8: *The radial profile of (a) particle flux, and (b) plasma density at the 'Top Probe' and the 'Radial Probe', in the negative helicity case. Both particle flux and plasma density are larger at the 'Radial Probe' near the last closed flux surface (i.e, $r - r_{sep} \sim 0$) as compared to those at the 'Top Probe'. This indicates presence of ballooning effect.*

Probe' is between 4 mA to 20 mA. The normalized rms (root mean square) values of ion saturation current fluctuations in the 'Top Probe' is between 0.2 to 0.6 and that in the 'Radial Probe' is between 0.3 and 0.9. This may be due to the 'Ballooning Effect'.

The large scatter in density and flux data at the same radius (see Fig. 6.6 and Fig. 6.8) is because the data points were taken from different discharges on different days/times, and thus, the scatter might be because of the shot-to-shot variation. The particle flux at the 'Radial Probe' is approximately two times that at the 'Top Probe' near the last closed flux surface (LCFS). The same conclusion may be drawn for the plasma density also. The prominence of particle flux and plasma density at the 'Radial Probe' may be attributable to the ballooning effect. This information may be used to determine the role of ballooning transport in the transport driven flow.

6.3.3 Transport and Drift Driven Mach Number

Figure 6.9 shows radial profiles of Mach number for negative helicity cases. The reversal of B_T and I_p keeps the helicity same but there is a drastic change in the

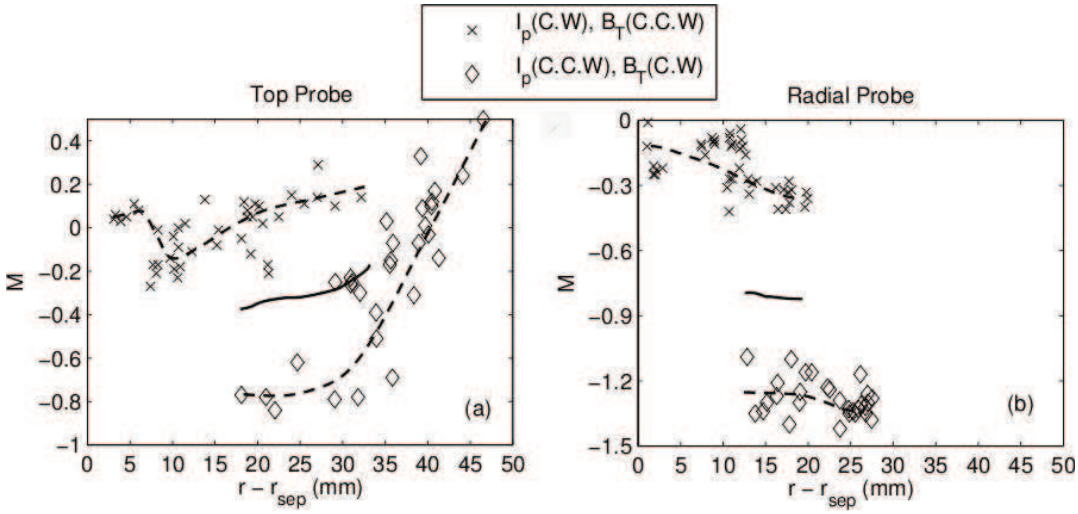

Figure 6.9: *Radial profiles of Mach number, measured by, (a) Top Probe, and by (b) Radial Probe. Both measurements are for negative helicity cases. The dashed line is the hand-fit to the respective data and the solid line is the transport driven Mach number, calculated by the average of dashed lines (only for common radial distances). The negative transport driven Mach number at both top and radial probes shows that the transport driven flow is in counter-clockwise direction as seen from top of the torus.*

Mach number profiles. If the ion drift determines the total flow, the Mach number should have nearly the same magnitude but with opposite sign, which is not observed in ADITYA. On the other hand, our observation indicates that there is a significant contribution of transport driven component in the measured Mach number. This component is found by averaging the Mach number in the two magnetic field configurations (only at common radial distances). At both probes, the transport driven Mach number has the same sign, which indicates that the flow direction is the same.

The estimated value of E_r is $\sim 3.5 \times 10^3 V m^{-1}$ and the estimated value of $v_{E_r \times B_\theta} \sim C_s$ with $B_\theta = 0.07\ T$. On the other hand, the estimated value of PS flow is $v_{PS} \sim 2 q_s v_\perp cos\theta \sim 0.1 C_s$, where $v_\perp = E_r/B_\phi - \Delta_r p / e n_{eb} B_\phi$ and $\Delta_r p$ is the radial pressure gradient [45].

Another observation in Fig. 6.9(b) is that M > 1, for a particular magnetic con-

figuration (i,e., $I_p(C.C.W), B_T(C.W)$). It can be explained as in the following: It is estimated that in this configuration the components of plasma flow due to PS flow, $E_r \times B_\theta$ drift, ballooning transport and sink action of the limiter are all in the same direction so that they add to give the total Mach number, M > 1. Similar observation has been reported from other tokamak also [6, 12, 25, 37].

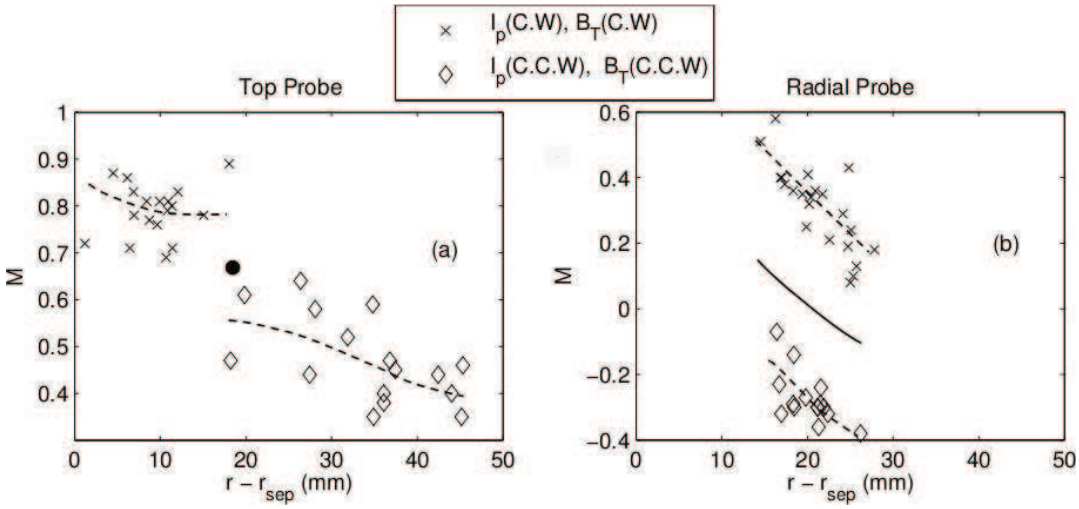

Figure 6.10: *Radial profiles of Mach number, measured by (a) 'Top Probe', and (b) 'Radial Probe' for positive helicity cases. The dashed line is the hand-fit to the respective data and dot/solid line is the transport driven Mach number, calculated by the average of dashed lines (only for common radial distances). The positive transport driven Mach number shows that this part of flow is in the clockwise direction as seen from top of the torus.*

Figure 6.10 shows radial profiles of Mach number for the positive helicity cases, for both the 'Top Probe' and the 'Radial Probe'. We have determined M_{tr} by averaging the Mach numbers at common radial distances. It is observed that for the 'Top Probe', M_{tr} is obtained only at a single radial distance, but for the 'Radial Probe', a radial profile is obtained. At the 'Radial Probe', there is a reversal in the sign of the measured Mach number, when both toroidal magnetic field and plasma current are reversed [see Fig. 6.10(b)].

Figure 6.5 shows the model of field lines in both negative and positive helicity cases, which is used to explain the direction of transport driven flows in ADITYA SOL plasma. In the negative helicity case, the transport driven flow is in the counter-

clockwise direction as shown in Fig. 6.9. We explain this observation as follows: The ballooning effect gives rise to higher pressure at the LFS as compared to that at the HFS. The pressure gradient causes flow from LFS to HFS. We have estimated that the particle diffusion coefficient in ADITYA tokamak is $D_{\perp} \sim (5-10) m^2/s$, by assuming that the diffusion obeys Fick's law [15, 45]. Similar estimation can be made for the data presented in Fig. 6.8. Now we estimate the diffusion co-efficient by assuming that the particle flux has ballooning-like continuity [112]. Accordingly the diffusion coefficient may be given by $D_{ballooning} \sim L_n V_r$, where V_r is the mean radial velocity of particles due to ballooning like continuity and L_n is the density gradient scale length. We have estimate from the assumption of ballooning-like continuity that $V_r \sim 1000$ m/s [112]. By substituting, $L_n \sim 10-15$ mm and $V_r \sim$ 1000 m/s, we obtain $D_{ballooning} \sim$ (10-15) m^2/s. The similarity, $D_{\perp} \sim D_{ballooning}$ withing a factor of 2, indicates that the ballooning transport may be responsible for the transport driven flow in ADITYA tokamak.

As described earlier, the direction of the transport-driven flow is positive (clockwise) in positive helicity case (see Fig. 6.10) and negative (counter-clockwise) in negative helicity case (see Fig. 6.9) . Why should field helicity determine the direction of the transport-driven flow ? Since the magnetic field constraints the plasma particle movement, the direction of plasma flow should depend on the helicity (field orientation) of the total magnetic field [see Fig. 6.5]. Let us assume that the probe is located at the top port. The LFS is connected to the top probe "T" in the clockwise/counter-clockwise directions for positive/negative helicity cases [see Fig. 6.5]. This will cause transport-driven flows in clockwise/counter-clockwise directions for the positive/negative helicity cases. Same observation can be made for the radial probe "R" from Fig. 6.5. The limiter sink action effect on the flow M is also seen at the radial probe [see Fig. 6.9(b) and Fig. 6.10(b)] as this probe is in the limiter shadow for most of the shots.

6.4 Summary

We have presented measurements of Mach numbers in the SOL plasma of ADITYA tokamak for positive as well as negative helicities of total magnetic field. The posi-

tive and negative helicities are obtained by reversing the directions of both toroidal magnetic field and plasma current. The negative helicity is obtained when both plasma current and toroidal magnetic field are in opposite (or, counter-) directions. Two possibilities exist for the negative helicity. Similarly, the positive helicity is obtained when toroidal magnetic field and plasma current are in the same (or, co-) directions. Two possibilities exist for the positive helicity also.

It is observed that when directions of toroidal magnetic field and plasma current are reversed but the helicity is kept unchanged, there is a change in the magnitude and direction of plasma flows. Since the change is observed in both the magnitude and the direction, it is concluded both flow components, transport and drift driven are present in the ADITYA. The $E \times B$ and PS flows are observed to be the main factors behind the drift driven flow component.

On the other hand the transport driven flow is caused by the pressure gradient forces, which includes the sink action of the limiter and the ballooning transport, i.e., excess particle transport on the outboard side compared to that on the inboard side. We have verified the existence of ballooning transport by direct measurement of particle flux and density at the LFS and the top port. The ballooning nature of transport should be verified by making simultaneous measurements on the inboard side (HFS) and the outboard side (LFS).

The existence of gradient in floating potential profile indicates significant poloidal flows. This aspect may be further explored by installing Gundestrap probe that measures the poloidal flow. These two aspects will be explored in future experiments.

Chapter 7

Conclusions and Future Scope

7.1 Conclusions

The SOL plasma is the skin of the main plasma; it protects the main plasma, and can affect the main plasma properties. All the plasma surface interaction takes place in the SOL and this interaction depends on SOL plasma properties. In recent years the existence of the plasma flows in the SOL has been observed and found that the SOL plasma flows can affect the main plasma, which includes the confinement improvement and impurity reduction. The various causes behind these flows are observed and they include Pfirsch-Schluter (PS) flows, $E \times B$ drift, diamagnetic drift , limiter/divertor sink action and the poloidal asymmetry in the particle transport.

In ADITYA, the limiter plasma contact point is only in the limited poloidal region not in the whole poloidal span. That makes the SOL of ADITYA special. In this configuration the outer SOL plasma field lines may be connected to the inner SOL field lines, which is not possible if plasma touches the limiter symmetrically. The effect of this special configuration has been observed in the ADITYA measurements. We have carried out experiments to establish the flow pattern and how it is affected by a small puff of the working gas, and to identify transport and drift driven components of the measured flows. We have used the Mach probes at different toroidal and poloidal locations to measure the flows. ADITYA SOL flow measurements will help to improve and to add to the existing database from other

tokamaks.

In chapter 4, we have presented the SOL flow along with the other properties in the low toroidal magnetic field $B_T = 0.2\ T$ and low plasma current $I_p \sim 25\ kA$. The directions of both I_p and B_T are in the clockwise (C.W), as seen from the top of the torus. The measured floating potential (V_f) at the top of the plasma shows the negative values, which is consistent with the $B \times \nabla B$ direction. The limited contact of the limiter with plasma column gives both short and long connection length $L_\parallel$ in the SOL. Its effect has been observed in the density decay length at the top port and the radial port. We have also observed the dependence of toroidal Mach number (M) on the radial distance from the last closed flux surface (LCFS) and local plasma density. Our observations confirm reports from other tokamaks. For example, we observe that M increase with the radial distance from the LCFS and the decrease of the M with the increase in the average local plasma density is similar to observation from other tokamaks. Decrease in the M at the higher densities indicates the possible role of the radial electric field in the ADITYA SOL. The $E \times B$ drift and the PS flows of ions are observed to have significant contributions to the measured M and the sink action of the limiter opposes the two. On the other hand, the contribution of the ballooning type transport at the outboard midplane is negligible. The measured toroidal flow direction is towards the ion side of the limiter and the poloidal flow direction is towards the contact of the LCFS with the limiter.

Sometimes the measured plasma flows can be be explained by the simple drift and transport driven flows. In some tokamaks the interplay between the mean plasma flows and the turbulence has been observed, and have been used to explain the measured flows. In ADITYA we have carried out measurements to look for the similar effects along with the effect of the gas puff (GP) on the SOL flows and other parameters. In chapter 5, we have reported these measurements in high $B_T = 0.75\ T$ and high $I_p \sim 80\ kA$. Different measured quantities are: plasma density, electron temperature, V_f, M, fluctuation induced particle flux and Reynolds stress near transition between the long and short $L_\parallel$ SOL regions during and before or without GP. The plasma position measurements show that for this counter combination of B_T counter clockwise (C.C.W) and I_p (C.W) the plasma centroid

remains in the first quadrant. At the top port plasma density is nearly flat in the transition region indicating the role of long $L_{\parallel}$. Measured electron temperature at the top of the plasma in the SOL region reduces to nearly half during the GP and it recovers to the original value in 2-4 ms after the GP. The poloidal flow velocity $V_\theta = E \times B$ reduces nearly to zero during this period. On the other hand, the fluctuation in ion saturation current remains nearly same and the fluctuation in floating potential shows significant reduction.

The shear in the poloidal flow velocity and M is observed near the transition of long to sort $L_{\parallel}$ region. The fluctuation driven particle flux peaks when the parallel Mach number is near zero, and it shows the role of parallel flows in reducing the radial particle flux. Similarly, the particle flux decreases with increasing shear in the M. We have further observed that the turbulence acts as a source and as a sink for both parallel and poloidal momentum in the long to short $L_{\parallel}$ transition region. However both are decoupled into the far SOL. On the other hand, the turbulence and mean flow are decoupled everywhere during the GP.

The SOL flow pattern is constructed by measuring Mach numbers at three different toroidal and poloidal locations, and it is observed that the parallel flow is towards the ion side in the limiter shadow ($L_{\parallel}$) but it is towards the electron side in the long $L_{\parallel}$ region of the SOL plasma at the top port. It is likely that the flow structure forms a convective shell in the SOL region because of special SOL configuration in ADITYA tokamak. The flow direction is towards the electron side of the limiter at all three locations in the presence of GP near the limiter edge. Thus there is a flow reversal at the outboard midplane in the limiter shadow. This phenomenon can be attributed to the location of the GP valve and the source of local ionization of the gas. The measured M has contributions from the ballooning type transport, PS flows, $E \times B$ drift and limiter sink action.

Our measurements presented in chapter 4 and 5 indicate that ADITYA has two types of flow components: drift driven and transport driven. The transport driven and drift driven components are independent and dependent respectively on the B_T and I_p directions. The observed differences in the M presented in chapter 4 and 5 may be because of the different magnitude of B_T and I_p and different direction

combinations of B_T and I_p.

In chapter 6, we have presented measurements of M, carried out at the top of the plasma and at the outboard side (away from the midplane), for all four direction combinations of B_T and I_p, in order to separate the drift driven Mach number M_{dr} and the transport driven Mach number M_{tr}.

Measurements are divided according to positive and negative helicities of the total magnetic field. Both positive and negative helicities consist of two direction combinations. The B_T and I_p are in same direction for the positive helicity case, in different direction for negative helicity case. The estimations are carried out by using: $M_{1,2} = M_{tr} \pm M_{dr}$, where $\pm$ is for the two direction combination of the same helicity. The plasma centroid position is in the first and fourth quadrant for negative and positive helicity cases respectively. The flow has been measured at top of the plasma and at the outboard side above the midplane. We have observed that for the both cases, there is a change in the magnitude and direction of plasma flows. The change in both the magnitude and the direction of flows indicates the presence of both transport and drift driven components. The $E \times B$ and PS flows are observed to be the main factors behind the drift driven component. The transport driven component include the sink action of the limiter and the ballooning transport driven flows. The existence of ballooning transport is seen by the direct measurement of particle flux and density at the outboard and the top port in ADITYA. The dependence of the M_{tr} on the helicity has been observed.

Our measurements have shown the existence of finite transport driven flows in the edge plasma of the ADITYA tokamak. We have also shown that the existence of large flows in the SOL plasma determine reduced outward flux, and hence increased particle confinement. These results will provide database for further modelling of plasma parameters in the ADITYA tokamak.

7.2 Future Scope

The flows of the order of $M \sim 1$ has been reported in different tokamaks at the inboard side. In ADITYA, inboard side flow measurement may be of great help in identifying the contribution of ballooning type transport in the transport driven flows. The effect of the ballooning type transport driven flows is less on the outboard side as compare to the inboard side, so attempt should be made to measure the M simultaneously at both inboard and outboard side.

In this thesis we have presented the GP effect experiments only for the one direction combination of B_T and I_p. The GP experiment should be carried out in both positive and negative helicities, which helps in understanding the effects of different plasma limiter contact location. The location of particle source is known to play a crucial role in the SOL plasma flows; so the experiments should be carried out by varying the GP toroidal/poloidal locations. It helps to understand the effect of particle source location on SOL flows. The duration of GP should be increase to see its extended effects.

The poloidal flows are significant in the tokamak SOL. Our measured floating potential profile shows large gradient, which indicates significant poloidal flows in ADITYA. So attempts should be made to directly measure the direction and magnitude of poloidal flows along with the parallel flows. The direct measurements of poloidal flows will be of great help in determining the parallel/perpendicular flow dynamics in reducing the particle flux, and for the understanding of the turbulence and mean flow coupling. This can be done by using Gundestrup probe.

Bibliography

[1] J. Wesson, Tokamaks, Oxford University Press, Third Edition (2004).

[2] K. Miyamoto, Plasma physics and controlled Fusion, Springer (2005).

[3] J. A. Boedo, G. D. Porter, M. J. Schaffer, R. Lehmer, R. A. Moyer, J. G. Watkins, T. E. Evans, C. J. Lasnier, A. W. Leonard and S. L. Allen, *Phys. Plasmas* **5**, 4305 (1998).

[4] N. Asakura, S. Sakurai, M. Shimada, Y. Koide, N. Hosogane and K. Itami, *Phys. Rev. Lett.* **84**, 3093 (2000).

[5] S. K. Erents, A. V. Chankin, G. F. Matthews and P. C. Stangeby, *Plasma Phys. Controlled Fusion* **42**, 905 (2000).

[6] J. P. Gunn et. al, *J.Nucl. Mater.* **363-365**, 484 (2007).

[7] G. S. Xu et. al., *Phys. Rev. Lett.* **107**, 125001 (2011).

[8] A. R. Field et. al., *Plasma Phys. Controlled Fusion* **46**, 981 (2004).

[9] G. S. Xu, B. N. Wan, M. Song, and J. Li, *Phys. Rev. Lett.* **91**, 125001 (2003).

[10] E. Westerhof et al, *Nucl. Fusion* **47**, 85 (2007).

[11] H. W. Muller, V. Bobkov, A. Herrmann, M. Maraschek, J. Neuhauser, V. Rohde, A. Scmid, M. Tsalas and ASDEX Upgrade Team, *J. Nucl. Mater.* **363-365**, 605 (2007).

[12] B. LaBombard et. al., *Nucl. Fusion* **44**, 1047 (2004).

[13] R. A. Pitts, J. Horacek, W. Fundamenski, O. E. Garcia, A. H. Nielsen, M. Wischmeier, V. Naulin and J. J. Rasmussen, *J. Nucl. Mater.* **363-365**, 505 (2007).

[14] P. Bilkova, M. Aftanas, P. Bohm, V. Weinzettl, D. Sestak, R. Melich, J. Stockel, R. Scannell and M. Walsh, *J. Nucl. Mater.* **623**, 656 (2010).

[15] D. Sangwan, R. Jha, J. Brotankova, M. V. Gopalkrishana, *Phys. Plasmas* **19**, 092507 (2012).

[16] K. Tomabechi, J. R. Gilleland, Yu. A. Sokolov, R. Toschi and ITER Team, *Nucl. Fusion* **31**, 1135 (1991).

[17] P. C. Stangeby, The Plasma Boundary of Magnetic Fusion Devices (Institute of Physics Publishing Bristol and Philadelphia, 2000).

[18] P. C. Stangeby and G. M. McCracken, *Nucl. Fusion* **30**, 1225 (1990).

[19] N. Asakura, H. Takenaga, S. Sakurai, G. D. Porter, T. D. Rognlien, M. E. Rensink, K. Shimizu, S. Higashijima and H. Kubo, *Nucl. Fusion* **44**, 503 (2004).

[20] A. V. Chankin, D. P. Coster, N. Asakura, G. Corrigan, S. K. Erents, W. Fundamenski, H. W. Muller, R. A. Pitts, P. C. Stangeby and M. Wischmeier, *Nucl. Fusion* **47**, 762 (2007).

[21] O. E. Garcia, J. Horacek, R. A. Pitts, A. H. Nielsen, W. Fundamenski, V. Naulin and J. J. Rasmussen, *Nucl. Fusion* **47**, 667 (2007).

[22] C. S. MacLatchy, C. Boucher, D. A. Poirier, J. P. Gunn, B. L. Stansfield and W. W. Zuzak, *J. Nucl. Mater.* **196-198**, 248 (1992).

[23] N. Asakura, H. Takenaga, S. Sakurai, H. Tamai, A. Sakasai, K. Shimizu and G. D. Porter, *Plasma Phys. Controlled Fusion* **44**, 2101 (2002).

[24] M. G. Shats, D. L. Rudakov, R. W. Boswell and G. G. Borg, *Phys. Plasmas* **4**, 3629 (1997).

[25] B. LaBombard et. al., Phys. Plasmas **12**, 056111 (2005).

[26] J. W. Connor and H. R. Wilson, *Plasma Phys. Controlled Fusion* **42**, R1 (2000).

[27] M. J. Schaffer, D. G. Whyte, N. H. Brooks, J. W. Cuthbertson, J. Kim, S. I. Lippmann, M. Ali Mahdavi, R. Maingi and R. D. Wood, *Nucl. Fusion* **35**, 1000 (1995).

[28] S. K. Erents, R. A. Pitts, W..Fundamenski, J. P. Gunn. and G. F. Matthews, *Plasma Phys. Controlled Fusion* **46**, 1757 (2004).

[29] R. A. Pitts, G. Vayakis, G. F. Matthews and V. A. Vershov, *J. Nucl. Mater.* **176 & 177**, 893 (1990).

[30] I. H. Hutchinson, *Plasma phys. Controlled Fusion* **44** , 1953 (2002).

[31] N. Fedorczak, J. P. Gunn, P. Ghendrih, P. M. Garbet and A. Pocheau, *J. Nucl. Mater.* **390-391**, 368 (2009).

[32] A. S. Wan, B. LaBombard, B. Lipschultz and T. F. Yang, *J. Nucl. Mater.* **145-147**, 191 (1987).

[33] G. Proudfoot, P. J. Harbour, J. allen and A. Lewis, *J. Nucl. Mater.* **128 & 129**, 180 (1984).

[34] V. A. Vershkov, S. A. Grashin and A. V. Chankin, *J. Nucl. Mater.* **162**, 611 (1989).

[35] N. Asakura, ITPA SOL and Divertor Topical Group, *J. of Nucl. Mater.* **363-365**, 41 (2007).

[36] B. LaBombard, S. Gangadhara, B. Lipschultz, C. S. Pitcher, *J. Nucl. Mater.* **313-316**, 995 (2003).

[37] N. Smick, B. LaBombard, C. S. Pitcher, *J. Nucl. Mater.* **337-339**, 281 (2005).

[38] N. Asakura, S. Sakurai, N. Hosogane, M. shimada, K. Itami, Y. Koide and O. Naito, *Nucl. Fusion* **39**, 1983 (1999).

[39] J. Hugill, *J. Nucl. Mater.* **196-198**, 918 (1992).

[40] G. R. Tynan, L. Schmitz, R. W. Conn, R. doerner and R. Lchmer, *Phys. Rev. Lett.* **68**, 3032 (1992).

[41] C. Hidalgo, B. Goncalves, C. Silva, M. A. Pedrosa, K. Erents, M. Hron and G. F. Matthews, *Phys. Rev. Lett* **91**, 65001 (2003).

[42] E. Sanchez, C. Hidalgo, B. Goncalves, C. Silva, M. A. Pedrosa, M. Hron, K. Erents and JET EFDA contributors, *J. Nucl. Mater.* **337-339**, 296 (2005).

[43] B. Goncalves, C. Hidalgo, M. A. Pedrosa, R. O. Orozco, E. Sanchez and C. Silva, *Phys. Rev. Lett.* **96**, 145001 (2006)

[44] Y. H. Xu, C. X. Yu., J. R. Luo, J. S. Mao, B. H. Liu, J. G. Li, B. N. Wan and Y. X. Wan, *Phys. Rev. Lett.* **84**, 3867 (2000)

[45] D. Sangwan, R. Jha, J. Brotankova, M. V. Gopalkrishana, *Phys. Plasmas* **20**, 062503 (2013)

[46] V. Antoni, E. Spada, N. Vianello, M. Spolaore, R. Cavazzana, G. Serianni and E. Martines, *Plasma Phys. Controlled Fusion* **47**, B13 (2005).

[47] D. Sangwan, R. Jha, J. Brotankova, M. V. Gopalkrishana (under review, Physics of Plasmas).

[48] S. B. Bhat et. al., *Indian J. Pure Applied Phys.* **27**, 710 (1989).

[49] G. M. MaCracken and P. E. Stott, *Nucl. Fusion* **19**, 889 (1979).

[50] V. S. Mukhovatov and V. D. Shafranov, *Nucl. Fusion* **11**, 605 (1971).

[51] K. Miyamoto, Plasma Physics and Controlled Fusion (Springer, Berlin, 2005).

[52] D. Raju, Ph.D. Thesis: Study of Plasma Equilibrium and MHD Instability in ADITYA Tokamak, Devi Ahilya Vishwavidyalaya, Indore, 2002.

[53] V. S. Vlasenkov, V. M. Leonov, V. G. Merezhkin and V. S. Mukhovatov, *Nucl. Fusion* **13**, 509 (1973).

[54] Y. S. Bae et.al., *Nucl. Fusion* **49**, 022001 (2009).

[55] R. M. Gilgenbach et al, *Nucl. Fusion* **21**, 319 (1981).

[56] T. Ocho, S. Kubo, M. Ikeda, T. Saito, Y. Terumichi, Y. Hamada and S. Tanaka, *Phys. Lett.* **77A**, 318 (1980).

[57] I. Langmuir, *Phys. Rev. Lett.* **22**, 357 (1923).

[58] F. Waelbroeck, J. Winter and P. Wienhold, *J. Vac. Sci. Technol. A* **2**, 1521 (1984).

[59] R. C. Cross, J. R. Liu and L. Giannone, *Nucl. Fusion* **23**, 791 (1983).

[60] H. F. Dylla, *J. Nucl. Mater.* **93 & 94**, 61 (1980).

[61] H. A. Pathak and Y. C. Saxena, *J. Nucl. Materl.* **220-222**, 708 (1995).

[62] Y. Sakamoto et. al., *J. Nucl. Mater.* **93 & 94**, 333 (1980).

[63] S. V. Mirnov, Atomnaya Energiya **17**, 929 (1964).

[64] A. K. Chattopadhyay, A. Anand, C. V. S. Rao, S. Joisa and Aditya Team, *Indian J. Pure Appl Phys.* **44**, 826 (2006).

[65] R. J. Mauqeda, G. A. Wurden and E. A. Crawford, *Rev. Sci. Instrum.* **63**, 4717 (1992).

[66] I. Furno, H. Weisen, J. Mlynar, R. A. Pitts, X. Liobet, Ph. Marmillod and G. P. Pochon, *Rev. Sci. Instrum.* **70**, 4552 (1999).

[67] K. Tahiliani, R. Jha, M. V. Gopalkrishana, K. Doshi, V. Rathod, C. Hansalia and the ADITYA team, *Plasma Phys. Control. Fusion* **51**, 085004 (2009).

[68] S. Banerjee, V. Kumar, M. B. Chowdhuri, J. Ghosh, R. Manchanda, K. M. Patel and P. Vasu, *Meas. Sci. Technol.* **19**, 045603 (2008).

[69] M. Greenwald, *Plasma Phys. Contrlled Fusion* **44**, R27 (2002).

[70] J. A. Wesson, *Nucl. Fusion* **18**, 87 (1978).

[71] P. K. Atrey et. al., *Indian J. Phys.* **66B**, 499 (1992).

[72] D. Bohm, The Characteristics of Electrical Discharges in Magnetic Fields, New York: MacGraw-Hill, 1949.

[73] I. H. Hutchinson, Principles of Plasma Diagnostics (Cambridge University Press, Cambridge, United Kingdom 2005).

[74] H. M. Mott-Smith and I. Langmuir, *Phy. Rev.* **28**, 727 (1926).

[75] J. C. Sprott, *Rev. Sci. Instrum.* **37**, 897 (1996)

[76] J. C. Sprott, Electrostatic Probe Techniques, Thermonucl. Plasma Stud. Rep. PLP 88, 1966, University of Wisconsin.

[77] H. Ji, H. Toyama, K. Yamagishi, S. Shinohara, A. Fujisawa and K. Miyamoto, *Rev. Sci. Instrum.* **62**, 2326 (1991).

[78] M. Kamitsuma, S. L. Chen and J.-S. Chang, *J. Appl. Phys. D* **10**, 1065 (1977).

[79] S. L. Chen and T. Sekiguchi, *J. Appl. Phys.* **36**, 2363 (1965).

[80] E. O. Johnson and L. Malter, Phys. Rev. **80**, 58 (1950).

[81] H. Ohtsuka, H. Kimura, S. Shimomura, H. Maeda, S. Yamamoto, M. Nagami, N. Ueda, A. Kitsunezaki and T. Nagashima, *Plasma Phys.* **20** 749(1978)

[82] L. Oksuz and N. Hershkowitz, *Plasma Sources Sci. Technol.* **13**, 263 (2004).

[83] M. Hudis and L. M. Lidsky, *J. Appl. Phys.* **41**, 5011 (1970).

[84] P.J. Harbour and G. Proudfoot, *J. Nucl. Materl.* **121**, 222 (1984).

[85] P. C. Stangeby, *Phys. Fluids* **27**, 2699 (1984).

[86] I. H. Hutchinson, *Phys. Fluids* **30**, 3777 (1987).

[87] I. H. Huchinson, *Phys. Review A* **37**, 4358 (1988).

[88] H. V. Goubergen, R. R. Weynants, S. Jachmich, M. V. Schoor, G. V. Oost and E. Desoppere, *Plasma Phys. Controlled Fusion* **41**, L17 (1999).

[89] C. S. MacLatchy, C. Boucher, D. A. Poirier and J. Gunn, *Rev. Sci. Instrum* **63**, 3923 (1992).

[90] R. Jha, A. Sen, P. K. Kaw, P. K. Atrey, S. B. Bhatt, N. Bisai, K. Tahiliani, R. L. Tanna and the ADITYA Team , *Plasma Phys. Controlled Fusion* **51**, 095010 (2009).

[91] K. S. Chung, I. H. Hutchinson, B. LaBombard and R. W. Conn , *Phys. Fluids* **11**, 2229 (1989).

[92] B. J. Peterson, J. N. Talmadge, D. T. Anderson, F. S. B. Anderson and J. L. Shohet, *Rev. Sci. Instrum.* **65**, 2599 (1994).

[93] L. Patacchini and I. H. Hutchinson, *Plasma Phys. Controlled Fusion* **52**, 035005 (2010)

[94] L. Patacchini and I. H. Hutchinson, *Plasma Phys. Controlled Fusion* **53**, 025005 (2011)

[95] See Figure 5 of P. C. Stangeby, *Plasma Phys. Controlled Fusion* **37**, 1337 (1995).

[96] X. Zhang, D. Dandurand, T. Gray, M. R. Brown and V. S. Lukin, *Rev. Sci. Instrum.* **82**, 033510 (2011)

[97] B. LaBombard and B. Lipschultz, *Nucl. Fusion* **27**, 81 (1987).

[98] L. G. Askinazi, V. E. Golant, S. V. Levdev and L. S. Levin, *Phys. Fluids B* **5**, 2420 (1993).

[99] P. I. H. Cooke and A. K. Prinja, *Nucl. Fusion* **27**, 1165 (1987).

[100] N. Asakura, S. Sakurai, O. Naito, K. Itami, Y. Miura, S. Higashijima, Y. Koide and Y. Sakamoto, *Plasma Phys. Controlled Fusion* **44**, A313 (2002).

[101] M. A. Mahdavi, J. C. Deboo, C. L. Hsieh, N. Ohyabu, R. D. Stambaugh and J. C. Wesley, *Phys. Rev. Lett.* **47**, 1602 (1981).

[102] L. S. Scaturroand and B. Kusse, *Nucl. Fusion* **18**, 1717 (1978).

[103] K. Nagashima, A. Sakasai, T. Fukuda, *Nucl. Fusion* **33**, 1677 (1993).

[104] B. A. Carreras, L. W. Owen, R. Maingi, P. K. Miodudzewski, T. N. Carlstrom and R. J. Groebner, *Phys. Plasmas* **5**, 2623 (1998).

[105] P.C. Efthimion et al., *Phys. Rev. Lett.* **66**, 421 (1991).

[106] C. Hidalgo et al., *Nucl. Fusion* **31**, 1471 (1991).

[107] C. Hidalgo, J. H. Harris, T. Uckan, G. R. Hanson, J. D. Bell, M. A. Meier, C. P. Ritz and A. J. Wooten, *Nucl. Fusion* **33**, 146 (1993).

[108] W. L. Rowan, C. C. Klepper, C. P. Ritz, R. d. Bengtson, K. W. Gentle, P. E. Phillips, T. L. Rhodes, B. Richards and A. J. Wooton, *Nucl. Fusion* **27**, 1105 (1987).

[109] D. Sharma, R. Jha, Y. Feng and F. Sardei, *J. Nucl. Mater.* **438**, S554 (2013).

[110] L. G. Askinazi, V. A. Kornev, S.V. Krikunov, S. V. Lebedev, A. I. Smirnov, A. S. Tukachinsky, M. I. Vildjunas and N. A. Zhubr, *Nucl. Instrum. Methods Phys. Research A* **623**, 664 (2010).

[111] J. Allen and P. J. Harbour, *J. Nucl. Mater.* **145-147**, 264 (1987).

[112] N. Smick, B. LaBombard and I. H. Hutchinson, *Nucl. Fusion* **53**, 023001 (2013).